A CONTINUUM DAMAGE MECHANICS MODEL FOR DUCTILE FRACTURE
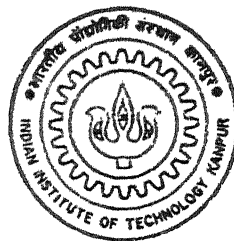
by

SANKAR DHAR

DEPARTMENT OF MECHANICAL ENGINEERING

INDIAN INSTITUTE OF TECHNOLOGY KANPUR
SEPTEMBER, 1995

A CONTINUUM DAMAGE MECHANICS MODEL FOR DUCTILE FRACTURE

A Thesis Submitted
in Partial Fulfillment of the Requirements
for the Degree of

DOCTOR OF PHILOSOPHY

by
SANKAR DHAR

to the

DEPARTMENT OF MECHANICAL ENGINEERING
INDIAN INSTITUTE OF TECHNOLOGY
KANPUR

SEPTEMBER, 1995

Certificate

August, 1995.

Certified that the work contained in this thesis entitled ' *A Continuum Damage Mechanics Model for Ductile Fracture* ', by Sankar Dhar has been carried out under our supervision and that this work has not been submitted elsewhere for a degree.

Dr. R. Sethuraman,
Department of Mechanical Engineering,
Indian Institute of Technology,
Kanpur.

Dr. P. M. Dixit,
Department of Mechanical Engineering
Indian Institute of Technology,
Kanpur.

To my daughter, HIKI

Synopsis

Application of linear elastic fracture mechanics to design of machine or structural components is restricted by the condition that the plastic zone at the crack tip be small compared to the size of the K dominant field and any relevant geometric dimension. It is virtually impossible to satisfy this condition for high toughness, low strength materials which generally undergo extensive plastic deformation and crack-tip blunting prior to the beginning of crack growth. Crack initiation in these materials is usually followed by a stable crack growth before it fails in catastrophic manner. The need to incorporate the influence of significant plastic deformation in crack growth initiation (i.e. the onset of growth of a existing crack) and subsequent stable growth is the main impetus for the development of elastic-plastic fracture mechanics. While the development in this field is ongoing, the theory of ductile fracture is not yet fully established. The use of HRR (Hutchinson [1] , Rice and Rosengren [2]) stress field to predict the stress and displacement fields ahead of a crack tip is restricted by several limitations like proportional loading, small crack-tip geometry change etc. Therefore, the use of J_{Ic} as a ductile fracture parameter becomes dependent on several conditions.

Recent investigations on ductile fracture show that the crack growth initiation in a ductile material is a microscopic phenomenon occurring over a small zone around the crack-tip. This zone is named as fracture process zone and is of the size of critical crack-tip opening displacement ($CTOD_c$). Within the fracture process zone, profuse void growth and coalescence occur which cause a local instability in the plastic flow and ultimately lead to ductile failure.

Modelling of the above phenomena in the framework of continuum mechanics in-

volves the following aspects:

(i) Constitutive modelling of the material behaviour to incorporate the effects of microstructural features of void growth,

(ii) Representation of void coalescence condition in terms of continuum parameters so as to identify a critical continuum parameter for micro crack initiation,

(iii) Use of the above critical continuum parameter along with a length parameter (representing the microstructural features of the material like grain size, inter-particle spacing etc) for the development of a local criterion for crack growth initiation.

In this thesis, the problem of ductile fracture is formulated with the help of continuum damage mechanics (CDM). The change in constitutive relations of the material due to void growth has been incorporated by introducing an internal damage variable (D) in the plastic potential. The damage variable is physically identified as the area void fraction at a point. Based on Lemaitre's CDM theory [3] and the experimental results of LeRoy et al [4] , a damage growth law is proposed as:

$$\dot{D} = c\dot{\epsilon}^p_{eq} + (a_1 + a_2 D)(-Y)\dot{\epsilon}^p_{eq}. \tag{0.1}$$

Here, a_1, a_2 and c are material constants derived from LeRoy's experimental results. $(-Y)$ is the thermodynamic force corresponding to the damage variable (D). The expression of $(-Y)$, as derived from Lemaitre's CDM theory, is given by

$$-Y = \frac{\sigma^2_{eq}}{2E(1-D)^2} \left[\frac{2}{3}(1+\nu) + 3(1-2\nu)(\frac{\sigma_m}{\sigma_{eq}})^2 \right]. \tag{0.2}$$

The ratio $(\frac{\sigma_m}{\sigma_{eq}})$ is called as triaxiality where σ_m is the mean stress and σ_{eq} is the von Mises equivalent stress. E is the Young's modulus, ν stands for poisson's ratio and $\dot{\epsilon}^p_{eq}$ is the equivalent plastic strain rate. Introduction of internal damage variable in plastic potential modifies the plastic flow rules. The modified plastic flow rules are stated below:

$$\dot{\epsilon}^p_{ij} = \frac{\lambda}{1-D} \frac{3}{2} \frac{\sigma'_{ij}}{\sigma_{eq}}, \tag{0.3}$$

$$\dot{p} = \frac{\lambda}{1-D} = \dot{\epsilon}^p_{eq}. \tag{0.4}$$

Here, σ'_{ij} is the deviatoric part of the stress tensor σ_{ij}, p is the hardening variable and λ stands for a scalar multiplier.

The constitutive equations cited above are used in an updated Lagrangian elastic-plastic FE programme which includes both material and geometric nonlinearities. The condition of void coalescence is derived from Thomason's [5] limit load model with appropriate modifications to suit the FE programme. The expression of the above condition is given below:

$$\sigma_1 - \left[0.1 + \frac{1.2}{\{1 - exp(-\epsilon^p_{eq}/2)\}^{\frac{1}{2}}} \right] exp(-\epsilon^p_{eq})\sigma_y = 0. \tag{0.5}$$

Here, σ_1 is the maximum principal stress and σ_y stands for current yield stress of the intervoid matrix material. Whenever the above condition is satisfied during the deformation process, micro crack initiation is assumed to take place.

Different case studies are performed with specimens of varying geometries. AISI-1090 spherodised steel is taken as the test material. It is found that, at micro crack initiation, the damage variable (D) reaches a critical value (D_c) which is almost constant for all the cases. Hence, the critical value of damage variable (D_c) is taken as a material property independent of specimen geometry. Further, it is observed from the case studies that a ductile fracture process depends on both plastic strain and triaxiality $(\frac{\sigma_m}{\sigma_{eq}})$. It should be noted that the damage variable incorporates the role of both plastic strain and the triaxiality (equation (1)).

Once the critical damage (D_c) is established as an accepted critical continuum parameter for micro crack initiation, it is used in a local criterion to predict the crack growth initiation in Mode-I ductile fracture. Average austenite grain size (l_c) is chosen as the critical length parameter. Thus, the local criterion is stated as:

$$D = D_c \quad \text{at } l = l_c. \tag{0.6}$$

That is, whenever D reaches the critical value D_c at a distance l_c ahead of the crack tip, the crack starts growing.

The crack growth initiation criterion cited above is used in numerical simulation to predict the fracture parameters like critical load (P_{cr}), fracture toughness (J_{Ic}) and critical crack-tip opening displacement (δ_{tc}) in plane strain condition. Standard fracture mechanics specimens (CT and TPB) are chosen for numerical simulation as well as for conducting experiments (both mechanical and metallurgical). The numerically predicted values of fracture parameters match favourably with their experimental values. Some additional results are also obtained from numerical simulations. These are also consistent with the results published earlier. Therefore, it is expected that the proposed local criterion (equation (6)) can predict the crack growth initiation in Mode-I ductile fracture.

A three dimensional numerical simulation, using the above crack growth initiation criterion, is also attempted in the last part of the thesis. The results give a consistent qualitative trend.

Finally, it is concluded that the critical damage D_c (or the critical area void fraction) is a satisfactory measure for predicting the crack growth initiation in ductile materials.

References

1. J.W.Hutchinson, (1968), 'Singular behaviour at the end of a tensile crack in a hardening material', J.Mech.Phys.Solids, 16, pp 13-31.

2. J.R.Rice and G.F.Rosengren, (1968), 'Plane strain deformation near a crack tip in a power-law hardening material', J.Mech.Phys.Solids, 16, pp 1-12.

3. J.Lemaitre, (1985), 'A continuous damage mechanics model for ductile fracture', J.Eng.Mat.Tech, 107, pp 83-89.

4. G.LeRoy, J.D.Embury, G.Edward and M.F.Ashby, (1981), 'A model of ductile fracture based on the nucleation and growth of voids', Acta Metall, 29, pp 1509-1522.

5. P.F.Thomason, (1990), 'Ductile fracture of metals', Pergamon Press (U.K).

Acknowledgement

I wish to place on record my deep sense of gratitude and indebtedness to Dr. P. M. Dixit and Dr. R. Sethuraman for their guidance and encouragement during the course of my thesis work. I am thankful to Prof. A. K. Mallik, Prof. A. Ghosh and Prof. V. Sundararajan for their valuable advice during my stay at I.I.T. Kanpur. Thanks are due to Mr. K. K. Bajpai, Mr. S. K. Sarkar and other members of Experimental Stress Analysis Laboratory. Thanks are also due to Mr. J. D. Verma of Q.I.P office, Mr. H. K. Nathani and others of Mechanical Engineering Department.

I like to acknowledge the help rendered to me by Mr. D. K. Pal of SEM Laboratory, Mr. S. P. Mukherjee of Metallography Laboratory, Mr. B. K. Jain of Material Testing Laboratory and Dr. K. S. Singh of computer center. I also acknowledge the supports given to me by my friends, Tapas, Basudev, Sandip, Gour, Tapan, Topobroto, Debashis, Monoj, Arun and Joydev. It will be unfair if I do not acknowledge the support and encouragement from my mother, Mrs Gouri Dhar and my wife, Mrs Sumana Dhar.

Lastly I wish to thank the authorities of Jadavpur University, Calcutta for granting leave to carry out my research work at I.I.T. Kanpur.

I.I.T. Kanpur.   Sankar Dhar
August, 1995.

Contents

.

.

List of Figures

List of Tables

List of symbols

a	effective crack length, Fig(5.1)
a	void dimension, Fig(2.3).
a_1	coefficient of void growth equation.
a_2	coefficient of void growth equation.
a_k	state variables in thermodynamic potential.
$\underline{a}$	flow vector.
A	slope of the hardening curve.
A	area.
A_n	area of intervoid matrix.
A_v	void area.
$\bar{A}_n$	area fraction of intervoid matrix.
A_k	thermodynamic forces.
A_k^c	conservative thermodynamic forces.
A_k^d	dissipative thermodynamic forces
b	ligament length, Fig(5.1).
b	void dimension, Fig(2.3).
B	thickness of fracture mechanics test specimen, Fig(5.1).
B	thermodynamic force in Rousselier's potential.
$[B]$	strain displacement matrix.
$[B]_L$	linear strain displacement matrix.
$[B]_N$	nonlinear strain displacement matrix.
c	coefficient in void growth equation.
C_{ijkl}	fourth order elasticity tensor.
C_{ijkl}^{EP}	fourth order elastic plastic tensor.
$[C]$	elasticity matrix.
$[C]^{EP}$	elastic plastic matrix.
d	intervoid spacing, Fig(2.3).
$\bar{d}$	grain diameter.
d_p	particle spacing in Rice and Tracy's formula.
D	damage variable.
D_c	critical damage.
D_p	particle diameter in Rice and Tracy's formula.
e_{ij}	Green Lagrange strain tensor.
E	Young's modulus.
f	void volume fraction in Gurson's model.
$\underline{f}$	internal force vector.
$\underline{f}^e$	internal force vector for the element.

F	plastic potential.
F_1	plastic potential associated with yielding.
F_D	damaged plastic potential.
$\underline{F}$	external force vector.
$\underline{F}^e$	external force vector for the element.
G	strain energy release rate.
$\dot{I}$	internal dissipation rate.
J	Rice's J integral.
J_I	J integral in mode I fracture.
J_{Ic}	critical value of J integral.
	plane strain fracture toughness.
K	hardening parameter equation (1.30).
K	material constant in Goods and Brown's formula.
K	stress intensity factor.
K_I	stress intensity factor in mode I fracture.
K_{Ic}	critical value of stress intensity factor.
$[K]$	stiffness matrix.
$[K]_L$	Linear part of the stiffness matrix.
$[K]_{NL}$	nonlinear part of the stiffness matrix.
l_c	critical length parameter.
n	hardening exponent equation (1.30).
N	hardening parameter in power hardening law equation (1.6).
p	hardening variable.
P	load.
P_L	limit load.
$\underline{P}$	load vector.
$q_1, \ q_2, \ q_3$	coefficients in Gurson's plastic potential.
r	distance ahead of crack tip.
r	particle radius in Goods and Brown's formula.
R	hardening force.
R	virtual work of external forces in FE formulation.
R	void radius in Rice and Tracy formula.
s	specific entropy.
S	entropy.
S_{ij}	2nd Piola Kirchoff stress tensor.
S_{ijkl}	fourth order compliance tensor.
t	time.
u	displacement.
u	displacement in x direction.
$\underline{u}$	displacement vector.

$\underline{u}^e$ elemental displacement vector.

U internal energy.

$\underline{U}$ global displacement vector.

v displacement in y direction.

V volume.

w velocity in z direction.

W width of fracture mechanics test specimen, Fig(5.1).

W^e strain energy density.

x Cartesian coordinate.

x_i position vector for a material point.

X_0 interparticle distance in Rice and Johnson's formula.

y Cartesian coordinate.

Y thermodynamic force corresponding to damage variable D.

z Cartesian coordinate.

α hardening parameter in power hardening law equation (1.6).

α_k internal state variable in thermodynamic potential.

β_k thermodynamic force corresponding to α_k.

δ variation.

δt crack tip opening displacement.

$(\delta t)_c$ critical crack tip opening displacement.

Δ increment in a quantity.

ϵ_{ij} infinitesimal strain tensor.

ϵ_{ij}^e elastic strain tensor.

ϵ_{ij}^p plastic strain tensor.

$\dot{\epsilon}_{ij}^p$ plastic strain rate tensor.

ϵ_{eq} equivalent strain.

ϵ_{eq}^p equivalent plastic strain.

$\dot{\epsilon}_{eq}^p$ equivalent plastic strain rate.

η Ernest factor.

$\Delta\eta_{ij}$ nonlinear part of the incremental strain tensor.

θ temperature in thermodynamic potential.

θ polar angle.

λ scalar multiplier in flow rules.

$^i\lambda$ load factor in arc length method.

ν poisson's ratio.

ρ density.

σ_{ij} Cauchy stress tensor.

σ_{ij} effective Cauchy stress tensor.

σ_{ij} deviatoric part of Cauchy stress tensor.

$\overset{\triangledown}{\sigma}_{ij}$ Jaumann stress rate.

σ_m mean stress.

σ_{eq} equivalent stress.

σ_{eq} effective equivalent stress.

σ_o initial yield stress.

σ_y current yield stress.

σ_1 maximum principal stress.

σ_n plastic constraint stress.

σ_{xx} normal stress in x direction.

σ_{yy} normal stress in y direction.

σ_{zz} normal stress in z direction.

$\frac{\sigma_m}{\sigma_{eq}}$ triaxiality.

Σ_m mean stress for porous aggregate in Gurson potential.

$\bar{\Sigma}$ effective stress for porous aggregate in Gurson potential.

Φ dissipative potential.

Ψ free energy.

ψ specific free energy.

Ω_{ij} spin tensor.

Chapter 1

INTRODUCTION

1.1 Introduction

Application of linear elastic fracture mechanics to design of machine or structural components is restricted by the condition that the plastic zone at the crack tip be small compared to the size of the K dominant field and any relevant geometric dimension. It is virtually impossible to satisfy this condition for high toughness, low strength materials which generally undergo extensive plastic deformation and crack-tip blunting prior to the beginning of crack growth. Crack initiation in these materials is usually followed by a stable crack growth before it fails in catastrophic manner. The need to incorporate the influence of significant plastic deformation in crack growth initiation (i.e. the onset of growth of a existing crack) and subsequent stable growth is the main impetus for the development of elastic-plastic fracture mechanics. While the development in this field is ongoing, the theory of ductile fracture is not yet fully established. The use of HRR (Hutchinson, 1968 [1] , Rice and Rosengren, 1968 [2]) stress field to predict the stress and displacement fields ahead of a crack tip is restricted by several limitations like proportional loading, small crack-tip geometry change etc. Therefore, the use of J_{Ic} (Rice, 1968 [3]) as a ductile fracture parameter becomes dependent on several conditions.

Recent investigations on ductile fracture show that the crack growth initiation in a

ductile material is a microscopic phenomenon occurring over a small zone around a crack tip. This zone is termed as fracture process zone which is estimated to be of the order of crack tip opening displacement $((\delta_t)_c)$ [4]. Within this fracture process zone, profuse void growth and coalescence occur which cause a local instability and ultimately the voids join in a void sheet to form micro cracks. When these micro cracks impinge with the parent crack, the crack growth initiation occurs. The void growth phenomenon depends on the purity of the material i.e. the presence of second phase particles or inclusions in the material. It also depends on the microstructural features of the material like grain size, inter particle spacing etc. For a material like steel the above phenomena are evident from the fractographs taken on the fracture surface where dimpled ruptured surface due to void growth is clearly visible. It is found from experiments that macroscopic material properties change when voids grow to a large extent.

While formulating the problem of ductile fracture in the frame work of continuum mechanics, the major difficulty is how to represent the microstructural phenomenon with the help of continuum parameters. Here some of the most important issues are as follows. The first issue is about the constitutive modelling for incorporating the effects of void growth on the material behavior. The choice of appropriate micro-model for void coalescence and its representation in terms of continuum variables is another important aspect of the problem. Finally one has to make use of this coalescence model to formulate a criterion for crack growth initiation with the help of some local parameters.

The above issues have been addressed by many research workers [5,6]. Due to difficulties in posing the problem in the frame work of continuum mechanics, several assumptions have been made. Thus, no single model addresses all the issues in a satisfactory manner. However, as far as constitutive modelling is concerned, the continuum damage mechanics (CDM) model [7,8] shows a lot of promise. The model has the capability to take care of loss of load bearing capacity and strain softening resulting from void growth. Similarly, Thomason's limit load model [9] seems to represent the phenomenon of void coalescence quite adequately.

Almost all the predictions made about ductile fracture have been qualitative. A quantitative prediction is rare. The present work aims at quantitative prediction of crack growth initiation in ductile materials. Elastic plastic finite element method coupled with CDM is employed for this purpose. Thomason's model for void coalescence is used to propose a local criterion for crack growth initiation. Numerical predictions are compared with experimental results to validate the proposed criterion.

1.2 Literature Survey

1.2.1 Stress and Displacement Analysis at the Crack Tip

Linear Elastic Fracture Mechanics (LEFM)

In a linearly elastic material, for a nominally stationary crack subjected to tensile (Mode I) opening, the local crack tip stresses and displacements can be characterised in terms of K_I singular field [10, 11]. Accordingly

$$\sigma_{ij}(r,\theta) = \frac{K_I}{\sqrt{2\pi r}} f_{ij}(\theta) + O(r^{\frac{1}{2}}) + \ldots \tag{1.1}$$

$$\Rightarrow \frac{K_I}{\sqrt{2\pi r}} f_{ij}(\theta) \quad \text{as} \quad r \to 0. \tag{1.2}$$

$$u_i = \frac{K_I}{2\mu} \sqrt{\frac{r}{2\pi}} g_i(\theta) \tag{1.3}$$

where, r is the distance ahead of crack tip, θ is the polar angle measured from the crack plane, f_{ij} is a dimensionless function of θ, g_i is a function of θ and bulk modulus of the material and μ stands for shear modulus. The configuration independent amplitude factor K_I is called the Mode I stress intensity factor. This parameter uniquely characterises the local stress field ahead of a crack and can be used as an indicator for crack growth (Irwin,1957). This asymptotic stress field dominates the crack tip vicinity over a region which is large compared to the scale of micro structural deformation and fracture events involved.

One of the principal limitations of the above approach is that a state of small scale yielding must exist. From equation (1.2) it is apparent that as r tends to zero the stresses become unbounded at the crack tip. In reality, however, such stresses are limited by local crack tip yielding which occurs over a zone ahead of the crack tip known as plastic zone. An approximate estimate of the plastic zone for monotonically loaded crack can be taken as [12]

$$r_y = \frac{1}{2\pi} \left(\frac{K_I}{\sigma_y} \right)^2 \quad \text{for plane stress,} \tag{1.4}$$

$$= \frac{1}{6\pi} \left(\frac{K_I}{\sigma_y} \right)^2 \quad \text{for plane strain} \tag{1.5}$$

where σ_y is the yield strength of the material. Provided the extent of local plasticity is small compared to the extent of K_I field which itself is small compared to the geometrical dimension of the body (including crack length) , the plastic zone can be considered as a small perturbation in the linear elastic field and the dominance of K_I field near crack tip remains valid. This situation is called the small scale yielding.

Elastic-Plastic Fracture Mechanics

Characterization of crack tip field by LEFM becomes unsuitable where small scale yielding conditions do not apply i.e when plastic zone size is comparable with the crack length. Since the K_I singular field is no longer appropriate in such instances, alternate asymptotic analysis has been done to determine the crack tip stress and strain fields in the presence of more extensive local plasticity. Based on the deformation theory of plasticity, the asymptotic form of these local fields, for materials obeying the power hardening law

$$\frac{\epsilon_{eq}^p}{\epsilon_y} = \alpha \left(\frac{\sigma_{eq}}{\sigma_y} \right)^N , \tag{1.6}$$

is given by so called HRR [1, 2] singular field:
As $r \to 0$,

$$\sigma_{ij}(r,\theta) \Rightarrow \sigma_y \left[\frac{J}{\alpha \sigma_y \epsilon_y I_N r} \right]^{\frac{1}{N+1}} \tilde{\sigma}_{ij}(\theta, N), \tag{1.7}$$

$$\epsilon_{ij}^{p}(r,\theta) \;\Rightarrow\; \alpha\epsilon_y \left[\frac{J}{\alpha\sigma_y\epsilon_y I_N \; r}\right]^{\frac{N}{N+1}} \tilde{\epsilon}_{ij}^{p}(\theta,N), \tag{1.8}$$

$$u_j(r,\theta) \;\Rightarrow\; \alpha\epsilon_y r \left[\frac{J}{\alpha\sigma_y\epsilon_y I_N \; r}\right]^{\frac{N}{N+1}} \tilde{u}_j(\theta,N) \tag{1.9}$$

where α and N are the hardening parameters, σ_{eq} and ϵ_{eq}^{p} are the equivalent stress and plastic strain, σ_y and ϵ_y are the yield stress and yield strain, I_N is a numerical constant weakly dependent on N, and $\tilde{\sigma}_{ij}(\theta,N)$, $\tilde{\epsilon}_{ij}(\theta,N)$, $\tilde{u}_j(\theta,N)$ are normalised stress, strain and displacement functions of N depending on the condition of plane stress or plane strain. The amplitude of this field is J-integral (Rice, 1968 [3]). J uniquely characterises the elastic-plastic crack tip field provided some degree of hardening is present and thus can be used to predict crack extension. For small scale yielding J can be identified as the strain energy release rate 'G' and hence can be related to K_I through the relation

$$J = G = \frac{K_I^{\,2}}{E'} \tag{1.10}$$

where E' is the appropriate elastic modulus (E for plane stress, and $E/(1-\nu^2)$ for plane strain where ν is the poisson's ratio).

It should be noted that HRR singular field and J-integral are strictly defined for a non linear elastic solid for which stress is a function of current strain rather than for a physically more realistic elastic-incrementally-plastic solid where strain increment is a function of current state of stress. Provided the crack remains stationary and is subjected only to a monotonically increasing load, the plastic loading does not depart radically from proportionality and this field remains valid. However, for a growing crack where regions of elastic unloading and non proportional plastic loading are embedded within the J dominated field, the crack tip field is not properly modelled by the HRR field [13].

An alternative treatment of elastic-plastic crack growth initiation, which is not subjected to above restrictions, is to utilise the concept of crack tip opening displacement or CTOD [14]. From equation (1.9), it is apparent that the opening of crack faces varies as $r^{\frac{1}{N+1}}$ when $r \to 0$. This separation can be used to define CTOD (δ_t) as the opening where 45° lines emanating from the crack tip intercept the crack faces [15].

Thus,

$$\delta_t = d_N(\epsilon_y, N)\frac{J}{\sigma_y} \qquad \text{for elastic plastic material,} \qquad (1.11)$$

$$= \frac{K_I{}^2}{\sigma_y E'} \qquad \text{for linearly elastic material.} \qquad (1.12)$$

Here, d_N is a constant depending on N, ϵ_y and the condition of plane stress or plane strain. For a perfectly plastic material and under plane stress condition, $d_N = 1$.

Effect of change of crack tip geometry

Substantial progress has been made in the recent years in analysing crack tip stress and deformation fields in elastic plastic materials [16,17]. Most of the solutions are based on conventional 'small geometry change' assumption. Two important changes are observed when the actual large geometry change of the crack tip is taken into account. Those are discussed by Rice and Johnson [18] . First, no severe strain concentration takes place directly ahead of the crack tip according to 'small geometry change' solution for nonhardening or moderately hardening materials. Further, an opening displacement at the crack tip can not defined. But, when progressive blunting of the crack tip is taken into account, intense strains do result directly ahead of the crack tip over a region of micro structural relevance like grain size, inter particle spacing etc. The second modification, due to large crack tip geometry change, has to do with stress distribution. Conventional 'small geometry change' solution gives a high stress concentration ahead of the crack tip (infinite for a continuous hardening material as the crack tip is approached) even when the strains are small. These high stresses result from high triaxiality ($\frac{\sigma_m}{\sigma_{eq}}$) at the crack tip. Here σ_m is the mean stress ($\sigma_m = \frac{1}{3}\sigma_{kk}$). When crack tip blunting is taken into account and the proper boundary conditions are imposed at the crack tip, the triaxiality reduces substantially at the crack tip. In other words, the stresses at the crack tip become finite. The above observations are also found in finite element computation of McMeeking and Parks [16].

From the above discussion, it is clear that the intense strain at the crack tip due to crack tip blunting plays an important role in the ductile fracture process . Though

a strain based criteria is likely to be appropriate, still the role of triaxiality can not be ignored.

1.2.2   Classical Fracture Criteria

The classical fracture criteria view fracture process in terms of continuum parameters. For brittle fracture, the crack tip stress field is characterised by K_I parameter whereas, for ductile fracture, it is J which specifies the crack tip stress and displacement fields. Sometimes crack tip opening displacement δ_t is used to describe the crack tip field. Note that the crack tip opening displacement δ_t has a unique relation with J or K_I (equation 1.11 and 1.12). Accordingly, the fracture toughness is defined by the critical value of K or J or δ_t. Thus, the crack growth initiation is predicted in Mode I by $K_I = K_{Ic}$ or $J_I = J_{Ic}$ or $\delta_t = \delta_{tc}$. Normally, the critical value (K_{Ic} or J_{Ic}) is determined from experimental load deflection curve. ASTM (E-399) specifies the standard for K_{Ic} and J_{Ic} tests.

The critical value of fracture parameters can also be expressed in terms of a characteristic dimension of microstructure (l_c) using local failure models. In one such model, the critical crack tip opening displacement is expressed in terms of the mean distance between the void initiating particles (Rice and Johnson, 1970 [18]). Thus

$$\delta_{tc} = 1 \text{ to } 2.7 \, X_o \tag{1.13}$$

where, X_o is the mean distance between the major void nucleating particles. From equations (1.11 and 1.13), this model implies the fracture toughness as:

$$J_{Ic} \sim \sigma_y X_o \tag{1.14}$$

although it is rare to find the toughness to increase directly with strength. Another approach to estimate the fracture toughness is to use the stress modified critical strain model (Mackenzie and coworkers, 1977 [19]). Here, local equivalent plastic strain has

to reach a critical ductility ($\epsilon_f(\frac{\sigma_m}{\sigma_{eq}})$), specific to the relevant triaxiality ($\frac{\sigma_m}{\sigma_{eq}}$) , over some characteristic length l_c. Accordingly, the fracture toughness is found as:

$$J_{Ic} \sim \sigma_y \, \epsilon_f \, l_c. \qquad (1.15)$$

Unlike the critical CTOD criterion, this criterion shows that the fracture toughness is proportional to product of strength and ductility which is physically more realistic.

1.2.3   Recent Development in Ductile Fracture

Recent investigations of ductile fracture reveal that a ductile fracture occurs mainly due to microvoid nucleation, growth and finally coalescence into micro crack. It is found from experiments that macroscopic material properties change due to void growth. As a result, the constitutive equations need to be changed when the extent of void growth is large (more than 10%) [20]. Thus, a realistic model for prediction of ductile fracture should include a void growth dependent material behavior and a condition for void coalescence. Three broad approaches have emerged which try to predict ductile fracture (micro crack initiation) on the basis of void nucleation, growth and coalescence. These are as follows:
(i) Porous Plasticity model of Berg and Gurson [21, 22]
(ii) Void Nucleation, Growth and Coalescence model (Goods and Brown-Rice and Tracy-Thomason Model) [28, 29, 26].
(iii) Continuum Damage Mechanics Model [7, 8].

These three approaches are discussed in the following paragraphs. Next, some phenomenological models of ductile fracture are discussed. When a micro crack initiation criterion is to be used for prediction of crack growth initiation, an additional (local) length parameter is needed. Some local criteria for crack growth initiation are discussed at the end of the section.

Porous Plasticity Model of Berg and Gurson

In this model, the material with voids is idealised as a porous material. Thus,

its constitutive equation is derived from the plastic potential of porous material. In a porous plastic material, there is a possibility of dilatation because of which the yield surface does not remain an infinitely long cylinder but capped by elliptical surfaces. Based on Berg's [21] model of dilational plasticity, Gurson [22] proposed a plastic potential for porous plastic material. Starting from a unit spheroidal cell with a single central void, he obtained the following expression for the potential function for a porous solid with randomly distributed voids of volume fraction 'f' :

$$\Phi(\sigma_{ij}, f, \sigma_y) = \frac{\bar{\Sigma}^2}{\sigma_y^2} + 2\, q_1\, f\, \cosh\left(\frac{3\, q_2\, \Sigma_m}{2\, \sigma_y}\right) - 1 - q_3\, f^2 = 0 \qquad (1.16)$$

Here $q_1 = q_2 = q_3 = 1$. (Tvergaard [23] assinged some other values to the constants q_1 and q_2 ($q_1 = 1.5$, $q_2 = 1$ and $q_3 = q_1^2$) to bring the predictions of the model into closer agreement with full numerical analysis of a periodic array of voids). $\bar{\Sigma}$ and Σ_m are the effective and mean stresses of the porous aggregate and σ_y is the flow-stress of the incompressible matrix.

In this model, void nucleation is assumed to be a continuous process. Accordingly, it is represented by the relation

$$df_{nucleation} = A d\epsilon_{eq}^p \qquad (1.17)$$

where A is constant. The void growth law is derived from the condition of plastic incompressibility. Thus

$$df_{growth} = (1 - f)d\epsilon_{kk}^p. \qquad (1.18)$$

The total incremental void volume fraction is of course the sum of the incremental void volume fraction due to nucleation and growth:

$$df = df_{nucleation} + df_{growth}. \qquad (1.19)$$

When the surrounding material ceases to deform, the dilation gets localised in a band (called as shear band). This concentration of dilational plastic deformation in a small zone gives rise to plastic instability leading to ductile fracture. Thus, in this model,

ductile fracture is regarded as the result of an instability in the weak dilatational plastic flow field in the shear band. Rudnicki and Rice [24] derived the conditions for the instability without considering any imperfection in the material. Later Tvergaard [23] and Yamamoto [25] investigated the conditions for instability in the presence of material imperfections. They represented the fracture criterion as a graph of critical localisation strain versus the critical void volume fraction with strain hardening exponent as a parameter.

In this model, it is assumed that the void coalescence by internal necking of intervoid matrix is a secondary effect which can only develop after the incipient formation of an intense shear band. However, according to Thomason [26], the primary mechanism of ductile fracture is the internal necking of the intervoid matrix which can be adequately modelled only by the incorporation of a strong dilatational response. It is this failure to appreciate the dominant effect of internal necking, that severely limits the validity of the Berg-Gurson model.

Before discussing the next model, it should be mentioned here that some research workers [27] have used the Berg-Gurson model without the instability conditions of Yamamoto. They characterised fracture by the critical value of 'f' (void volume fraction) which was determined experimentally.

Void Nucleation, Growth and Coalescence Model (Goods and Brown-Rice and Tracy-Thomason)

In this model, Thomason [26] combined the results of Goods and Brown [28] on void nucleation, those of Rice and Tracy [29] on void growth and his own on void coalescence to arrive at a fracture criterion in the form of a graph of fracture strain versus the mean stress. For numerical predictions, this graph can be used along with conventional elastic plastic constitutive equations. Thus in the present model, the effect of void nucleation and growth are incorporated not in the constitutive equations but in the fracture criterion itself. The void nucleation model of Goods and Brown, void

growth model of Rice and Tracy and void coalescence model of Thomason are described below. Along with them, some additional models on void nucleation and growth are also discussed.

Void Nucleation Models

A stress based void nucleation model is based on the condition that the void nucleation by *decohesion* of particles occurs whenever the normal stress at the particle/matrix interface reaches the critical value σ_c. Goods and Brown [28] used this condition to derive the following relation for void nucleation strain (ϵ_1^n) in terms of the mean stress σ_m:

$$\epsilon_1^n = K \ r \ (\sigma_c - \sigma_m)^2 \tag{1.20}$$

Here, r is the particle radius and K is a material constant depending on the particle volume fraction. Experiments on $Fe - Fe_3C$ system [28] confirm the linear relationship between the void nucleating strain and the particle radius. The relation (1.20) is for small spheroidal particles ($r < 1\mu m$). For larger size particles, the approximate analysis of Argon et al [30] gives the following condition for the void nucleation by *decohesion*:

$$\sigma_{eq} + \sigma_m = \sigma_c. \tag{1.21}$$

For a given problem, this condition can be expressed in terms of the nucleation strain. Note that this condition is independent of particle radius.

A different void nucleation model has been proposed by Gurland [31]. His experiment on 1.05% C spherodised steel shows that the void nucleation by *cracking* of cementite particles takes place continuously. Voids nucleate at all strain levels depending on the size, shape and orientation with the maximum principal stress direction. It is observed that the volume fraction of broken particles is a linear function of the plastic strain. Note that the void nucleation relation (equation 1.17) used in the Berg-Gurson model is of this type only.

It should be noted that the development of a very general model of void nucleation is a difficult task as a typical commercial alloy contains a wide range of particle types

and particle morphologies which can result in a variety of void nucleation mechanisms operating simultaneously. Further such a model may be too complicated to be amenable to analysis for making useful numerical predictions.

Void Growth Models

Once the nucleation of a microvoid takes place either by decohesion or cracking of a second-phase particle or inclusion, the resulting stress-free surface of the void produces a localised stress and strain concentration in the surrounding plastically deforming matrix. With continuing plastic flow of the matrix, the void undergoes volumetric growth and change of shape. If it is assumed that the sites of void nucleation are sufficiently far apart to have any interaction between the neighbouring voids, then one can study the void growth phenomenon by considering a single void in an infinite medium.

Rice and Tracy [29] considered a single spherical void of initial radius R_o in a remote uniform strain rate field $\dot{\epsilon}_{ij}$ and remote stress field σ_{ij} in a rigid-plastic material. They derived the following expression for the rate of change of the radii of curvature ($\dot{R}_k$) in the principal strain-rate directions:

$$\dot{R}_k = [(1 + E)\dot{\epsilon}_k + \dot{\epsilon}_{eq}D] R_{mean} \qquad (k=1,2,3) \qquad (1.22)$$

where

$$
\begin{aligned}
E \;&=\; \frac{2}{3} \quad \text{for linear hardening and for low values of } \sigma_m \text{ for non-hardening,} \\
&=\; 1 \quad \text{for high values of } \sigma_m \text{ for non-hardening,} \\
D \;&=\; 0.75\frac{\sigma_m}{\sigma_y} \quad \text{for linear hardening,} \\
&=\; 0.558 \sinh\left(\frac{3}{2}\frac{\sigma_m}{\sigma_y}\right) + 0.008\nu \cosh\left(\frac{3}{2}\frac{\sigma_m}{\sigma_y}\right) \quad \text{for non-hardening,} \\
R_{mean} \;&=\; \frac{1}{3}(R_1 + R_2 + R_3), \\
\dot{\epsilon}_{eq} \;&=\; equivalent\ strain\ rate, \\
\dot{\epsilon}_k \;&=\; principal\ strain\ rates, \\
\nu \;&=\; -\frac{3\dot{\epsilon}_2}{\dot{\epsilon}_1 - \dot{\epsilon}_3}, \quad \text{Lode variable.}
\end{aligned}
$$

Note that an initial spherical void grows into an ellipsoidal void of principal radii R_1, R_2 and R_3. Thomason [26] integrated the above equation by assuming that the principal axes of the strain-rates remain fixed in direction throughout the strain path and obtained the following expressions for the principal radii of the void:

$$R_1 = \left(A + \frac{3(1+\nu)}{2\sqrt{\nu^2+3}} B \right) R_o, \tag{1.23}$$

$$R_2 = \left(A - \frac{\nu\, B}{\sqrt{\nu^2+3}} \right) R_o, \tag{1.24}$$

$$R_3 = \left(A + \frac{(\nu-3)\, B}{2\sqrt{\nu^2+3}} \right) R_o, \tag{1.25}$$

where

$$A = exp \left(\frac{2\sqrt{\nu^2+3}}{(3+\nu)} D \epsilon_1^g \right), \tag{1.26}$$

$$B = \left(\frac{1+E}{D} \right) (A-1) \tag{1.27}$$

and ϵ_1^g is the integral of the largest principal strain rate. Thomason used the expressions (1.23 - 1.25) in his derivation of the condition for void coalescence.

For an array of void nucleating particles of diameter D_p and spacing d_p, setting the initial void radius as $D_p/2$ and integrating equation (1.22) upto the point of fracture, the fracture strain ϵ_f (for a non hardening material) is obtained as:

$$\epsilon_f = \frac{\ln\left(\frac{d_p}{D_p}\right)}{0.28\; exp\left(\; 1.5\frac{\sigma_m}{\sigma_{eq}}\;\right)}. \tag{1.28}$$

Similar analysis has been done by McClintock [32] for the case of cylindrical voids in plane strain condition. The corresponding fracture strain expression is given by

$$\epsilon_f = \frac{\ln\left(\frac{d_p}{D_p}\right)(1-n)}{\sinh\left[(1-n)(\sigma_a+\sigma_b)/\frac{2\sigma_{eq}}{\sqrt{3}}\right]}. \tag{1.29}$$

Here σ_a and σ_b are the principal stress components and n is the hardening parameter defined by

$$\sigma_y = K\left(\epsilon_{eq}^p\right)^n. \tag{1.30}$$

The material constant K is different than that used in equation (1.20).

Some research workers [33,34] have used the expressions (1.28) and (1.29) for prediction of ductile fracture with the help of some experimentally determined parameters. The major limitations of this approach are that it ignores the effects of void nucleation (as the expressions are derived from a pre-existing finite size void) and void coalescence. Thus, usually ϵ_f is overestimated. However, these expressions do reveal the dependence of ϵ_f and fracture toughness on triaxiality ($\frac{\sigma_m}{\sigma_{eq}}$), hardening n and the purity ($\frac{d_p}{D_p}$) of the material.

Void Coalescence condition

Thomason [26] has modelled void coalescence phenomenon as plastic instability due to necking of the intervoid matrix. According to him, the sufficient condition for plastic instability of the intervoid matrix is given by

$$\sigma_n \bar{A}_n - \sigma_1 = 0 \qquad (1.31)$$

where $\bar{A}_n$ is the area fraction of the intervoid matrix perpendicular to the direction of maximum principal stress σ_1 and σ_n is the plastic constraint stress. He considered a geometrically equivalent square prismatic void with the same principal dimensions as the ellipsoidal void and used the upper bound method to obtain the expression for the plastic constraint stress in terms of the void dimensions, intervoid spacing and the yield stress. The details of this derivation are described in Chapter 2.

Fracture Criterion

Thomason used expressions (1.23 - 1.25) for the void dimensions to express the void coalescence condition (equation 1.31) in terms of the void growth strain ϵ_1^g and the mean stress σ_m. By superposing this condition on the void nucleation relation (equation 1.20), he obtained the fracture criterion as a graph of fracture strain ($\epsilon_f = \epsilon_1^n + \epsilon_1^g$) versus the mean stress.

The main drawback of this approach is the use of expressions (1.23 - 1.25) for the

void growth. These expressions are based on integration procedure which assumes that the principal directions of strain rates remain fixed throughout the strain path. This is true only for the case of small strain and rotation. As a result, this approach can not be used when the strains and/or rotations are large.

Continuum Damage Mechanics Models

In continuum damage mechanics model, the change in material behavior due to void growth is taken care of by introducing the damage variable as an internal variable in the plastic potential. The damage variable is supposed to quantify the intensity of microvoids. As a result, it is usually identified as either the void volume fraction or area void fraction. The theory of continuum thermodynamics is used to derive the plastic flow rules and the damage growth law.

It should be kept in mind that the main objective of continuum damage mechanics model is to incorporate the effects of void growth in the constitutive equations. However, there is a scope to include the void nucleation phenomenon in the damage growth law. But, as far as void coalescence is concerned, it has to be incorporated as an additional condition in terms of the continuum parameters. This condition, which serves as a fracture criterion, has to be based on an appropriate micro model. Thomason's limit load model [26] seems to be a good candidate for this purpose.

Based on Kachanov's idea of effective stress (for creep damage), Lemaitre [7] proposed a damage mechanics model for void growth in elastic plastic materials. Details of the model are described in Chapter 2 of the thesis. Lemaitre used a simple damage growth law in which the damage rate is linearly dependent on the plastic strain and the thermodynamic force corresponding to the damage. Later, Tai and Yang [35] modified the damage growth law to make it dependent on the current value of damage. They obtained the material constants appearing in the damage growth law from the experimental results of LeRoy et al [36] on area void fraction measurements at different strain levels. Jun [37] introduced non linearity with respect to plastic strain in the

damage growth law. The degree of nonlinearity for a material is adjusted by a parameter which is determined from tension test data. Applications of Lemaitre's model are found in the works of many authors, however, there seems to be no attempt at combining the model with a void coalescence criterion for the purpose of prediction of ductile fracture.

Another popular model is due to Rousselier [8] . Rousselier model consists of a damaged plastic potential in terms of current density ρ of the material and mean stress σ_m. Accordingly, the plastic potential is given as

$$\Phi = \left[J_2 \left(\frac{\sigma'_{ij}}{\rho} \right) \right]^{\frac{1}{2}} - \sigma_y + B \ g \left(\frac{\sigma_m}{\rho} \right). \tag{1.32}$$

Here, σ'_{ij} is the deviatoric part of the stress tensor σ_{ij}, J_2 is the 2nd invariant of σ'_{ij}, g is a function related to the dialatational effect of void growth and B stands for the thermodynamic force corresponding to damage variable β which is implicitly present in the plastic potential through the density function i.e

$$\beta = \beta(\rho) \tag{1.33}$$

The mass conservation law is used to derive the expressions for the function g, the thermodynamic force B and the damage growth $\dot{\beta}$.

Bilby, Howard and Li [38] applied the Rousselier's model to predict the $J - R$ curve for a spinning cylinder. The model was implemented with updated Lagrangian elastic plastic FE programme. However, for the purpose of prediction of crack growth, instead of using a condition for void coalescence, they used a stress based local criterion. Zheng, Luo and Zheng [39] used Rousselier's model to derive a macro damage parameter for prediction of crack initiation in metal forming processes.

Phenomenological Models

In the absence of reliable quantitative models for incorporating the phenomena of void nucleation, growth and coalescence in materials undergoing large plastic deformation, in metal forming processes, empirical relations based on some phenomenological

models are used. They are many in number. Here, only two popular models are discussed.

Cockcroft and Latham [40] suggested a fracture criterion of ductile material based on the idea of critical plastic work. Accordingly, their criterion is stated as

$$\int_o^{\epsilon_f} \sigma_{eq} d\epsilon_{eq}^p = constant. \tag{1.34}$$

Here, ϵ_f stands for fracture strain in tension test. For a tensile specimen, the change in neck geometry influences the fracture process. In order to take care of the effect of change in neck geometry, the above expression is modified as

$$\int_o^{\epsilon_f} \sigma_{eq} \left(\frac{\sigma_1}{\sigma_{eq}} \right) d\epsilon_{eq}^p = constant \tag{1.35}$$

or,

$$\int_o^{\epsilon_f} \sigma_1 d\epsilon_{eq}^p = constant \tag{1.36}$$

Here, σ_1 is the maximum normal stress. The dimensionless factor $\left(\frac{\sigma_1}{\sigma_{eq}} \right)$ acts as a stress concentrator.

The main criticism of the model is that the role of hydrostatic stress is not incorporated in this model even though it is accepted, in general, that the hydrostatic stress also influences the ductility of the material.

Another popular criterion used in the field of metal forming is due to Oyane [41]. The Oyane's model is based on a theory of plasticity of porous materials where dialatational stress-strain relation is assumed as

$$d\epsilon_m = \frac{d\epsilon_{eq}}{A} \left(\frac{\sigma_m}{\sigma_{eq}} + A_o \right) \tag{1.37}$$

where ϵ_{eq} is equivalent strain, ϵ_m stands for volumetric strain and A and A_o are material constants. Oyane integrated equation (1.37) over the total strain path to give

$$\int_o^{\epsilon_f} A \frac{d\epsilon_m}{A_o} = \int_o^{\epsilon_f} \left(1 + \frac{\sigma_m}{A_o \sigma_{eq}} \right) d\epsilon_{eq}. \tag{1.38}$$

Here, ϵ_f is the fracture strain in tension test. It is assumed that the left hand side of equation (1.38) is a material constant. Thus,

$$\int_o^{\epsilon_f} \left(1 + \frac{\sigma_m}{A\sigma_{eq}} \right) d\epsilon_{eq} = B_o, \qquad \text{a constant.} \tag{1.39}$$

The main objection to this criterion is that the ductile fracture is governed by critical volumetric strain independently of deviatoric strain. Ductile fracture in pure shear contradicts this theory.

Local Crack Growth Initiation Criteria

All the criteria discussed so far are for micro-crack initiation. When these criteria are to be used for prediction of crack growth initiation, an additional (local) length parameter is needed. Some existing local criteria for crack growth initiation are discussed next.

Critical Stress Criterion

A stress based criterion states that the cleavage fracture propagates in an unstable manner when the maximum principal stress (σ_{yy}) ahead of a crack tip reaches a critical value (σ_f^*). RKR (Ritchie, Knott and Rice) [42] proposed a local criteria for cleavage fracture of a sharp crack which requires the local tensile stress (σ_{yy}) to exceed a critical fracture stress over a microstructural characteristic length l_c. In their work on quantitative prediction of fracture toughness of mild steel at low temperature, the fracture stress was determined by breaking a V notched bent bar at low temperature and σ_{yy} was found from Hill's slip line solution. RKR found that their prediction gives best agreement with the experimental value when $l_c = 2\bar{d}$, where $\bar{d}$ is the diameter of Fe grain.

Critical Strain Criterion

Ritchie, Server and Wullaert [43] used the strain based criterion to predict fracture toughness of $A533B$ and $A302B$ alloy steels. The critical fracture strain was determined from tension test of circumferentially notched round specimen. The equivalent plastic strain (ϵ_{eq}^p) was found from Rice and Johnson's [18] solution. Their findings show a

critical length l_c, varying from one to six times the average MnS particle spacing.

1.3 Objective of the Present Work

The present work is an investigation of Mode I fracture in ductile material where void nucleation, growth and coalescence play a predominant role. The aim of the work is to identify a critical continuum parameter and critical (local) length parameter to predict crack growth initiation in Mode I ductile fracture. The following are the broad objectives of the thesis.

1. To study the role of void growth in ductile fracture process and to propose a void growth law.

2. To determine the critical value of area void fraction of the material for micro crack initiation and to establish its independence of specimen geometry.

3. To propose a crack growth initiation criterion in Mode I ductile fracture using the critical area void fraction and a critical (local) length parameter.

4. To predict the global fracture parameters (like J_{Ic}) numerically using the proposed crack growth initiation criterion

5. To verify the numerically predicted values of the fracture parameters with experiments (both mechanical and metallurgical) to validate the proposed crack growth initiation criterion.

1.4 Plan of the Thesis

Lemaitre's continuum damage mechanics model is used to derive the constitutive equations (flow rules and damage growth law) of a material with voids. The damage is identified as an area void fraction. The updated Lagrangian elastic plastic FE formula-

tion (which includes both material and geometric nonlinearities) is used for numerical simulation. Thomason's criterion for void coalescence is used to determine the critical value of the area void fraction. The critical value of area void fraction along with a critical length parameter is used to predict the global fracture parameters. Experiments have been carried out to verify the results of numerical simulation.

Chapter 2 of the thesis deals with constitutive equations of a material with voids. The concept of continuum damage, due to Lemaitre[7], is used to modify the von Mises plastic potential. A damage growth law, based on LeRoy's experimental results [36] on AISI 1090 spherodised steel, is proposed. The law also incorporates void nucleation. A micro model for void coalescence (Thomason [26]) is also discussed. The model is modified appropriately, without changing the basic principle, to suit the elastic plastic FE formulation.

Chapter 3 is devoted to updated Lagrangian elastic plastic FE formulation. Both the nonlinearities, material and geometrical, have been incorporated in the FE analysis. Deformation due to finite strain as well as rotation has been considered. Different numerical schemes are also discussed here. The elastic plastic FE programme developed on the basis of the above formulation is used in the later part of the thesis to investigate the Mode I fracture of ductile material numerically.

Chapter 4 is a numerical investigation of micro crack initiation, due to void nucleation, growth and coalescence, for different specimens of AISI 1090 spherodised steel. The constitutive equations developed in chapter 2 and the FE formulation of chapter 3 are applied together along with Thomason's model. The critical value of damage variable (area void fraction) is found to be almost constant for all the specimens analysed. Hence, the critical value of damage variable is taken as a parameter for crack growth initiation in the later part of the thesis.

Chapter 5 deals with the Mode I fracture of a ductile material like AISI 1095 spherodised steel in plane strain condition. A crack growth initiation criterion is proposed

in terms of the damage as a critical continuum parameter and austenite grain size as a critical length parameter. Numerical simulations of standard fracture mechanics tests have been carried out using the FE formulation of chapter 3. The results of numerical simulations are compared with experiments (both mechanical and metallurgical) to validate the proposed crack growth initiation criterion.

Chapter 6 is an extension of the work to 3D case. The effects of variation in thickness on critical fracture parameters are studied. The variation of continuum parameters at the crack front, along the thickness, has also been observed in this study.

Chapter 2

CONTINUUM DAMAGE MECHANICS

2.1   Introduction

Investigation of ductile failure of metals requires the knowledge of material behavior at microstructural level. It has been found from metallurgical test results that the ductile fracture occurs due to void nucleation, growth and finally coalescence into a micro crack. In order to model the void growth phenomenon in continuum mechanics, the idea of continuum damage mechanics (CDM) is very helpful. In CDM, the material behavior is represented by a plastic potential which includes damage as an internal variable. The plastic flow-rules and the damage growth law are derived from the plastic potential.

The basis of the continuum damage mechanics rests on the theory of continuum thermodynamics. It is well known that the constitutive relations must obey the basic laws of thermodynamics. Hence a brief discussion of continuum thermodynamics is given first in sections 2.2 and 2.3 [44,45]. Next, Lemaitre's continuum damage mechanics model and the resulting constitutive equations of a damaged material are presented in sections 2.4 and 2.5. In the end, a criterion for void coalescence and micro crack initiation is discussed.

2.2 Thermodynamics of a Continuum

A thermodynamic process is normally described by a set of kinematic variables a_k ($k = 1, 2, \ldots, n$) and the absolute temperature θ (non negative). These quantities are known as independent state variables. Any function of the state variables is referred as state function. Examples of state function are internal energy $U(a_k, \theta)$, entropy $S(a_k, \theta)$, free energy $\Psi(a_k, \theta)$ etc. For a reversible process, the free energy or the thermodynamic potential completely specifies the thermomechanical behavior of a continuum. By means of the two thermodynamic laws, we get the following expression for the conservative part, A_k^c, of the thermodynamic force corresponding to a_k:

$$A_k^c = \frac{\partial \Psi}{\partial a_k}. \tag{2.1}$$

A_k^c is also called as the conjugate variable corresponding to a_k. Since, the entropy production is zero, there is no need to introduce the dissipative part of the thermodynamic forces. As an example, consider the following expression for specific free energy for an elastic process:

$$\psi = \frac{1}{2\rho} \, C_{ijkl} \epsilon_{ij}^e \epsilon_{kl}^e - \theta s. \tag{2.2}$$

Here, the components of elastic strain tensor ϵ_{ij}^e are the kinematic variables. C_{ijkl} is the fourth order elasticity tensor and s is the specific entropy. The Cauchy stress tensor is given by

$$\sigma_{ij} = \rho \frac{\partial \psi}{\partial \epsilon_{ij}^e} = C_{ijkl} \epsilon_{kl}^e. \tag{2.3}$$

For an irreversible process, it is necessary to consider the dissipative thermodynamic forces in order to describe the thermomechanical behavior of a continuum. For such a process, the rate of entropy production $\dot{S}^i$ is not a state variable but in general a function of $\dot{a}_k$, $\dot{\theta}$, a_k, and θ. Normally this functional relationship is expressed for the dissipative power which is nothing but the product of absolute temperature θ and the rate of entropy production $\dot{S}^i$. The superscript ' i ' stands for the irreversible process while the superscript '.' denotes the time rate of the quantity. Thus for an irreversible

process, the dissipative power can be expressed as

$$\theta \dot{S}^i = \Phi(\ \dot{a}_k,\ \dot{\theta},\ a_k,\ \theta\ ). \tag{2.4}$$

If we assume that an irreversible system is purely dissipative, then the dissipative forces A_k^d can be completely derived from Φ. Thus

$$A_k^d = \frac{\partial \Phi}{\partial \dot{a}_k}. \tag{2.5}$$

The quantity Φ is called the dissipative potential. The 2nd law of thermodynamics states that

$$\Phi \geq 0. \tag{2.6}$$

2.3 Thermodynamic Process with Internal Variables

In the field of mechanics or thermodynamics, all variables can be classified into two categories, namely the variables which are measurable or controllable and the variables which can not be measured or controlled directly. The first kind is termed as external variable whereas the second one is called as internal variable. When we include them in thermodynamic potential, we call them as external state variable and internal state variable respectively.

For dissipative phenomena, the current state also depends on the past history. This history can only be represented by means of internal variables. For example in a damaged elastic-plastic material, the history of deformation can be represented by accumulated plastic strain, accumulated damage etc.

The thermodynamic potential or free energy as a function of internal state variables α_k is expressed as

$$\Psi = \Psi(a_k, \alpha_k, \theta) \tag{2.7}$$

and the corresponding thermodynamics forces are given by

$$A_k^c = \frac{\partial \Psi}{\partial a_k}, \tag{2.8}$$

$$\beta_k^c = \frac{\partial \Psi}{\partial \alpha_k}, \tag{2.9}$$

$$S = -\frac{\partial \Psi}{\partial \theta}. \tag{2.10}$$

Here, β_k^c is the conservative part of the thermodynamics force β_k corresponding to the internal state variable α_k.

When the dissipative potential $\Phi(\dot{a}_k, \dot{\alpha}_k, \dot{\theta}, a_k, \alpha_k, \theta)$ is also function of internal state variables α_k and $\dot{\alpha}_k$, the dissipative forces are given by

$$A_k^d = \frac{\partial \Phi}{\partial \dot{a}_k} \tag{2.11}$$

and,

$$\beta_k^d = \frac{\partial \Phi}{\partial \dot{\alpha}_k}. \tag{2.12}$$

Here, β_k^d is the dissipative part of the thermodynamic force β_k corresponding to the internal variable α_k. Since β_k is an internal force,

$$\beta_k^c + \beta_k^d = 0$$

or,

$$\beta_k^d = -\beta_k^c. \tag{2.13}$$

2.3.1 Elastic-plastic Process

When the temperature change is not significant, the dissipative potential for an elastic-plastic process is expressed as

$$\Phi = \Phi(\dot{\epsilon}_{ij}^p, \dot{p}, \dot{D}, \epsilon_{ij}^p, p, D). \tag{2.14}$$

Here, p and D are taken as internal variables corresponding to isotropic hardening and damage respectively. The physical identification of the damage variable is discussed in detail in the next section. For the case of strain hardening, p is nothing but the equivalent plastic strain ϵ_{eq}^p. Thus

$$p = \epsilon_{eq}^p = \int_o^t \dot{\epsilon}_{eq}^p \, dt \tag{2.15}$$

and

$$\dot{\epsilon}^p_{eq} = \left(\frac{2}{3}\dot{\epsilon}^p_{ij}\dot{\epsilon}^p_{ij}\right)^{\frac{1}{2}}. \tag{2.16}$$

The quantity $\dot{\epsilon}^p_{ij}$ is the plastic part of the strain rate tensor and ϵ^p_{ij} is the integral of $\dot{\epsilon}^p_{ij}$ along the particle path. Therefore,

$$\sigma_{ij} = \frac{\partial \Phi}{\partial \dot{\epsilon}^p_{ij}}, \tag{2.17}$$

$$-R = \frac{\partial \Phi}{\partial \dot{p}}, \tag{2.18}$$

$$-Y = \frac{\partial \Phi}{\partial \dot{D}}. \tag{2.19}$$

Here, $-R$ and $-Y$ are the dissipative parts of the thermodynamic forces corresponding to the internal variables p and D respectively. These laws are called as complementary laws while equations (2.8 - 2.10) are called as state laws. Using Legendre-Fenchel transformation [45], one can transform $\Phi(\dot{\epsilon}^p_{ij}, \dot{p}, \dot{D}, \epsilon^p_{ij}, p, D)$ to its dual $\Phi^*(\sigma_{ij}, -R, -Y)$ and write the complementary laws as the evolution laws of the flux variables. Thus

$$\dot{\epsilon}^p_{ij} = \frac{\partial \Phi^*}{\partial \sigma_{ij}}, \tag{2.20}$$

$$\dot{p} = \frac{\partial \Phi^*}{\partial (-R)}, \tag{2.21}$$

$$\dot{D} = \frac{\partial \Phi^*}{\partial (-Y)}. \tag{2.22}$$

Since Φ^* or Φ is governed by an inequality (see equation 2.6), its actual value is usually difficult to determine. As a result, the above laws are not useful from the computational point of view. To derive the useful relations, we maximise the dissipation Φ^* using the yield function or the plastic potential $F(\sigma_{ij}, -R, -Y)$, which has a zero value on the yield surface, as a constraint. Thus

$$\delta(\Phi^* - \lambda F) = 0 \tag{2.23}$$

where δ denotes the variation and λ acts as a Lagrangian multiplier. The function F is called an indicator function. Combining equations (2.20 - 2.22) with equation (2.23), we

get

$$\dot{\epsilon}^p_{ij} = \lambda \frac{\partial F}{\partial \sigma_{ij}}, \tag{2.24}$$

$$\dot{p} = \lambda \frac{\partial F}{\partial (-R)}, \tag{2.25}$$

$$\dot{D} = \lambda \frac{\partial F}{\partial (-Y)}. \tag{2.26}$$

The laws (2.24 - 2.26) are called as plastic flow rules and they describe the mechanical behavior of an elastic-plastic material.

2.4 Introduction to Damage Mechanics

Damage represents surface discontinuities in the form of micro cracks or volume discontinuities in the form of micro voids. The description of material behavior of a damaged material involves an additional internal variable, called as the damage variable, which quantifies the intensity of damage. If it is assumed that the voids are scattered in an isotropic way, then this variable can be assumed as a scalar quantity which is denoted by D in the literature. Here the damage variable is identified as area void fraction at a point in a plane. That is,

$$D = \frac{\Delta A_v}{\Delta A} \tag{2.27}$$

where ΔA is an infinitesimal area around the point in some plane and ΔA_v is the area of the void traces in the plane contained in ΔA. The introduction of damage variable leads to the concept of effective stress i.e. the stress calculated over the effective area ($\Delta A - \Delta A_v$) that actually resists the forces. Thus the effective Cauchy stress tensor at a point is defined as

$$\sigma^*_{ij} = \frac{\sigma_{ij}}{(1 - D)}. \tag{2.28}$$

Another important concept is the principle of strain equivalence which states that the deformation behavior of a damaged material is represented by the constitutive laws of the virgin material in which the usual stress is replaced by the effective stress . The concept is represented in Fig(2.1).

When temperature change is not significant, the specific free energy of an elastic process in a damaged material can be obtained using the principle of strain equivalence. Following Lemaitre [7], we get

$$\psi = \frac{1}{2\rho}C_{ijkl}\epsilon_{ij}^e\epsilon_{kl}^e(1-D).$$ (2.29)

From equation (2.29) the Cauchy stress components are found as

$$\sigma_{ij} = \rho\frac{\partial\psi}{\partial\epsilon_{ij}^e} = C_{ijkl}\epsilon_{kl}^e(1-D).$$ (2.30)

Further, the conservative part of the thermodynamic force (Y) corresponding to D is given by

$$Y = \rho\frac{\partial\psi}{\partial D} = -\frac{1}{2}C_{ijkl}\epsilon_{ij}^e\epsilon_{kl}^e.$$ (2.31)

Since it is an internal force, the dissipative counterpart of Y is obtained as (see equation 2.13)

$$-Y = \frac{1}{2}C_{ijkl}\epsilon_{ij}^e\epsilon_{kl}^e.$$ (2.32)

For a better physical interpretation of Y, equation (2.32) can be modified as follows. From equation (2.30), we get

$$\frac{d\sigma_{ij}}{dD} = C_{ijkl}(1-D)\frac{d\epsilon_{kl}^e}{dD} - C_{ijkl}\epsilon_{kl}^e.$$ (2.33)

For constant stress,

$$\frac{d\sigma_{ij}}{dD} = 0$$ (2.34)

and hence,

$$C_{ijkl}\epsilon_{kl}^e = C_{ijkl}(1-D)\frac{d\epsilon_{kl}^e}{dD}.$$ (2.35)

Using equation (2.35) in equation (2.32), we get

$$-Y = \frac{1}{2}C_{ijkl}(1-D)\epsilon_{ij}^e\frac{d\epsilon_{kl}^e}{dD}\bigg|_{\sigma=constant}$$

or,

$$-Y = \frac{1}{2}\sigma_{ij}\frac{d\epsilon_{ij}^e}{dD} = \frac{1}{2}\frac{dW_e}{dD}\bigg|_{\sigma=constant}.$$ (2.36)

Here $dW_e = \sigma_{ij}d\epsilon^e_{ij}$ is the elemental strain energy per unit volume. Therefore, $-Y$ is nothing but the change in strain energy due to damage when the stress remains constant.

An explicit expression for $(-Y)$, for an isotropic material, can be found from equations (2.32) and (2.30) which will be useful in the later part of the thesis. First, inverting the equation (2.30), we get

$$\epsilon^e_{ij} = \frac{1}{1-D}S_{ijkl}\sigma_{kl} \tag{2.37}$$

where S_{ijkl} is the inverse of C_{ijkl}. The above expression, when substituted in equation (2.32), gives $-Y$ in terms of the stress tensor.

$$-Y = \frac{1}{2(1-D)^2}S_{ijkl}\sigma_{ij}\sigma_{kl}. \tag{2.38}$$

Using S_{ijkl} for an isotropic material and decomposing stress tensor in its deviatoric and mean components, we can write

$$-Y = \frac{1}{2}\left[\frac{(1+\nu)}{E}\frac{\sigma'_{ij}\sigma'_{ij}}{(1-D)^2} + 3\frac{(1-2\nu)}{E}\frac{\sigma^2_m}{(1-D)^2}\right]. \tag{2.39}$$

Here, E and ν are the elastic constants of the material,

$$\sigma'_{ij} = \sigma_{ij} - \frac{1}{3}\sigma_{ii} \tag{2.40}$$

is the deviatoric part of σ_{ij} and

$$\sigma_m = \frac{1}{3}\sigma_{ii} \tag{2.41}$$

is the mean part. Using the definition of equivalent stress

$$\sigma_{eq} = \left[\frac{3}{2}\sigma'_{ij}\sigma'_{ij}\right]^{\frac{1}{2}}, \tag{2.42}$$

the expression (2.39) can be written as

$$-Y = \frac{\sigma^2_{eq}}{2E(1-D)^2}\left[\frac{2}{3}(1+\nu) + 3(1-2\nu)(\frac{\sigma_m}{\sigma_{eq}})^2\right]. \tag{2.43}$$

The term within the bracket in equation (2.43) is termed as triaxiality function $f\left(\frac{\sigma_m}{\sigma_{eq}}\right)$ whereas the quantity $\left(\frac{\sigma_m}{\sigma_{eq}}\right)$ is named as triaxiality. Thus,

$$-Y = \frac{\sigma^2_{eq}}{2E(1-D)^2}f\left(\frac{\sigma_m}{\sigma_{eq}}\right). \tag{2.44}$$

Using the definition of effective stress, we get

$$-Y = \frac{\sigma_{eq}^{*\,2}}{2E} f\left(\frac{\sigma_m}{\sigma_{eq}}\right).$$

(2.45)

2.5 The Constitutive Equations for Elastic-plastic Process in a Damaged Material

The constitutive equations for elastic-plastic behavior of a damaged material can be derived from the appropriate plastic potential F. We assume that, in metal plasticity, it is possible to decompose F as

$$F = F_1(\sigma_{ij}, R, D) + F_D(-Y, p, D)$$

(2.46)

where F_D is the plastic potential associated with damage such that it reduces to zero whenever $D = 0$. For a material yielding according to von Mises criterion, the form of F_1 is

$$F_1 = \frac{\sigma_{eq} - R}{1 - D} - \sigma_o$$

(2.47)

where σ_o is the initial yield stress in tension. When $D = 0$, F_1 reduces to the original form due to von Mises. Now the plastic flow rules (equation 2.24 - 2.26) become

$$\dot{\epsilon}_{ij}^p = \lambda \frac{\partial F_1}{\partial \sigma_{ij}} = \frac{\lambda}{1 - D} \frac{3}{2} \frac{\sigma_{ij}'}{\sigma_{eq}},$$

(2.48)

$$\dot{p} = \lambda \frac{\partial F_1}{\partial(-R)} = \frac{\lambda}{1 - D},$$

(2.49)

$$\dot{D} = \lambda \frac{\partial F_D}{\partial(-Y)}.$$

(2.50)

Combining equations (2.15) and (2.49), we get the following expression for λ:

$$\lambda = (1 - D)\dot{\epsilon}_{eq}^p.$$

(2.51)

Substitution of expression (2.51) into equations (2.48) and (2.50) leads to the following constitutive equations (stress-strain rate relation and damage growth law):

$$\dot{\epsilon}_{ij}^p = \frac{3\dot{\epsilon}_{eq}^p}{2\sigma_{eq}}\sigma_{ij}',$$

(2.52)

$$\dot{D} = (1 - D)\dot{\epsilon}^p_{eq} \frac{\partial F_D}{\partial(-Y)}. \tag{2.53}$$

This stress-strain rate relation is not really convenient for an updated Lagrangian formulation for which the incremental stress-strain relation is needed. It is derived in Chapter 3 starting from the expressions (2.46) and (2.47) for the plastic potential.

Unlike F_1, F_D is not well established in literature. As a result, we can not use equation (2.53) as the damage growth law. Therefore, experimental results on void measurement at different deformation levels are used to propose a damage growth law. Based on experimental results of LeRoy et al [36] for spherodized steel, the following growth law is proposed.

$$\dot{D} = c\dot{\epsilon}^p_{eq} + (a_1 + a_2 D)(-Y)\dot{\epsilon}^p_{eq}. \tag{2.54}$$

Here the coefficients a_1, a_2 and c are material constants which are evaluated from experimental results. The 1st term of the equation (2.54) represents the void nucleation as proposed by Gurland [31]. As stated in chapter 1, this model assumes that void nucleation takes place continuously at all strain levels. The other terms of the equation represent the void growth phenomena as proposed by several workers [35,37]. It is worthy to note that in Lemaitre's [7] analysis the term corresponding to a_2 is not considered where as in the work of Tai and Young [35] the term corresponding to a_1 is missing. From the experimental results of LeRoy et al [36] , it is observed that the graph of area void fraction versus strain is almost linear at low strain level but it is highly nonlinear at higher values of strain. Therefore it seems to be wise to retain both the terms in void growth rate equation (2.54). One can add more nonlinear terms like $a_3 D^2$, $a_4 D^3$, etc. But it is found that, for the material under study, such terms have insignificant contribution.

Coming back to equation (2.45), the conjugate variable$(-Y)$ corresponding to damage D can be expressed in terms of equivalent plastic strain in the following way. Using the definition of effective stress, the expression (2.47) for the plastic potential F_1 can be expressed as

$$F_1 = \sigma^*_{eq} - \sigma_y \tag{2.55}$$

where the yield stress σ_y of the material is given by

$$\sigma_y = \left(\frac{R}{1-D} + \sigma_o \right). \tag{2.56}$$

For most materials, the strain hardening relationship is expressed by a power law:

$$\sigma_y = K \left(\epsilon_{eq}^p \right)^n \tag{2.57}$$

where K and n are hardening parameter and exponent respectively. Since F_1 is zero along the yield surface, from equation (2.55) and (2.57), we get

$$\sigma_{eq}^* = K \left(\epsilon_{eq}^p \right)^n. \tag{2.58}$$

After substituting this expression in equation (2.45), $-Y$ becomes

$$-Y = \frac{K^2}{2E} \left(\epsilon_{eq}^p \right)^{2n} f \left(\frac{\sigma_m}{\sigma_{eq}} \right). \tag{2.59}$$

Then the damage growth law (equation 2.54), in terms of the equivalent plastic strain, can be written as

$$\dot{D} = c\dot{\epsilon}_{eq}^p + (a_1 + a_2 D) \frac{K^2}{2E} \left(\epsilon_{eq}^p \right)^{2n} f \left(\frac{\sigma_m}{\sigma_{eq}} \right) \dot{\epsilon}_{eq}^p. \tag{2.60}$$

The form of the damage growth law as cited in equation(2.60) is used in FE computation.

2.6 The Void Coalescence and Micro-crack Initiation

Experimental studies on micro structural features of ductile fracture indicate that the ductile fracture process is essentially a localized plastic instability occurring simultaneously in the inter void matrix between a large number of coalescing microvoids [26]. According to this reference, the sufficient condition for plastic instability of the intervoid matrix at a point is given by (equation 1.31)

$$\sigma_1 = \sigma_n \bar{A}_n \tag{2.61}$$

where σ_1 is the current maximum principal stress of the macroscopically homogeneous state of stress at the point, $\bar{A}_n$ is the current area fraction of the inter void matrix perpendicular to the direction of σ_1 and σ_n is the critical stress required to initiate localized plastic flow or internal necking. The stress σ_n is called the plastic constraint stress.

Since there are about 10^5 microvoids in an area of 0.25 mm^2 of the ductile fracture surface[26], one can describe the fracture process by using a simple unit cell model in which the unit cell represents the statistical average of the microvoid size and intervoid spacing at the point under consideration. Thomason [26] considered a geometrically equivalent square prismatic void with the same principal dimensions as the ellipsoidal void (Figs 2.2(a), (b)) and used the upper bound method to obtain the expression for plastic constraint stress. A brief outline of the method is given in the next few paragraphs.

Thomason assumed a certain portion of the unit cell as a plastic zone and divided that zone into a number of generating segments. He used parallel generating segment (Fig 2.2 (c)) for a smaller void size and triangular generating segment (Fig 2.2 (d)) for larger void size. He assumed the following kinematically admissible velocity field.

(a) For parallel generating segment (Fig 2.2 (c)):

$$\dot{u} = \frac{\dot{W}}{2ax} \left[(b+d)^2 - x^2 \right] , \tag{2.62}$$

$$\dot{v} = \frac{\dot{W}y}{2ax^2} \left[(b+d)^2 - x^2 \right] , \tag{2.63}$$

$$\dot{w} = \frac{\dot{W}z}{a} , \tag{2.64}$$

$$\dot{s} = \sqrt{\dot{u}^2 + \dot{v}^2}. \tag{2.65}$$

(b) For triangular generating segments (Fig 2.2 (d)):

$$\dot{u} = \frac{\dot{W}d}{2ax} \left[(b+d) + x \right], \tag{2.66}$$

$$\dot{v} = \frac{\dot{W}yd}{2ax^2} \left[(b+d) + x \right], \tag{2.67}$$

$$\dot{w} = -\frac{\dot{W}zd}{2ax},$$
(2.68)

$$\dot{s} = \frac{\dot{W}}{2x}\left[(b+d)+x\right]\left[1+\left(\frac{d}{a}\right)^2+\left(\frac{y}{x}\frac{d}{a}\right)^2\right]^{\frac{1}{2}}.$$
(2.69)

Here $\dot{u}$, $\dot{v}$, $\dot{w}$ are Cartesian velocity components at a point (x,y,z), $\dot{W}$ is the velocity (in z direction) of the intervoid matrix at the top and bottom boundaries, a and b are the void dimensions, d is the intervoid spacing and $\dot{s}$ is the tangential velocity discontinuity on boundaries between the plastic zone and the remaining rigid zone (such surfaces are indicated in the Figs 2.2 (c) and 2.2 (d)).

The rate of internal energy dissipation $\dot{I}$ in the plastic zone V and the rigid-plastic boundaries S is given by

$$\dot{I} = \sqrt{\frac{2}{3}}\sigma_o^*\int_V\left[\dot{\epsilon}_{xx}^2+\dot{\epsilon}_{yy}^2+\dot{\epsilon}_{zz}^2+2\left(\dot{\epsilon}_{xy}^2+\dot{\epsilon}_{yz}^2+\dot{\epsilon}_{zx}^2\right)\right]^{\frac{1}{2}}dv+\frac{\sigma_o^*}{\sqrt{3}}\int_S\dot{s}\,ds.$$
(2.70)

Here, σ_o^* stands for the yield stress of the rigid perfectly plastic material in the intervoid matrix. Using the strain rate velocity relations

$$\dot{\epsilon}_{xx} = \frac{\partial\dot{u}}{\partial x}, \quad \dot{\epsilon}_{yy} = \frac{\partial\dot{v}}{\partial y}, \quad \dot{\epsilon}_{zz} = \frac{\partial\dot{w}}{\partial z},$$

$$\dot{\epsilon}_{xy} = \frac{1}{2}\left(\frac{\partial\dot{u}}{\partial y}+\frac{\partial\dot{v}}{\partial x}\right),$$

$$\dot{\epsilon}_{yz} = \frac{1}{2}\left(\frac{\partial\dot{v}}{\partial z}+\frac{\partial\dot{w}}{\partial y}\right),$$

$$\dot{\epsilon}_{zx} = \frac{1}{2}\left(\frac{\partial\dot{w}}{\partial x}+\frac{\partial\dot{u}}{\partial z}\right),$$
(2.71)

and the expressions (2.62 - 2.69) for the velocity field, $\dot{I}$ can be expressed in terms of $\dot{W}$, the void dimensions (a and b) and the intervoid spacing d.

The rate of external work done is given by

$$\dot{E} = \sigma_n A_n \dot{W}.$$
(2.72)

Here A_n represents the actual cross sectional area of the inter void matrix perpendicular to $\dot{W}$. Setting $\dot{E} = \dot{I}$, an expression for σ_n can be obtained in terms of the current void dimensions and σ_o^*. Thomason obtained the solution of the above equation numerically. The numerical result obtained by him can be approximated by the following relation:

$$\sigma_n = \left[\frac{0.1}{\left(\frac{a}{d}\right)^2} + \frac{1.2}{\left(\frac{b}{b+d}\right)^{\frac{1}{2}}} \right] \sigma_o^*. \tag{2.73}$$

For a strain hardening material, the above expression should be modified by replacing σ_o^* with the current yield stress σ_y of the intervoid matrix material. Thus,

$$\sigma_n = \left[\frac{0.1}{\left(\frac{a}{d}\right)^2} + \frac{1.2}{\left(\frac{b}{b+d}\right)^{\frac{1}{2}}} \right] \sigma_y. \tag{2.74}$$

Elimination of σ_n from equations (2.61) and (2.74) leads to the following criterion for the void coalescence and micro crack initiation.

$$\sigma_1 - \left[\frac{0.1}{\left(\frac{a}{d}\right)^2} + \frac{1.2}{\left(\frac{b}{b+d}\right)^{\frac{1}{2}}} \right] \bar{A}_n \sigma_y = 0. \tag{2.75}$$

Therefore, whenever the combination of stress components and void size and spacing satisfies equation (2.75), void coalescence and micro crack initiation take place at that point. Since the upper bound solution gives an overestimated plastic constraint stress (σ_n), the above combination is an overestimation of onset of micro crack initiation.

In order to incorporate the above criteria in FE analysis, the current void dimensions and spacing should be expressed in terms of stress or strain. Thomason used Rice and Tracey's[29] expressions (equations 1.23 - 1.25) to express a, b and d in terms of strain and triaxiallity. However, as stated in Chapter 1, these expressions are valid only for the case of small strain/rotation and therefore not suitable for large strain/rotation. Several research workers [46] have suggested that, at void coalescence, the a /d ratio should lie between 0.8 to 1.2 depending on the triaxiality $\left(\frac{\sigma_m}{\sigma_{eq}}\right)$ at the point. In the experimental

results of LeRoy et al [36], a/d is observed to be close to 1.0. Therefore. in the present work , it is taken as 1.0. Thus,

$$\frac{a}{d} = 1.0. \tag{2.76}$$

To relate the void dimension ' b ' and the intervoid spacing ' d ' to the strain at the point, we assume that the equivalent plastic strain ϵ_{eq}^p at the point. as defined by equations (2.15 - 2.16), is more or less equal to the axial plastic strain of the unit cell (Fig 2.3). Then, neglecting the elastic strain, we get

$$\bar{A}_n = \frac{A_n}{A_o} = exp(-\epsilon_{eq}^p) \tag{2.77}$$

and hence,

$$\frac{d}{b+d} = exp(-\epsilon_{eq}^p/2). \tag{2.78}$$

Equation (2.78) implies that

$$\frac{b}{b+d} = 1.0 - exp(-\epsilon_{eq}^p/2). \tag{2.79}$$

Substituting equations (2.76), (2.77) and (2.79) into equation (2.75), we get

$$\sigma_1 - \left[0.1 + \frac{1.2}{\{1 - exp(-\epsilon_{eq}^p/2)\}^{\frac{1}{2}}} \right] exp(-\epsilon_{eq}^p) \, \sigma_y = 0. \tag{2.80}$$

Thus, whenever equation (2.80) is satisfied in the course of FE incremental computation, the micro crack initiation or void coalescence takes place at that point.
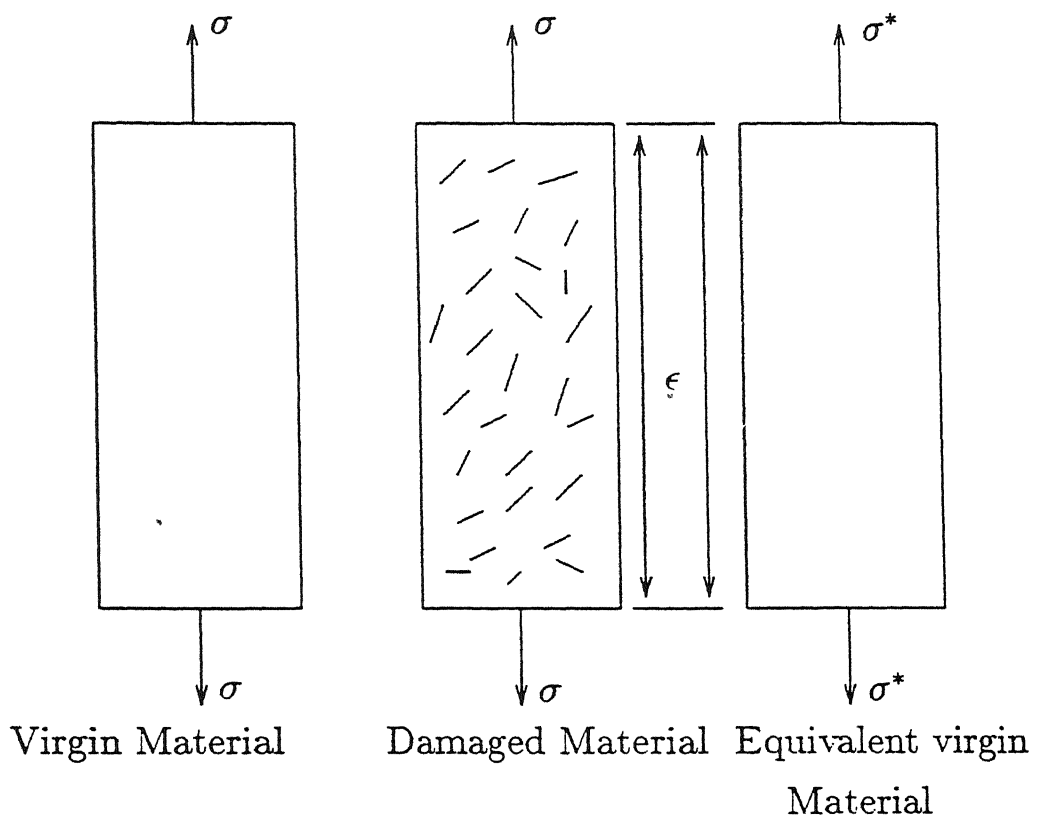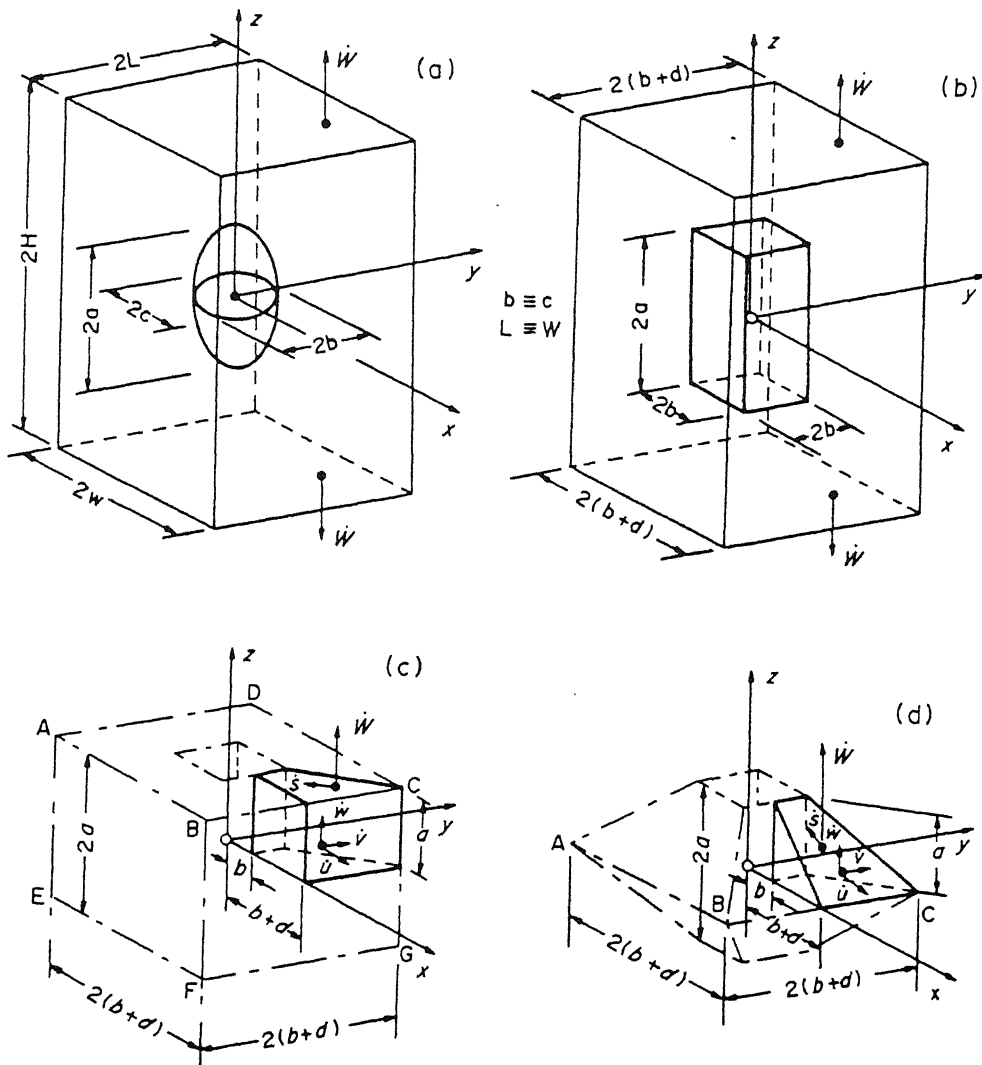
Fig. 2.1 : Strain equivalence principle.

Fig. 2.2 The unit cell and velocity fields in
the intervoid matrix.

(a) An ellipsoidal void, (b) The equivalent square-prismatic
void, (c) The parallel velocity field, (d) The triangular ve-
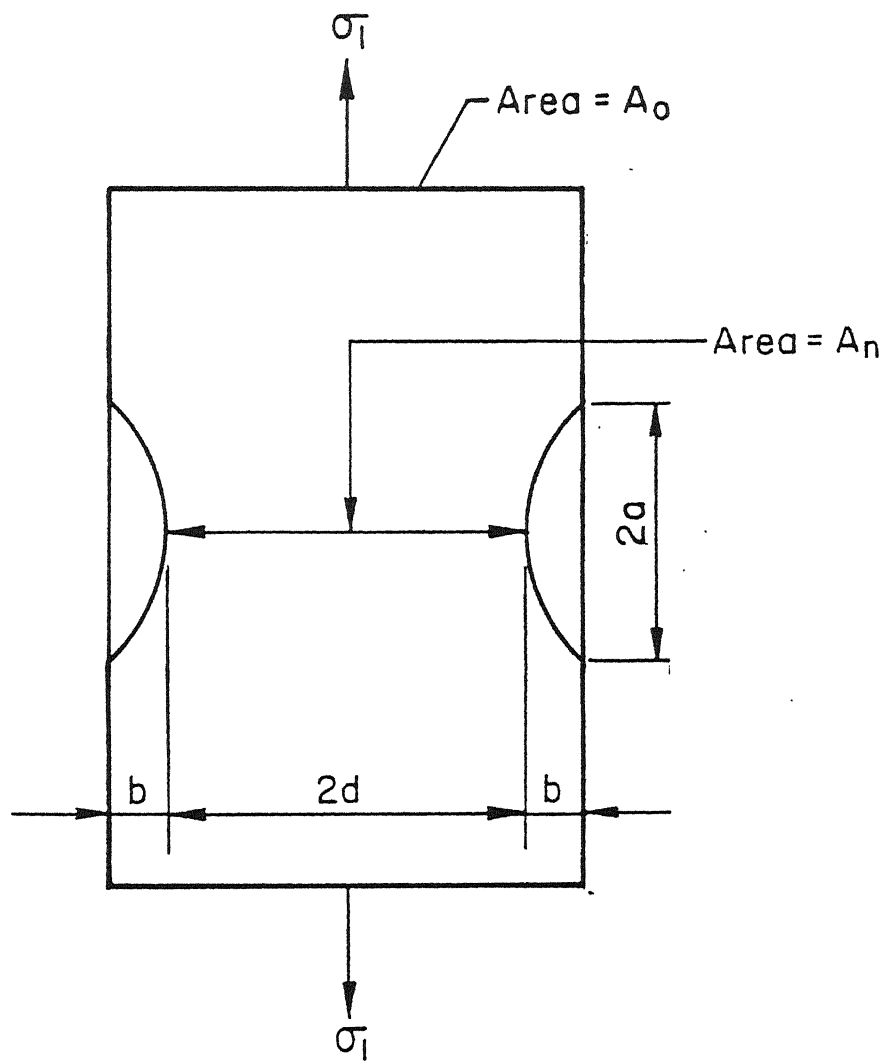locity field (after P. F. Thomson [26]).

Fig. 2.3 Unit cell

Chapter 3

FINITE ELEMENT FORMULATION

3.1   Introduction

In this chapter a nonlinear finite element formulation has been developed using updated Lagrangian approach. An elastic-plastic matrix relating incremental stress and strain is derived using the plastic potential proposed in Chapter 2 for a damaged material. Geometric non linear relationship between strain and displacement is introduced in the finite element formulation following a procedure given by Bathe [47]. Finally the numerical schemes, required to implement the finite element formulation, are discussed.

3.2   Introduction to Non-linear Analysis

In linear elastic finite element formulation, we assume that the displacements and their derivatives are infinitesimally small and the material is linearly elastic. The former assumption leads to the condition that the strain displacement matrix $[B]$ of each element is independent of nodal displacements. Moreover, the stress strain matrix $[C]$ also remains constant for a linearly elastic material over the entire loading. The finite element

equilibrium equations become

$$[K]\underline{U} = \underline{F} \tag{3.1}$$

where $[K]$ is the global stiffness matrix and $\underline{U}$ and $\underline{F}$ are the global displacement and load vectors respectively. The global stiffness matrix is an assemblage of the element stiffness matrices, i.e.

$$[K] = \sum_e [K_e] \tag{3.2}$$

where

$$[K_e] = \int_V [B]^T [C][B] dv. \tag{3.3}$$

Here, V is the volume of the element and the summation is to be carried out after expanding the matrices $[K_e]$. Since the matrix equation (3.1) is a set of linear equations, the displacements are linear functions of load.

In nonlinear finite element analysis, we encounter two types of nonlinearities , namely the material nonlinearity and the geometric nonlinearity. The Ist kind deals with the nonlinearity in material stress strain relation. Thus $[C]$ matrix becomes a function of the current state of stress. The other type of nonlinearity comes from the nonlinear relation between the strain and the displacement which is predominant in large deformation and rotation. Here the strain displacement matrix $[B]$ becomes dependent on displacement. Thus different problems can be categorised in the following manner.

Nature of the problem	_Catagory_
(a)_Elastic analysis with small strain_	_Linear in both material and geometric relation._
(b)_Elastic analysis with large deformation and rotation._	_Geometrically nonlinear only._
(c)_Elastic − plastic with small strain_	_Materially nonlinear only._
(d)_Elastic − plastic with large deformation and rotation_	_Nonlinear in both material and geometric relations._

3.3 Elastic-Plastic Analysis with Large Deformation/Rotation

3.3.1 Incremental Stress-strain Relationship representing Material Nonlinearity

Since the stress-strain relationship is path dependent for an elastic-plastic material, it is convenient to represent it in incremental form. The incremental stress-strain relation is expressed as

$$d\underline{\sigma} = \left[C^{EP}\right] d\underline{\epsilon} \tag{3.4}$$

where $d\underline{\sigma}$ and $d\underline{\epsilon}$ are the incremental stress and strain written in vector form. The expression for the elastic-plastic matrix $\left[C^{EP}\right]$ is derived from the plastic potential F. Initially, we shall derive the expression for $\left[C^{EP}\right]$ for a material without damage. Since D is zero for such materials, the expressions (2.46) and (2.47) for the plastic potential reduce to

$$F = F_1 = \sigma_{eq} - \sigma_y \tag{3.5}$$

where now the yield stress is given by

$$\sigma_y = (R + \sigma_o). \tag{3.6}$$

Note that F depends on the Cauchy stress tensor σ_{ij} through σ_{eq} and the isotropic hardening variable p through σ_y (the variable p has been defined in the previous chapter by equations 2.15 - 2.16). For the derivation of $\left[C^{EP}\right]$ matrix, it is convenient to express σ_{ij} in a vector form $\underline{\sigma}$:

$$\underline{\sigma}^T = \{\sigma_{11}, \sigma_{22}, \ldots\}. \tag{3.7}$$

Now the (von Mises) yield condition can be expressed as

$$F(\underline{\sigma},\, p) = \sigma_{eq}(\underline{\sigma}) - \sigma_y(\,p\,) = 0. \tag{3.8}$$

On the yield surface, $dF = 0$ and hence

$$\left(\frac{\partial F}{\partial \underline{\sigma}}\right)^T d\underline{\sigma} + \frac{\partial F}{\partial p}dp = 0, \tag{3.9}$$

or

$$\underline{a}^T d\underline{\sigma} - A\lambda dt = 0 \qquad (3.10)$$

where, the flow vector $\underline{a}$ is defined by

$$\underline{a} = \frac{\partial F}{\partial \underline{\sigma}}, \qquad (3.11)$$

the parameter A is given by

$$A = -\frac{1}{\lambda dt}\frac{\partial F}{\partial p}dp. \qquad (3.12)$$

and λ is the same scalar which appears in equations (2.24 - 2.26). When $D = 0$ (i.e. when $F = F_1$), equations (2.48) and (2.51) give the following expressions for the flow vector $\underline{a}$ and the scalar λ :

$$\underline{a} = \frac{3}{2\sigma_{eq}}\underline{\sigma}', \qquad (3.13)$$

$$\lambda = \dot{\epsilon}^p_{eq}. \qquad (3.14)$$

Here $\underline{\sigma}'$ is the vector form of the deviatoric part of σ_{ij}. Equation (2.15) gives

$$dp = \dot{\epsilon}^p_{eq}dt. \qquad (3.15)$$

Substitution of equations (3.8), (3.14) and (3.15) in (3.12) leads to the following expression for A :

$$A = \frac{d\sigma_y}{dp} = \frac{d\sigma_y}{d\epsilon^p_{eq}} \qquad (3.16)$$

The total strain increment can be split into elastic and plastic parts. Thus,

$$
\begin{aligned}
d\underline{\epsilon} &= d\underline{\epsilon}^e + d\underline{\epsilon}^p \\
&= [C]^{-1}d\underline{\sigma} + \lambda dt \, \frac{\partial F}{\partial \underline{\sigma}} \\
&= [C]^{-1}d\underline{\sigma} + \lambda dt \, \underline{a}. \qquad (3.17)
\end{aligned}
$$

Here, $[C]$ is the matrix form of the elasticity tensor C_{ijkl} (see equation 2.3). The 2nd part of the right hand side of equation(3.17) is due to the flow rule (equation 2.24).

Pre-multiplying both sides of equation (3.17) by $\underline{a}^T[C]$ and using equation (3.10) one can get

$$\lambda dt = \frac{\underline{a}^T [C] d\underline{\epsilon}}{A + \underline{a}^T [C] \underline{a}}. \tag{3.18}$$

Thus,

$$d\underline{\epsilon} = [C]^{-1} d\underline{\sigma} + \frac{\underline{a}^T [C] d\underline{\epsilon}}{A + \underline{a}^T [C] \underline{a}} \underline{a} \tag{3.19}$$

which leads to

$$d\underline{\sigma} = \left[[C] - \frac{[C] \underline{a}\, \underline{a}^T [C]}{A + \underline{a}^T [C] \underline{a}} \right] d\underline{\epsilon}. \tag{3.20}$$

Therefore,

$$[C^{EP}] = \left[[C] - \frac{[C] \underline{a}\, \underline{a}^T [C]}{A + \underline{a}^T [C] \underline{a}} \right] \tag{3.21}$$

where the definitions of $[C]$, $\underline{a}$ and A are as before. The expression for $\underline{a}$ is given by equation (3.13). For a material with power strain hardening law (equation 2.57), the expression (3.16) for A becomes

$$A = K\, n\, \left(\epsilon_{eq}^p \right)^{n-1}. \tag{3.22}$$

For an isotropic material, the expression for $[C]$ for the 3-D case is given by

$$[C] = \frac{E}{(1+\nu)(1-2\nu)} \begin{bmatrix} 1-\nu & \nu & \nu & 0 & 0 & 0 \\ \nu & 1-\nu & \nu & 0 & 0 & 0 \\ \nu & \nu & 1-\nu & 0 & 0 & 0 \\ 0 & 0 & 0 & \frac{1-2\nu}{2} & 0 & 0 \\ 0 & 0 & 0 & 0 & \frac{1-2\nu}{2} & 0 \\ 0 & 0 & 0 & 0 & 0 & \frac{1-2\nu}{2} \end{bmatrix}. \tag{3.23}$$

From this, one can easily extract the expression for either the axisymmetric case or the plane strain case.

The tensor form of the incremental relation (3.4) can be expressed as

$$d\sigma_{ij} = C_{ijkl}^{EP} d\epsilon_{kl} \tag{3.24}$$

where $d\sigma_{ij}$ is the incremental stress tensor, ϵ_{kl} is the incremental infinitesimal strain tensor and C_{ijkl}^{EP} is the (fourth order) tensor form of $[C^{EP}]$ matrix. The tensor $d\sigma_{ij}$ should be an objective stress tensor i.e. it should not be affected by a rigid body motion. Therefore $d\sigma_{ij}$ can not be interpreted as an incremental Cauchy stress tensor. Two commonly used objective stress tensor in the literature are the 2nd Piola-Kirchoff stress tensor S_{ij} and the tensor based on Jaumann stress rate $\overset{\triangledown}{\sigma}_{ij}$. The definitions of the tensors are given in the following sections. Thus $d\sigma_{ij}$ should either be dS_{ij} or $\overset{\triangledown}{\sigma}_{ij}dt$ (Here dt is the incremental time).

For a damaged material, the plastic potential is given by equations (2.46 - 2.47). When a similar derivation is carried out starting from equations (2.46 - 2.47), we get the following expression for the $[C^{EP}]$ matrix.

$$\left[C^{EP}\right] = \left[[C] - \frac{[C]\,\underline{a}\,\underline{a}^T\,[C]}{A + \underline{a}^T\,[C]\,\underline{a}}\right] (\,1 - D\,). \tag{3.25}$$

3.3.2 Updated Lagrangian Formulation for Geometric Non-linearity

When a body experiences large deformation and/or rotation, the equilibrium must be established in the current configuration. The normal solution procedure adopted in this case is updated Lagrangian. That is to say that when all the kinematical variables are known from time 0 to time t in discreate time steps, the objective is to establish the equilibrium in the configuration at time $t + \Delta t$.

In order to derive the finite element equilibrium equations at time $t + \Delta t$, the principle of virtual work requires that

$$\int_{V^t} {}_{t+\Delta t}\sigma_{ij}^{t+\Delta t}\, \delta\, {}_{t+\Delta t}\epsilon_{ij}^{t+\Delta t}\, dv^{t+\Delta t} = R^{t+\Delta t} \tag{3.26}$$

where ${}_{t+\Delta t}\sigma_{ij}^{t+\Delta t}$ is the Cauchy stress tensor at time $t + \Delta t$, ${}_{t+\Delta t}\epsilon_{ij}^{t+\Delta t}$ is the infinitesimal strain tensor at time $t + \Delta t$, $R^{t+\Delta t}$ is the virtual work of the external body and surface forces at time $t + \Delta t$, $V^{t+\Delta t}$ is the domain at time $t + \Delta t$ and $dv^{t+\Delta t}$ is a volume element

at time $t + \Delta t$. The major difficulty in application of equation (3.26) is that the configuration at $t + \Delta t$ is unknown. Moreover quantities like Cauchy stress tensor are not purely additive as now one has to take care of rotation into account.

An elegant way of formulating the problem is given by Bathe [47]. Here, the virtual work expression (equation 3.26) is written in terms of 2nd Piola Kirchoff stress tensor and Green Lagrange strain tensor which are energetically conjugate to each other. Thus, for updated Lagrangian formulation, the virtual work expression is written as

$$\int_{V^t} {}_t S_{ij}^{t+\Delta t} \, \delta \, {}_t e_{ij}^{t+\Delta t} \, dv^t = R^{t+\Delta t}. \tag{3.27}$$

The right superscript stands for the current configuration and the left subscript stands for the reference configuration. S_{ij} denotes 2nd Piola Kirchoff stress tensor whose relation with Cauchy stress tensor σ_{ij} is given by

$$_t S_{ij}^{t+\Delta t} = \frac{\rho^t}{\rho^{t+\Delta t}} \, {}_{t+\Delta t} x_{i,m}^t \sigma_{mn}^{t+\Delta t} \, {}_{t+\Delta t} x_{j,n}^t. \tag{3.28}$$

Since Cauchy stress tensor is always referred to the current configuration, the left subscript has been omitted. Here ${}_{t+\Delta t} x_{i,m}^t$ represents the derivative of the position vector at time t with respect to one at time $t + \Delta t$ and $\rho^t/\rho^{t+\Delta t}$ denotes the ratio of densities at time t and $t + \Delta t$. The Green-Lagrange strain tensor ${}_t e_{ij}^{t+\Delta t}$ is defined as

$$_t e_{ij}^{t+\Delta t} = \frac{1}{2} \left({}_t u_{i,j}^{t+\Delta t} + {}_t u_{j,i}^{t+\Delta t} + {}_t u_{k,i}^{t+\Delta t} \, {}_t u_{k,j}^{t+\Delta t} \right) \tag{3.29}$$

where ${}_t u_{i,j}^{t+\Delta t}$ is the derivative of the displacement vector from time t to $t + \Delta t$ with respect to the position vector at time t.

An incremental decomposition of stress and strain gives

$$
\begin{aligned}
_t S_{ij}^{t+\Delta t} &= {}_t S_{ij}^t +_t \Delta S_{ij} \\
&= \sigma_{ij}^t +_t \Delta S_{ij},
\end{aligned} \tag{3.30}
$$

$$_t e_{ij}^{t+\Delta t} =_t \Delta \epsilon_{ij} +_t \Delta \eta_{ij}, \tag{3.31}$$

where,

$$_t\Delta\epsilon_{ij} = \frac{1}{2}\left(_t\Delta u_{i,j} +_t \Delta u_{j,i}\right) \tag{3.32}$$

and,

$$_t\Delta\eta_{ij} = \frac{1}{2}\,_t\Delta u_{k,i}\,_t\Delta u_{k,j}. \tag{3.33}$$

Here $_t\Delta u_{i,j}$ stands for the derivative of $_t\Delta \underline{u}$ (incremental displacement vector at time t) with respect to $_t\underline{x}$ (position vector at time t). Thus, equation(3.27) can be written with incremental decomposition as

$$\int_{V^t} {}_t\Delta S_{ij}\,\delta(\,_t\Delta\epsilon_{ij})\,dv^t + \int_{V^t} {}_t\Delta S_{ij}\,\delta(\,_t\Delta\eta_{ij})\,dv^t + \int_{V^t} \sigma_{ij}^t\,\delta(\,_t\Delta\eta_{ij})\,dv^t =$$
$$R^{t+\Delta t} - \int_{V^t} \sigma_{ij}^t\,\delta(\,_t\Delta\epsilon_{ij})\,dv^t. \tag{3.34}$$

The 2nd integral on the left hand side is a higher order term compared to other terms and hence can be neglected. More over, using an elastic-plastic incremental stress-strain relationship (equation 3.24), the Ist term can be approximated as $\int_{V^t} {}_tC^{EP}_{ijkl}\,{}_t\Delta\epsilon_{kl}\,\delta(_t\Delta\epsilon_{ij})dv^t$. The left subscript of C^{EP}_{ijkl} denotes the time at which it is to be evaluated. The above simplification will definitely give rise to an error in the right hand side of the equation (3.34). The error is normally neutralised by using some iterative scheme like Newton Raphson Method. Thus, equation (3.34) can be written as

$$\int_{V^t} {}_tC^{EP}_{ijkl}\,{}_t\Delta\epsilon_{kl}\,\delta(\,_t\Delta\epsilon_{ij}\,)\,dv^t + \int_{V^t} \sigma_{ij}^t\,\delta(\,_t\Delta\eta_{ij}\,)\,dv^t =$$
$$R^{t+\Delta t} - \int_{V^t} \sigma_{ij}^t\,\delta(\,_t\Delta\epsilon_{ij}\,)\,dv^t. \tag{3.35}$$

Owing to the symmetries in C^{EP}_{ijkl}, ϵ_{ij}, η_{ij} and σ_{ij}, the equation (3.35) can be rewritten in the following form:

$$\int_{V^t} \left(\delta\,_t\Delta\underline{\epsilon}^T\right)\,_t[C]^{EP}\,_t\Delta\underline{\epsilon}\,dv^t + \int_{V^t} \left(\delta\,_t\Delta\underline{\eta}^T\right)\,[T]^t\,_t\Delta\underline{\eta}\,dv^t =$$
$$R^{t+\Delta t} - \int_{V^t} \left(\delta\,_t\Delta\underline{\epsilon}^T\right)\underline{\sigma}^t\,dv^t \tag{3.36}$$

where,

$$_t\Delta\underline{\epsilon} = (_t\Delta\epsilon_{11},\ _t\Delta\epsilon_{22},\ _t\Delta\epsilon_{33}, 2\ _t\Delta\epsilon_{12}, 2\ _t\Delta\epsilon_{23}, 2\ _t\Delta\epsilon_{31})^T, \tag{3.37}$$

$$\underline{\sigma}^t = (\sigma_{11}^t,\ \sigma_{22}^t,\ \sigma_{33}^t,\ \sigma_{12}^t,\ \sigma_{23}^t,\ \sigma_{31}^t)^T, \tag{3.38}$$

$$_t\Delta\underline{\eta} = (\ _t\Delta u_{1,1}\ _t\Delta u_{1,2}\ _t\Delta u_{1,3}\ _t\Delta u_{2,1}\ _t\Delta u_{2,2}\ _t\Delta u_{2,3}\ _t\Delta u_{3,1}\ _t\Delta u_{3,2}\ _t\Delta u_{3,3}\ )^T. \tag{3.39}$$

$$[T]^t = \begin{bmatrix} \sum^t & 0 & 0 \\ 0 & \sum^t & 0 \\ 0 & 0 & \sum^t \end{bmatrix} \tag{3.40}$$

and

$$\overset{t}{\sum} = \begin{bmatrix} \sigma_{11}^t & \sigma_{12}^t & \sigma_{13}^t \\ \sigma_{21}^t & \sigma_{22}^t & \sigma_{23}^t \\ \sigma_{31}^t & \sigma_{32}^t & \sigma_{33}^t \end{bmatrix}. \tag{3.41}$$

The $_t[C^{EP}]$ matrix is the elastic-plastic matrix evaluated at time t which is given by equation (3.21) or (3.25).

3.4   FEM Equations

The domain is discretised into a number of elements and the displacement field within each element is approximated as

$$_t\Delta\underline{u} = [Q]\ _t\Delta\underline{u}^e \tag{3.42}$$

where,

$$_t\Delta\underline{u}^e = (\Delta u_1^1,\ \Delta u_2^1,\ \Delta u_3^1,\ \dots\ ,\Delta u_1^n,\ \Delta u_2^n,\ \Delta u_3^n)^T$$

and Δu_1^i, Δu_2^i, Δu_3^i stand for incremental displacements of node 'i' in x, y, z directions respectively. Here

$$[Q] = \begin{bmatrix} \underline{Q}_1^T \\ \underline{Q}_2^T \\ \underline{Q}_3^T \end{bmatrix} \tag{3.43}$$

where,

$$\underline{Q}_1^T = [N_1 \quad 0 \quad 0 \quad N_2 \quad 0 \quad 0 \quad \ldots \quad N_n \quad 0 \quad 0],$$

$$\underline{Q}_2^T = [0 \quad N_1 \quad 0 \quad 0 \quad N_2 \quad 0 \quad \ldots \quad 0 \quad N_n \quad 0],$$

$$\underline{Q}_3^T = [0 \quad 0 \quad N_1 \quad 0 \quad 0 \quad N_2 \quad \ldots \quad 0 \quad 0 \quad N_n].$$

With displacement field defined by equation (3.42), the strain field within the element can be calculated in terms of nodal displacements. From equation (3.42),

$$_t\Delta u_{i,j} = \frac{\partial \, _t\Delta u_i}{\partial \, _t x_j} = \, _t\underline{Q}_{i,j}^T \, _t\Delta \underline{u}^e \tag{3.44}$$

where

$$_t\underline{Q}_{i,j}^T = \frac{\partial \underline{Q}_i^T}{\partial \, _t x_j}. \tag{3.45}$$

Substituting equation (3.44) in equations (3.32) and (3.33) and arranging them in vector form, one can get the strain displacement relations:

$$_t\Delta \underline{\epsilon} = \, _t[B]_L \, _t\Delta \underline{u}^e, \tag{3.46}$$

$$_t\Delta \underline{\eta} = \, _t[B]_N \, _t\Delta \underline{u}^e \tag{3.47}$$

where,

$$_t[B]_L = \begin{bmatrix} _t\underline{Q}_{1,1}^T \\ \\ _t\underline{Q}_{2,2}^T \\ \vdots \\ _t\underline{Q}_{1,2}^T + \, _t\underline{Q}_{2,1}^T \\ \vdots \end{bmatrix} \tag{3.48}$$

and

$$_t[B]_N = \begin{bmatrix} _t\underline{Q}_{1,1} & _t\underline{Q}_{1,2} & \cdots & \cdots & _t\underline{Q}_{3,3} \end{bmatrix}. \tag{3.49}$$

Using the strain displacement relations derived above, equation (3.36) can be expressed as

$$\sum_e \left\{ \delta(_t\Delta\underline{u}^e)^T \left(\int_{V_e^t} {}_t[B]_L^T {}_t[C]^{EP} {}_t[B]_L \, dv^t \right) {}_t\Delta\underline{u}^e \right\}$$

$$+ \sum_e \left\{ \delta(_t\Delta\underline{u}^e)^T \left(\int_{V_e^t} {}_t[B]_N^T [T]^t {}_t[B]_N \, dv^t \right) {}_t\Delta\underline{u}^e \right\}$$

$$= \sum_e \left\{ \delta(_t\Delta\underline{u}^e)^T \underline{F}^e - \delta(_t\Delta\underline{u}^e)^T \left(\int_{V_e^t} {}_t[B]_L^T \underline{\sigma}^t \, dv^t \right) \right\}. \tag{3.50}$$

Here the term $R^{t+\Delta t}$ has been expressed in terms of the elemental nodal forces $\underline{F}^e$ using a standard procedure. V_e^t is the elemental domain at time t. Expressing the term within Ist parenthesis as linear elemental stiffness $[\,K_L\,]^e$ and that of 2nd one as nonlinear elemental stiffness $[\,K_{NL}\,]^e$ the above equation can be written as

$$\sum_e ([K_L]^e + [K_{NL}]^e) \, _t\Delta\underline{u}^e = \sum_e (\underline{F}^e - \underline{f}^e) \tag{3.51}$$

or

$$\sum_e [K]^e \, _t\Delta\underline{u}^e = \sum_e (\underline{F}^e - \underline{f}^e) \tag{3.52}$$

where

$$\underline{f}^e = \int_{V_e^t} {}_t[B]_L^T \underline{\sigma}^t d\underline{v}^t \tag{3.53}$$

gives the internal force vector. Assembling the elemental matrices $[K]^e$ and the elemental vectors $\underline{F}^e$ and $\underline{f}^e$ over all the elements, we get the following equation.

$$[K] \, _t\Delta\underline{u} = (\underline{F} - \underline{f}). \tag{3.54}$$

Here $[K]$ is the global stiffness matrix, $_t\Delta\underline{u}$ is the global incremental displacement vector (at time t) and $\underline{F}$ and $\underline{f}$ are the global external and internal force vectors respectively.

Equation(3.54), which represents the equilibrium equation in the current configuration, has to be solved iteratively. In an iteration cycle, The R.H.S of equation (3.54) represents the unbalanced force. The iterations are continued till the R.H.S becomes zero. The details of various iteration schemes are described in section 5. In each iteration, first the incremental strain tensor $_t\Delta\epsilon_{ij}$ is calculated from the strain displacement relation (equation 3.46). Then the Jaumann stress rate is calculated from equation (3.24) as

$$\overset{\triangledown t}{\sigma}_{ij} \Delta t = C^{EP}_{ijkl} \, _t\Delta\epsilon_{kl}. \tag{3.55}$$

Finally the Cauchy stress tensor at $t + \Delta t$ is evaluated from

$$\sigma_{ij}^{t+\Delta t} = \sigma_{ij}^{t} + \overset{\nabla}{\sigma}_{ij}^{t}\Delta t + \sigma_{ip}^{t}\Omega_{pj}^{t}\Delta t + \sigma_{jp}^{t}\Omega_{pi}^{t}\Delta t \tag{3.56}$$

where Ω_{ij}^{t} is a spin tensor defined by

$$\Omega_{ij}^{t}\Delta t = \frac{1}{2}\left({}_{t}\Delta u_{j,i} - {}_{t}\Delta u_{i,j} \right). \tag{3.57}$$

3.5   Numerical Scheme

The finite element equation of an elastic-plastic material (equation 3.54) can be solved iteratively by various numerical schemes. Newton Raphson scheme is one of the most commonly used method for such problems. However, if the incremental load step is too large, the error involved in the computation of stress from the $[C^{EP}]$ matrix, evaluated at the previous point, also becomes large [48]. In such a situation, the backward return algorithm can be used to minimize the error. Another limitation of Newton Raphson method is that it often fails to converge in the neighborhood of critical point. In such a situation, the arc length method can be used. These three methods (Newton Raphson method, the backward return algorithm and the arc length method) have been discussed in the next three sub-sections.

Normally we encounter two types of problems in mechanics: (1) Load control problem and (2) Displacement control problem. In a load control problem, the desired deformation is achieved by prescribing a load at a point. On the other hand, in a displacement control problem, it is the prescribed displacement which gives the desired deformation. In a load control problem, if the load falls due to change in geometry, then most iterative schemes fail to converge. Displacement control problems are free from this limitation. In this thesis, only displacement control problems are considered.

3.5.1 The Newton Raphson scheme

The scheme is best described with the help of Fig (3.1) in the following steps. In Fig (3.1), m is an equilibrium point at load level $\underline{P}$. The aim is to reach another equilibrium point $(m+1)$ at a load level $(\underline{P} + \Delta \underline{P})$.

Step1— First of all, the stiffness matrix $[K]$ in equation (3.54) is evaluated using the stresses corresponding to point m. Next, equation (3.54) is solved with $\underline{f} = \underline{0}$ and $\underline{F} = \Delta \underline{P}$ to get an incremental displacement vector $_i\Delta \underline{u}$.

Step 2- From the incremental nodal displacements, incremental strain components are calculated by using equation (3.46). Incremental stresses are calculated from the incremental strains by using suitable constitutive relation. Generally incremental stresses are calculated at the Gauss points of the element. If the point under consideration is in elastic range, the elastic stress strain matrix $[C]$ is used. Otherwise, elastic-plastic matrix $[C^{EP}]$ is used. Since elastic-plastic matrix is dependent on the current state of stress, the stress value at position m is used for the computation of elastic-plastic matrix. The error involved due to this approximation is neutralised by backward return algorithm discussed later. Equation (3.55) is used to calculate Jaumann stress rate and the total Cauchy stress follows from equation (3.56).

Step 3- Once the stresses are calculated at all the Gauss points of all the elements, the internal nodal force vector $\underline{f}$ is calculated. This force corresponds to the equilibrium load at point i in Fig(3.1).

Step 4- Since the applied nodal forces $(\underline{P} + \Delta \underline{P})$ are not equal to internal nodal forces $\underline{f}$, the deformed configuration is not an equilibrium configuration at load level $(\underline{P} + \Delta \underline{P})$. It gives rise to an unbalanced nodal forces $(\underline{P} + \Delta \underline{P} - \underline{f})$.

Step 5- The steps 1 to 3 are repeated with unbalanced nodal forces as the load vector and i as a starting point. Successive repetition of the above steps will lead to the equilibrium point $(m+1)$ for load level $\underline{P} + \Delta \underline{P}$ when the unbalanced nodal forces become

almost zero (less than a pre assinged quantity). In each successive iteration, incremental displacement vector is added to its previous value.

Faster convergence is achieved if the tangential stiffness matrix at each successive equilibrium points is updated. The general practice is to achieve the total load increment in several steps. Within each incremental load step, Newton Raphson iterative scheme is applied with the same tangential stiffness matrix. Stiffness matrix is updated only when going for the next load increment. This modified Newton Raphson scheme is a good compromise between reduced computational time and faster convergence.

3.5.2   The Backward Return Algorithm

Consider the increment from point m to point i. In calculation of the stresses at point i (in step 2 of the Newton Raphson scheme), we use the incremental stress-strain relation (equation 3.4) where the $[C^{EP}]$ matrix is evaluated at point m. When the incremental load step is too large, this gives stresses not at point i but at some point i' which is not on the yield surface (see Fig 3.2). Thus

$$\underline{\sigma}_{i'} = \underline{\sigma}_m + [C^{EP}]_m \, \Delta\underline{\epsilon}. \tag{3.58}$$

A further return is required to bring the stresses to point i. Therefore we can write

$$\underline{\sigma}_i = \underline{\sigma}_{i'} + \Delta\underline{\sigma}. \tag{3.59}$$

To determine $\Delta\underline{\sigma}$, we proceed as follows. From equations (3.18) and (3.21) we note that

$$[C^{EP}]_m \, \Delta\underline{\epsilon} = [C] \, \Delta\underline{\epsilon} - \lambda_m dt \, [C] \, \underline{a}_m. \tag{3.60}$$

Therefore, to bring the stresses to point i, a correction is needed only in the second term. We assume that the correction can be approximated as

$$\Delta\underline{\sigma} = -\lambda_o dt \, [C] \, \underline{a}_{i'}. \tag{3.61}$$

To determine the scalar λ_o, we expand the plastic potential at point i'. Thus,

$$F_i = F_{i'} + \left(\frac{\partial F_{i'}}{\partial \underline{\sigma}}\right)^T \Delta\underline{\sigma} + \frac{\partial F_{i'}}{\partial p}\Delta p + \dots \tag{3.62}$$

Analogous to equation (3.12), we define $A_{i'}$ as

$$A_{i'} = -\frac{1}{\lambda_o dt} \frac{\partial F_{i'}}{\partial p} \Delta p. \tag{3.63}$$

Substituting equations (3.61) and (3.63) in (3.62) and using the definition of flow vector $\underline{a}_{i'}$ (equation 3.11), we get

$$F_i = F_{i'} - \lambda_o dt\ \underline{a}_{i'}^T\ [C]\ \underline{a}_{i'} - \lambda_o dt\ A_{i'}. \tag{3.64}$$

Since the plastic potential has a zero value on the yield surface, $F_i = 0$. Thus

$$\lambda_o dt = \frac{F_{i'}}{\underline{a}_{i'}^T\ [C]\ \underline{a}_{i'} + A_{i'}}. \tag{3.65}$$

Substitution of equations (3.61) and (3.65) in (3.59) gives the following approximate expression for the stress at point i:

$$\underline{\sigma}_i \approx \underline{\sigma}_{i'} - \frac{F_{i'}\ [C]\ \underline{a}_{i'}}{\underline{a}_{i'}^T\ [C]\ \underline{a}_{i'} + A_{i'}}. \tag{3.66}$$

A further expansion will lead to the result

$$\underline{\sigma}_i \approx \underline{\sigma}_{i'} - \frac{F_{i'}\ [C]\ \underline{a}_{i'}}{\underline{a}_{i'}^T\ [C]\ \underline{a}_{i'} + A_{i'}} - \frac{F_{i''}\ [C]\ \underline{a}_{i''}}{\underline{a}_{i''}^T\ [C]\ \underline{a}_{i''} + A_{i''}} - \ldots \tag{3.67}$$

where the point i'' is closer to point i than i' (see Fig 3.2). When the plastic potential at point i becomes less than a pre assigned small number, no additional terms need to be added to equation (3.67).

As a demonstration, Fig (3.3) shows the true stress versus true strain curve for a cylindrical specimen with and without backward return algorithm. The true stress is calculated by dividing the load with the current cross sectional area at the necked region.The true strain (logrithmic strain) is calculated from the formula

$$\epsilon = 2\ln\left(\frac{d_o}{d}\right) \tag{3.68}$$

where d_o and d are the initial and current diameters of the test specimen in the necked portion. Comparison of the curves with the actual curve shows improvement with the backward return algorithm.

3.5.3   The Arc Length Method

The arc length method [49] is described here for a displacement controlled problem in conjunction with Newton Raphson method in its standard or modified version. Proportional loading is assumed but it can be extended to non proportional loading with minor changes.

Notation:

A left superscript indicates the configuration. Therefore, $^{m}\underline{u}$, $^{m}\underline{P}$ ....etc denote the total displacement vector, the load vector .....etc at configuration m. For proportional loading, the loads may be expressed by a single load factor $^{m}\lambda$. Thus.

$$^{m}\underline{P} = {}^{m}\lambda\underline{P} \tag{3.69}$$

where $\underline{P}$ is a basic load vector. Within one increment from configuration m to $(m+1)$, the positions i and $j = (i+1)$ indicate the beginning and the end of an iteration cycle as shown in Fig (3.4). The changes in quantities from i to j (both iterative points) are denoted by $\Delta\underline{u}^{(j)}$, $\Delta\underline{P}^{(j)}$ and $\Delta\lambda^{(j)}$ respectively.

Starting point:

The incremental equation (equation 3.54) at position i may be expressed as

$$^{i}[K]\,\Delta\underline{u}^{(j)} = \Delta\underline{P}^{(j)} + {}^{i}\underline{P} - {}^{i}\underline{f}. \tag{3.70}$$

Denoting the out of balance force by $^{i}\underline{R}$, i.e.

$$^{i}\underline{R} = {}^{i}\underline{P} - {}^{i}\underline{f} \tag{3.71}$$

and using

$$\Delta\underline{P}^{(j)} = \Delta\lambda^{(j)}\underline{P} \tag{3.72}$$

we get

$$^{i}[K]\,\Delta\underline{u}^{(j)} = \Delta\lambda^{(j)}\underline{P} + {}^{i}\underline{R}. \tag{3.73}$$

Procedure for Displacement Control

A simplified method as suggested by Batoz and Dhatt [50] is described here. Since the

equation (3.73) is linear, one can decompose the displacement vector $\Delta \underline{u}^{(j)}$ into two parts as follows:

$$\Delta \underline{u}^{(j)} = \Delta \lambda^{(j)} \Delta \underline{u}^{(j)I} + \Delta \underline{u}^{(j)II} \tag{3.74}$$

where

$$^i[K]\, \Delta \underline{u}^{(j)I} = \underline{P} \tag{3.75}$$

and

$$^i[K]\, \Delta \underline{u}^{(j)II} = {}^i\underline{R}. \tag{3.76}$$

The nth component of the incremental displacement vector $\Delta u_n^{(j)}$ can be expressed as

$$\Delta u_n^{(j)} = \Delta \lambda^{(j)} \Delta u_n^{(j)I} + \Delta u_n^{(j)II}. \tag{3.77}$$

Therefore,

$$\Delta \lambda^{(j)} = \frac{\Delta u_n^{(j)} - \Delta u_n^{(j)II}}{\Delta u_n^{(j)I}}. \tag{3.78}$$

At the start of the iteration, every thing corresponds to the equilibrium point m. Therefore, $^\circ\underline{R} = 0$, $\Delta \underline{u}^{(1)II} = 0$ (from equation 3.76) and thus, $\Delta u_n^{(1)II} = 0$. Hence,

$$\lambda^{(1)} = \Delta \lambda^{(1)} = \frac{\Delta u_n^{(1)}}{\Delta u_n^{(1)I}} \tag{3.79}$$

If we chose the nth component of the displacement vector as the prescribed displacement for the increment then, $\lambda^{(1)}$ becomes the factor for scaling the prescribed displacement $\Delta u_n^{(1)}$ from the displacement $\Delta u_n^{(1)I}$ corresponding to the choice of basic load vector $\underline{P}$. For other iterations, $\Delta u_n^{(j)} = 0$, since $u_n^{(j)}$ is unaltered during iteration cycles. Therefore,

$$\Delta \lambda^{(j)} = -\frac{\Delta u_n^{(j)II}}{\Delta u_n^{(j)I}} \tag{3.80}$$

Note that $\Delta \underline{u}^{(j)I}$ and $\Delta \underline{u}^{(j)II}$ can be calculated by solving equations (3.75) and (3.76). Then, knowing $\Delta \lambda^{(j)}$ from equation (3.80), one can calculate the displacement

increment $\Delta \underline{u}^{(j)}$ with the help of equation (3.74). Then the total dislacement vector at iteration point j becomes

$$^{j}\underline{u} = {}^{i}\underline{u} + \Delta\underline{u}^{(j)}. \tag{3.81}$$

Further, the value of λ at point j is given by

$$^{j}\lambda = {}^{i}\lambda + \Delta\lambda^{(j)}. \tag{3.82}$$

From this one can calculate the total load vector at point j as

$$^{j}\underline{P} = {}^{j}\lambda\underline{P}. \tag{3.83}$$

The stress, strain and other secondary quantities can be calculated from this data using the standard relations.

Unbalanced force (P + ΔP - f)

$P+\Delta P$

P

m

i

(m+1)

Load

Internal force ' f '

$u_i =$

u_m

$u_m + \Delta u$

Displacement
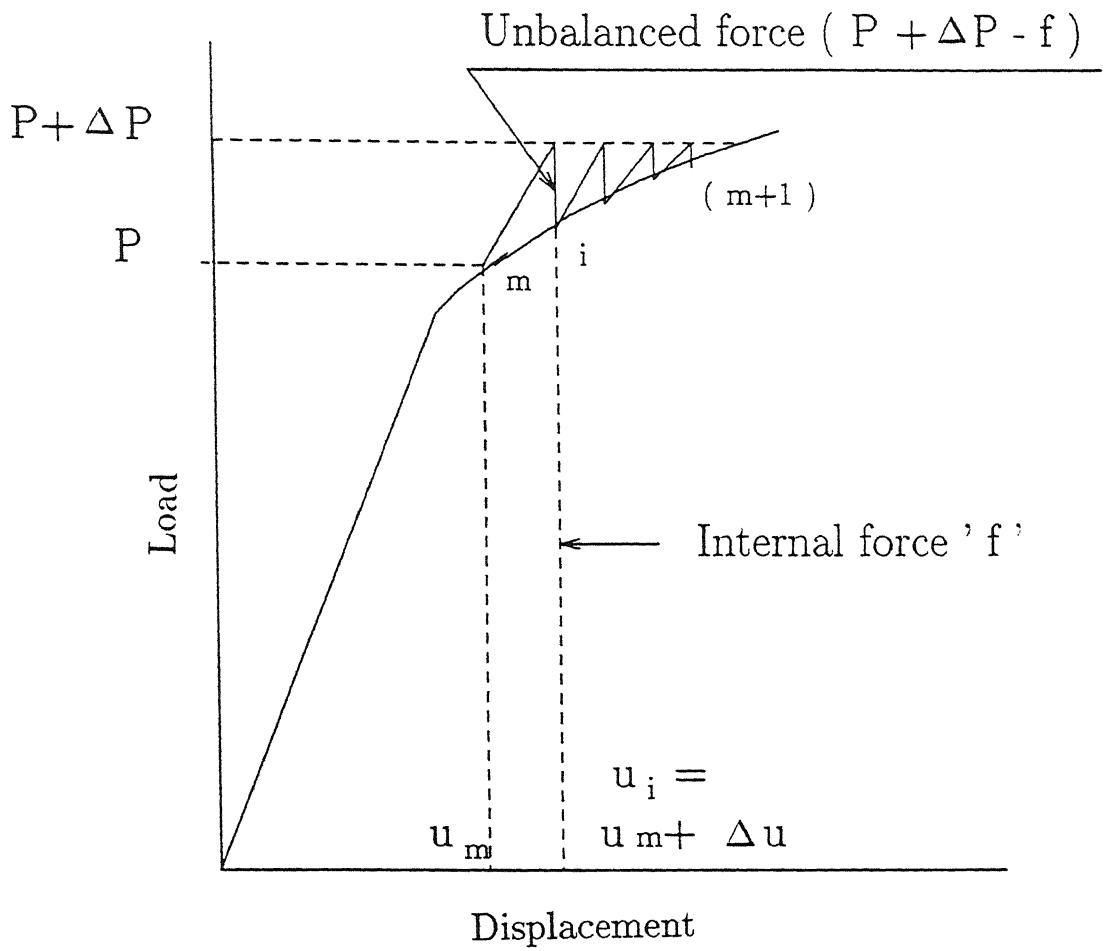
Fig. 3.1 : Illustration of Newton Raphson iterative scheme
for a single load.
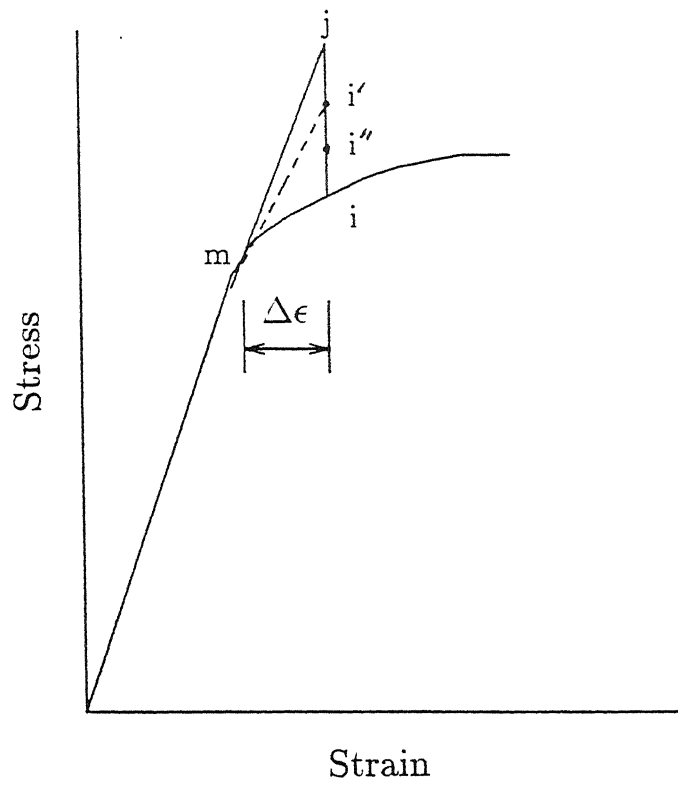
Fig. 3.2 : Illustration of Backward return algorithm
for 1-D problem.
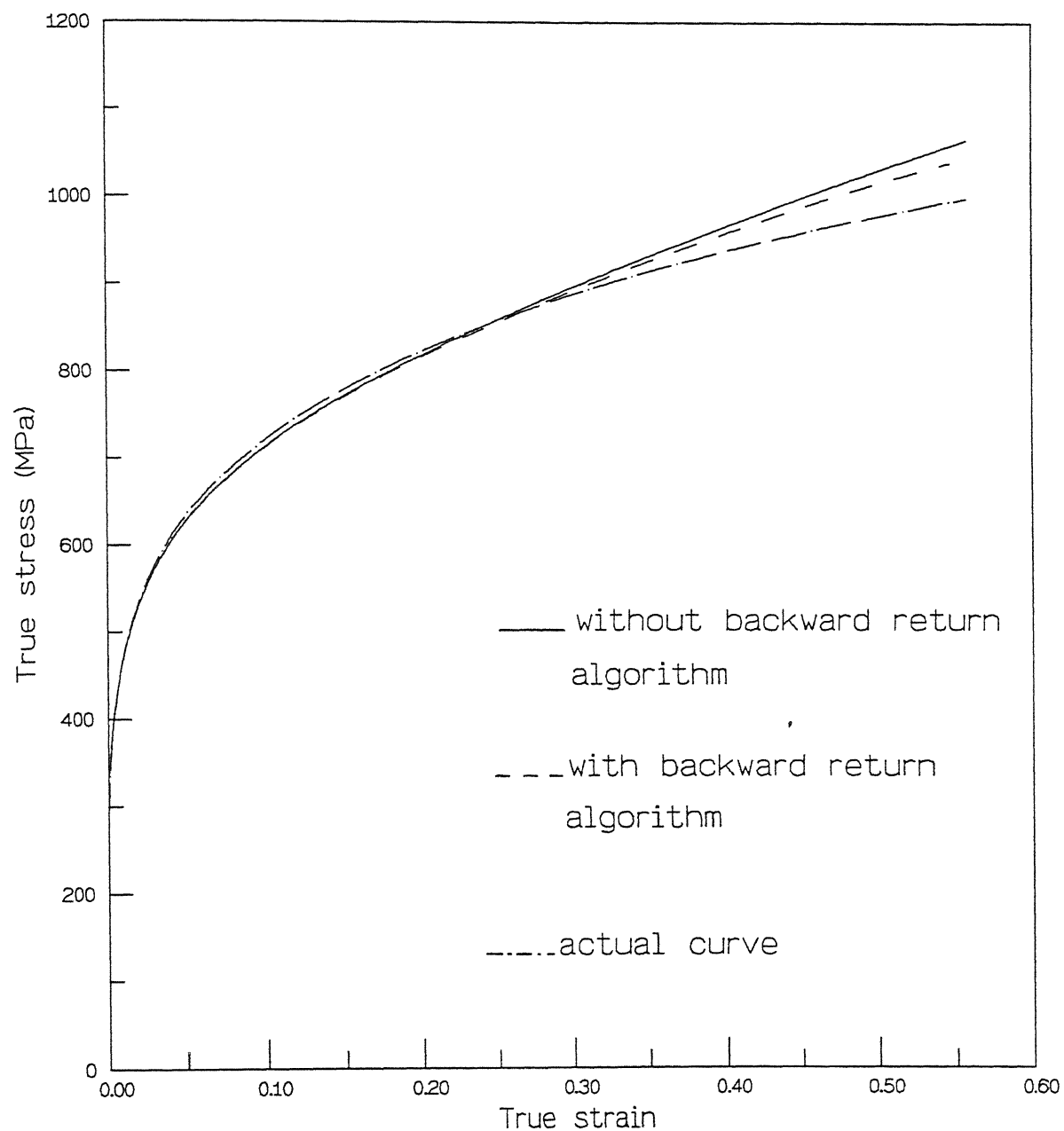
Fig 3.3. Application of Backward return algorithm in cylindrical specimen.
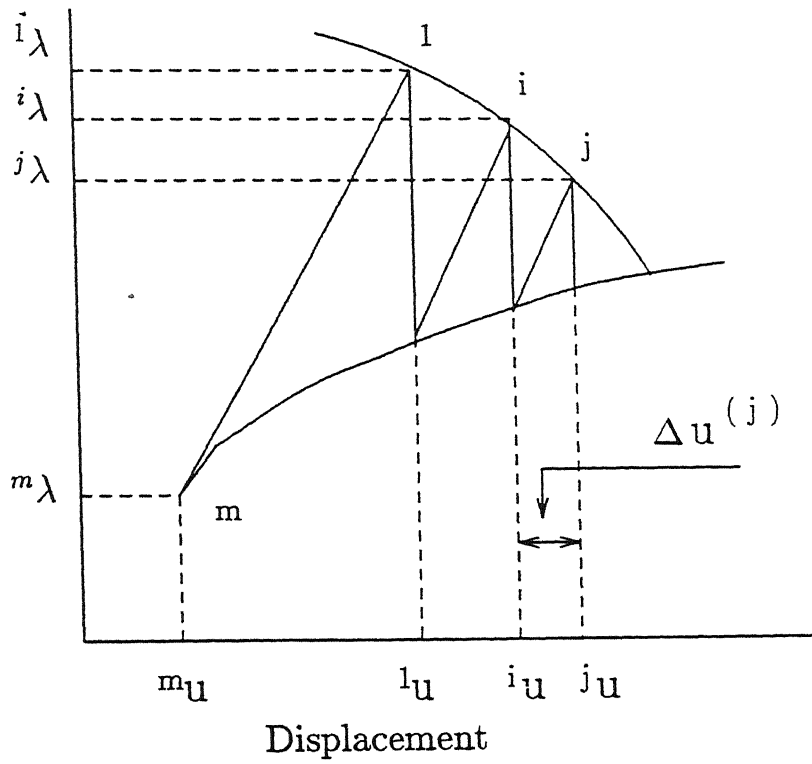
Fig. 3.4 : Illustration of Arc length method
for a single prescribed displacement.

Chapter 4

CASE STUDIES

4.1 Introduction

The updated Lagrangian finite element formulation of a damaged elastic-plastic material developed in the previous Chapter has been applied to a number of cases. The objective of these case studies is to investigate the effects of triaxiallity ($\frac{\sigma_m}{\sigma_{eq}}$), plastic strain and damage variable on ductile fracture process. Finally, using the micro crack initiation criterion based on Thomason's limit load model (Chapter 2), a failure curve is constructed and a ductile fracture parameter is identified which is independent of geometry.

4.2 Finite Element Implementation

The FE formulation developed in Chapter 3 has been implemented in an iterative fashion. That is, equation (3.54) is solved for equilibrium till the unbalanced force in any iteration cycle is zero. The Arc length method in conjunction with Newton Raphson scheme (section 3.5) is used for displacement controlled problems.

A step is defined as the collection of increments of all the quantities between two successive equilibrium states. Within a step there are several iteration cycles. At each

step, the stiffness matrix is calculated by adding its linear and non linear components (equation 3.51). Within a step the stiffness matrix is kept constant and is updated only at the end of each step. Although the stiffness matrix is kept constant for iteration cycles, the internal nodal forces (equation 3.53) and hence the unbalanced forces for each element are calculated with a $[B]_L$ matrix evaluated at the current configuration. For this purpose, nodal coordinates are updated by adding incremental displacement components to achieve the current configuration. Following procedure is adopted for a iteration cycle. Incremental strain components are calculated from incremental displacements using equation (3.46). Next the Jaumann's stress rate is calculated from equation (3.55). The total Cauchy stress follows from equation (3.56). The total displacement increment for the step is achieved by adding the incremental displacements for the iteration cycles.

At the end of each step, the following quantities are calculated. The incremental strain tensor and the incremental equivalent strain for the total step are calculated from the total displacement increment for the step. The equivalent strain, thus obtained, is added to its accumulated value in the previous step to get the total equivalent strain. As the elastic strain is small, the total equivalent strain is treated as the total equivalent plastic strain. The equivalent stress (σ_{eq}), the mean stress (σ_m) and hence the triaxiality ($\frac{\sigma_m}{\sigma_{eq}}$) are calculated from Cauchy stress components. Incremental damage is calculated at the end of the step using the damage growth law (equation 2.60). The incremental damage so obtained is added to its previous value to get the total damage. During elastic unloading, the calculations regarding equivalent plastic strain and the damage are bypassed. For reloading, the calculations for equivalent plastic strain and the damage are restarted from the point of unloading. The load is calculated from the nodal reactions. The programme is terminated when the condition for micro crack initiation by void coalescence (equation 2.80) is satisfied.

4.2.1 Validation of the Programme and the Convergence Study

The elastic-plastic FE programme developed in Chapter 3 is validated with TEPSAC code developed by Tsu [51] for a test problem given in ref [51] . Fig (4.1) shows the geometry, boundary conditions and material properties of the problem. Fig (4.2) shows the load vs radial contraction at the mid-section of the specimen. The FE result obtained from our code matches very well with that given in ref [51]. The Maximum discrepancy is only 3 % which occurs at the maximum load. It is not necessary to perform the damage calculations during this validation study. It should be noted that the stress-strain curve given in ref [51] is approximated by the relation $\sigma_y = K(\epsilon_{eq}^p)^n$.

The convergence study is done for the problem of a cracked plate in plane strain condition. Fig (4.3) shows the geometry and the loading of the problem. The load point displacement and the crack opening displacement (COD) at a point 0.2 mm away from the crack tip, are checked for different crack tip element sizes at the same load level. Table 4.1 shows the results of the convergence study. Fig (4.4) show its graphical representation. It is found from the convergence study that for a crack tip element size not exceeding 0.2 mm, the results are satisfactory in engineering sense.

4.3 Case Studies

4.3.1 General Description of the Problems

The material used in this study is AISI-1090 spherodised steel whose void growth curve for a cylindrical specimen in uniaxial loading is given by LeRoy et al [36]. For the sake of completeness it is reproduced here in Fig (4.5). The chemical composition and the mechanical properties of the material are given in Tables 4.2 and 4.3 respectively. The coefficients a_1 , a_2 and c of the damage growth law (equation 2.60) are obtained as follows. First, equation (2.54) is rearranged as a relation between $\frac{dD}{d\epsilon_{eq}^p}$ and ϵ_{eq}^p using Bridgman's [52] expression for triaxiality ($\frac{\sigma_m}{\sigma_{eq}}$) as a function of strain. Then, from

experimental results of LeRoy et al (Fig 4.5), the slopes $\frac{dD}{d\epsilon_{eq}^p}$ are calculated at different strain levels. Finally, the coefficients a_1 , a_2 and c are obtained by the method of least square curve fitting. The following are the values obtained.

$$a_1 = 9.8 \times 10^{-04} \ MPa^{-1},$$
$$a_2 = 1.84 \ MPa^{-1},$$
$$c = 1.898 \times 10^{-02}. \tag{4.1}$$

Five specimens with different geometries are studied. The geometries of the specimens are shown in Fig (4.6). For all cases except for the cracked plate, a total of 105 eight noded isoparametric elements are used. For the cracked plate, the number of eight noded isoparametric elements is 182 including the crack tip elements. The size of crack tip elements is 0.2 mm × 0.2 mm. The deformed and the undeformed mesh patterns for the cylindrical specimen are shown in Fig (4.7). It is worth noting here that a small imperfection of the order of 0.1% is introduced in the diameter of the mid-section to simulate necking [53] (see the Appendix).

4.3.2   Results and Discussion

To check the accuracy of the result obtained from computer simulation, the simulated results for the cylindrical specimen are compared with the experimental results of LeRoy et al [36]. Fig (4.8) shows the simulated as well as experimental damage growth curve. The simulated curve is obtained by integrating the damage growth rate law up to the failure point. Note that the simulated curve depicts the experimental trend quite well. Further, it is able to predict the damage values with a reasonable engineering accuracy. Fig (4.9) shows the comparison between the simulated true stress-true strain curve with the experimental results of LeRoy et al [36] for the cylindrical specimen. The true stress is calculated by dividing the load with the current area of the necked region. The true strain is calculated from equation (3.68). It is observed from Fig (4.9) that the simulated stress-strain curve matches with the experimental curve very well (The

difference in stress level is only 8% even at a strain level as high as 55%). This shows that the proposed damage growth law (equation 2.60) is consistent with the experimental material behavior.

Fig (4.10) shows the damage growth with equivalent plastic strain up to failure (i.e. up to micro crack initiation) for the five cases. As expected, the damage grows with plastic strain. For all cases except for the cracked plate, the maximum damage occurs at the centre. For the cracked plate, it occurs at the crack tip. The critical values of damage (D_c) and strain ($\epsilon_{eq}^p)_c$ are obtained when equation (2.80) is satisfied. The values of the critical strain and the critical damage for the cylindrical specimen are respectively 60.6% and 5.62%. The reported value of the fracture strain for the cylindrical specimen in ref [36] is 63%. Since the critical strain is close to the experimental value of fracture strain, it shows that the Thomason's model is a good representation of micro crack initiation due to void coalescence.

Fig (4.11) shows the damage versus triaxiality curves for the five cases. It is found that, for the major portion of the deformation, triaxiality remains constant. It means the proportional loading condition has been achieved in all the five cases. This situation arises because the loading is uniaxial tension in all the five cases. Since, the triaxiality function $f(\frac{\sigma_m}{\sigma_{eq}})$ does not change in damage growth rate equation (2.60), the dialatational rate becomes constant. Hence, the nonlinearity in damage growth relation is due to plastic strain only. Although the triaxiality remains constant in each case, its value differs from case to case since it saturates to different critical values for different cases. The maximum critical triaxiality is found at the crack tip of the cracked plate whereas the minimum value occurs for the cylindrical specimen. For the cracked plate, triaxiality increases in the initial part of the deformation due to change in crack tip geometry.

Table 4.4 lists the critical values of strain, triaxiality and damage for the five different cases. It is found that for a wide variation of critical strain and triaxiality, the value of critical damage remains almost constant. Hence, the critical value of damage

(D_c) can be regarded as a geometry independent parameter which indicates the micro crack initiation in ductile solids.

Fig(4.12) shows the variation of triaxiality with equivalent plastic strain for all the five cases. The locus of the failure (or critical) points is called as the failure curve. The failure curve has a qualitative similarity with that of Hancock and Brown [54] but the quantitative comparison is not possible since they have used a different steel. This curve shows that the failure can not be predicted either by critical strain alone or by critical triaxiality alone. Since one has to take both into account, it is better to predict it by critical damage which incorporates both strain and triaxiality. It is observed that critical strain increases with decreasing critical triaxiality. Finally, Fig (4.12) shows that, besides strain, triaxiality also plays an important role in void growth and micro crack initiation.

1
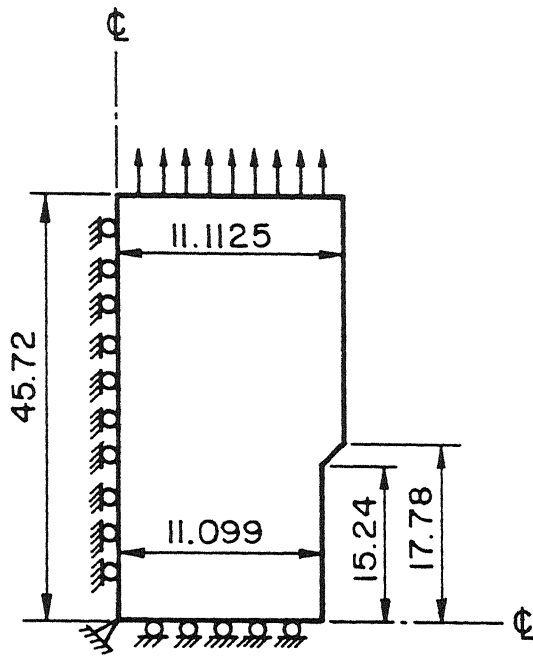
All dimensions are in mm.

Material : Properties

Youngs modulus, $E = 71724$ MPa

Poisson ratio, $\nu = 0.33$

Initial yield strength, $\sigma_0 = 350$ MPa

Hardening parameter, $K = 523.70$ MPa

Hardening exponent, $n = 0.07229$

Fig. 4.1   Geometry and boundary conditions of the test problem.
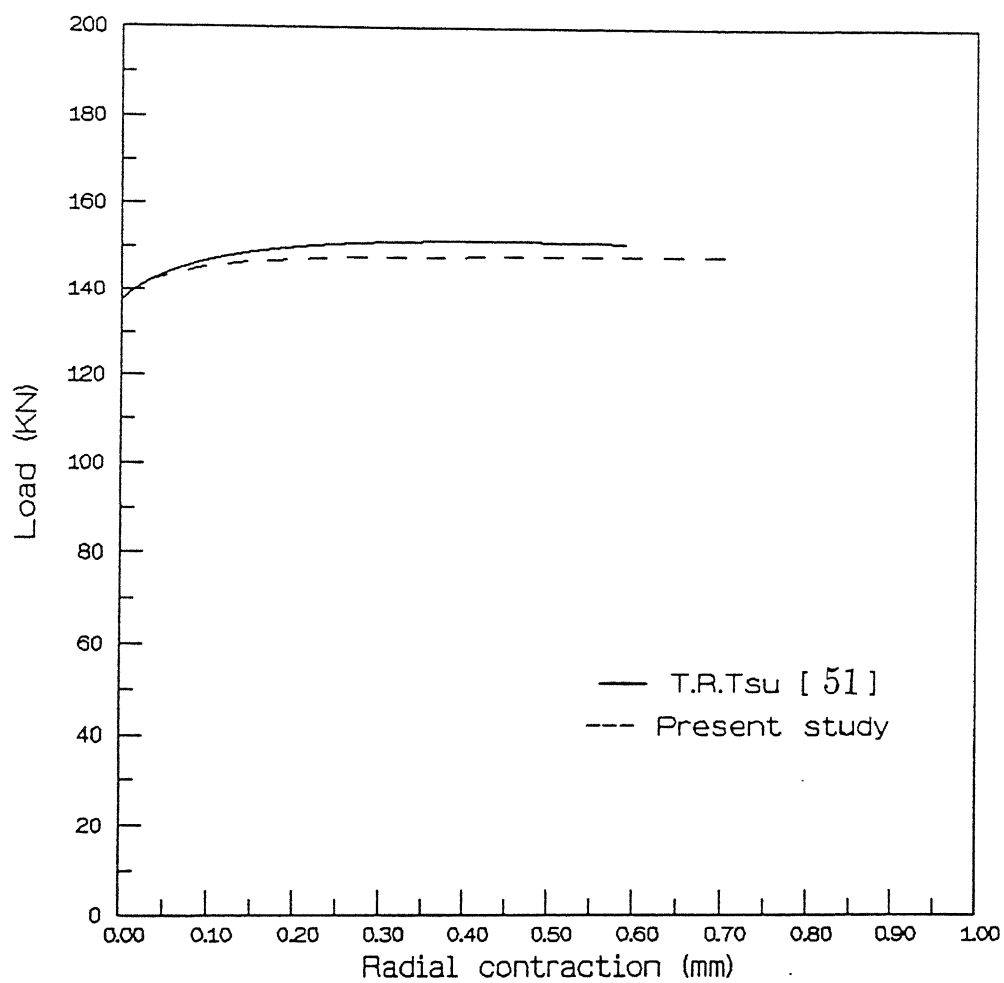
Fig 4.2. load versus radial contraction for the test problem
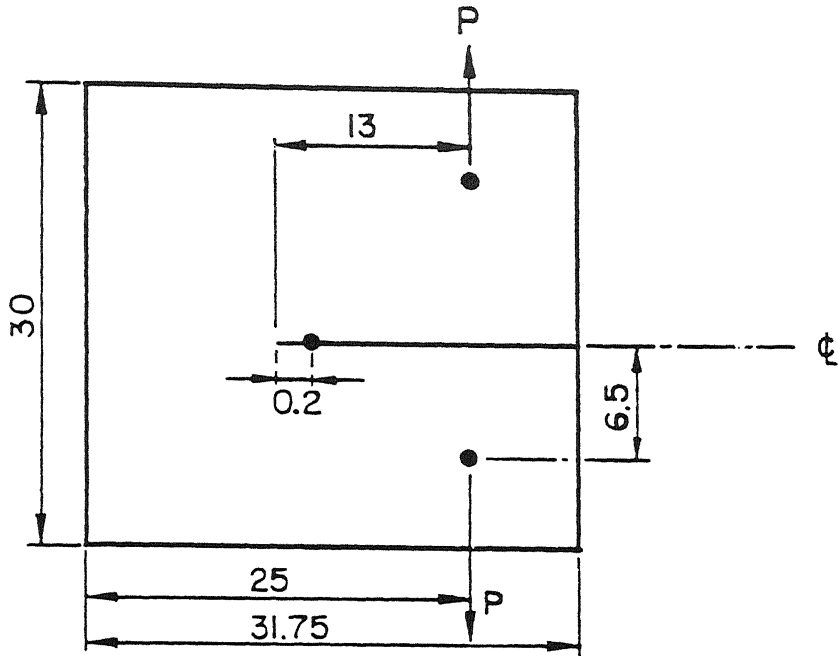
All dimensions are in mm.

Material : AISI 1090 spherodised steel.
Youngs modulus E = 210 GPa
Poisson ratio, ν = 0.3
Yield stress σ_0 = 464 MPa
Hardening parameter K = 1115 MPa
Hardening exponent, n = 0.2.

Fig. 4.3   Geometry and loading of the (1/2 TCT specimen for convergence study.

Sl No	Load (KN)	No of elements	Crack tip element size (mm)	COD (cm)	Load point deflection (cm)
1	17.5	120	0.1×0.1	1.83968×10^{-02}	7.2631×10^{-02}
2	17.5	98	0.2×0.2	1.83940×10^{-02}	7.1469×10^{-02}
3	17.5	66	0.4×0.4	1.53050×10^{-02}	6.6688×10^{-02}

Table 4.1: Results of convergence study
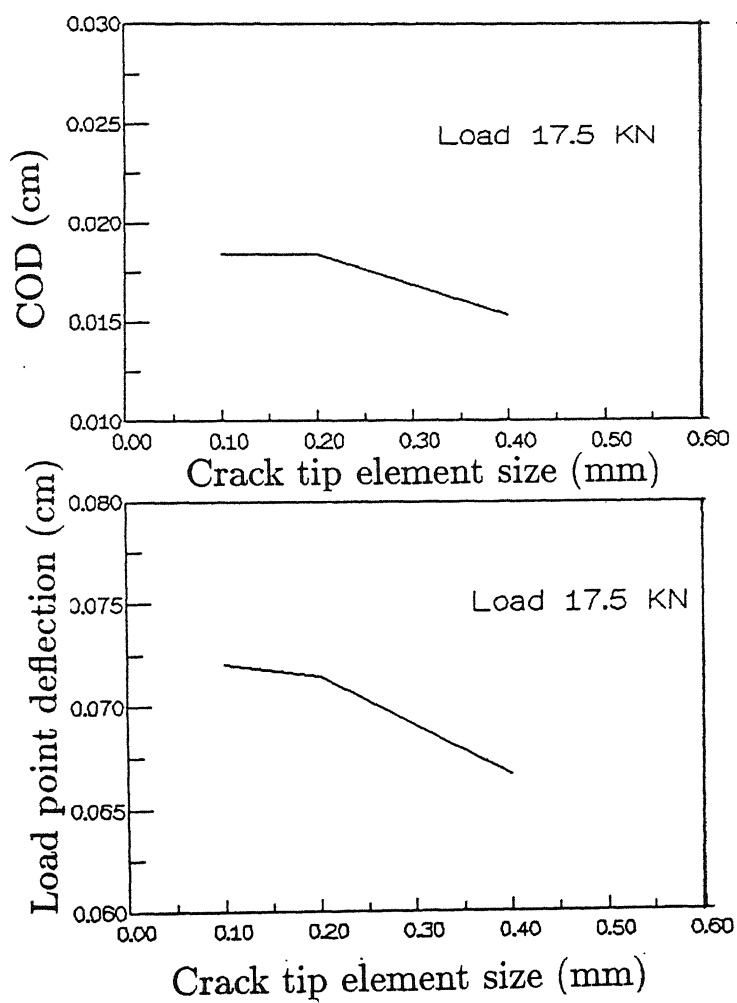
Fig 4.4. Graphical representation of conver-
gence results.
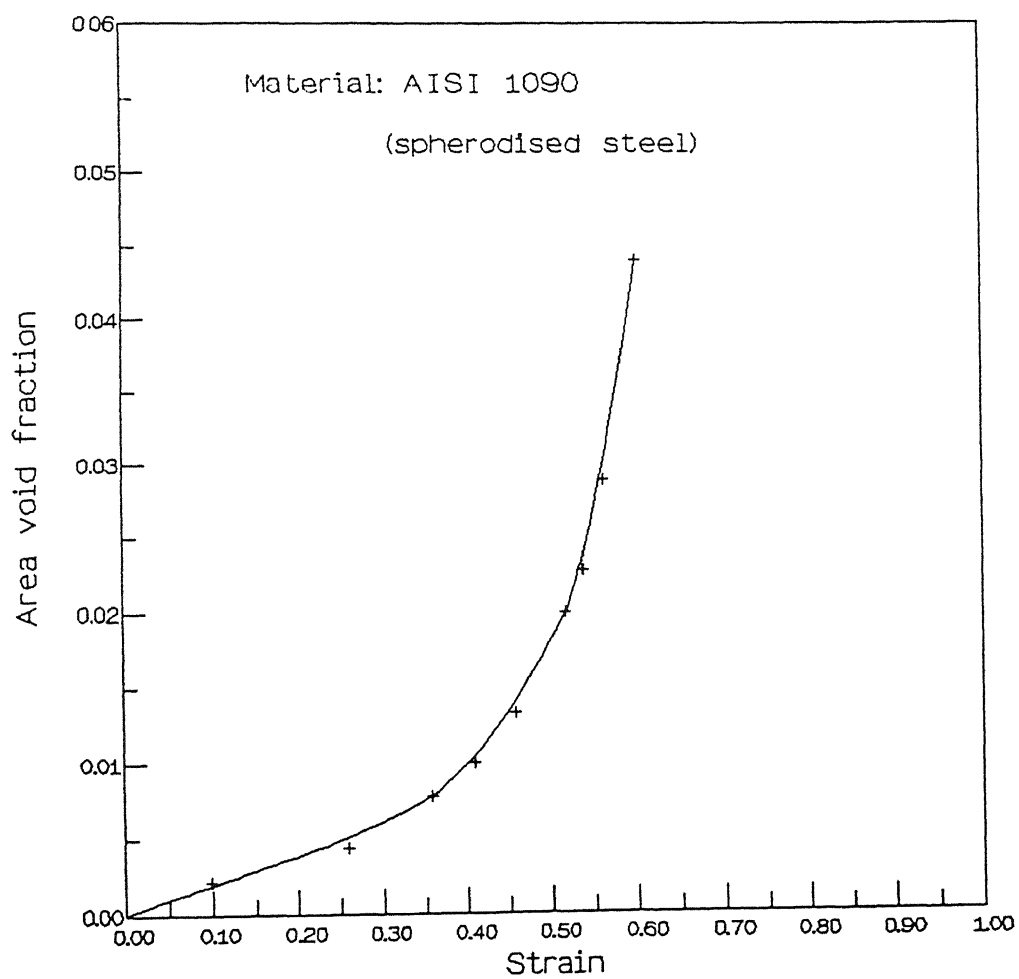
Fig 4.5. Experimental void growth curve, ref [36].

C	Mn	P	S	Si	Fe
0.92	0.72	0.009	0.022	0.20	balance

Table 4.2: Chemical composition (% weight) of Material AISI-1090 steel

poisson's ratio ν	Young modulus E GPa	Yield stress σ_o MPa	Ultimate stress σ_{uts} MPa	Fracture strain ϵ_f	K MPa	n
0.3	210	464	619	0.63	1115	0.19

Table 4.3: Mechanical properties of Material AISI-1090 spherodised steel

(a) Cylindrical
(b) Cylindrical prenecked
(c) Plane strain
(d) Plane strain side grooved
(e) Cracked plate

All dimensions are in mm

Fig. 4.6   Specimen geometry

(a) Undeformed mesh
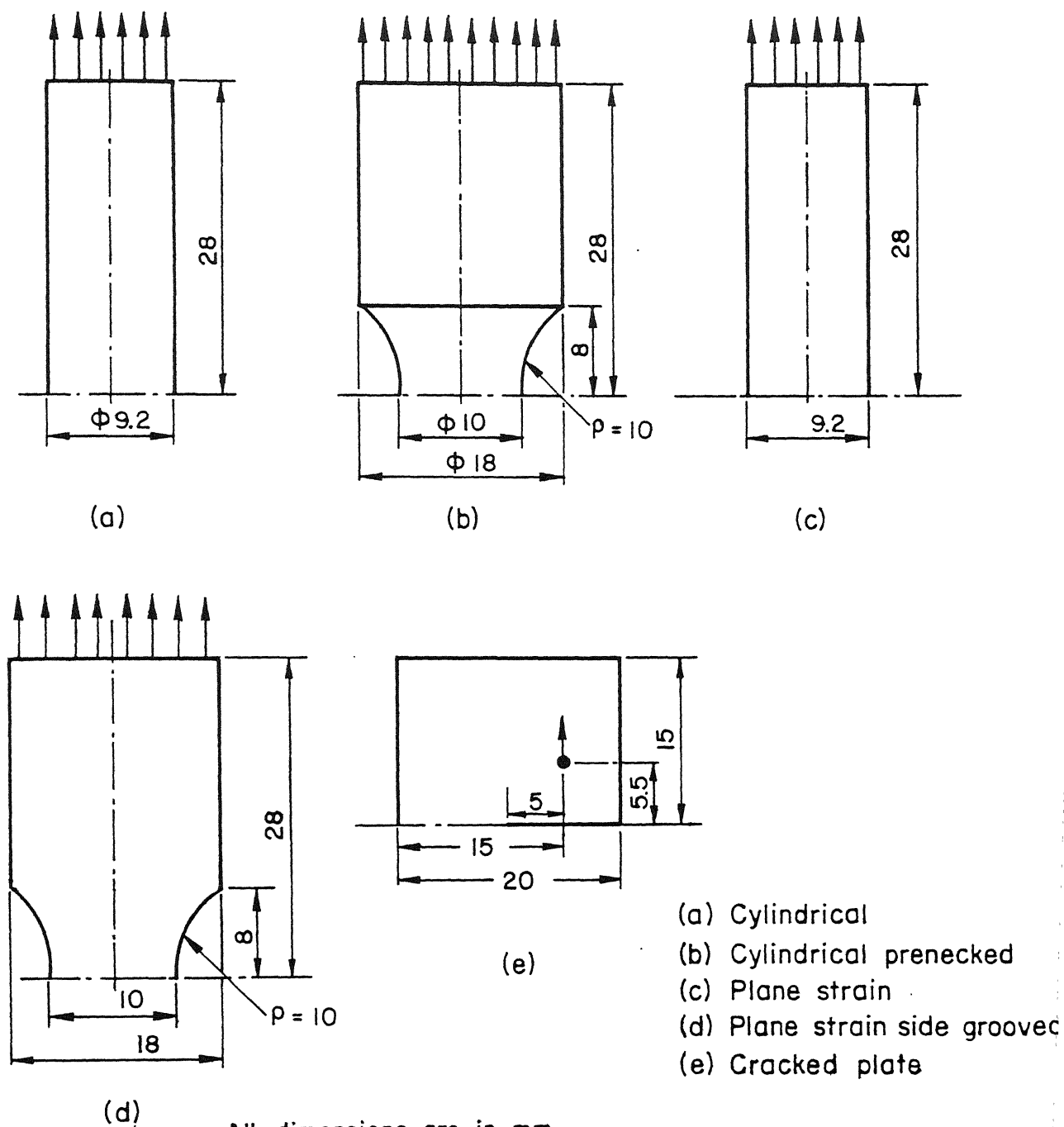
(b) Deformed mesh
at strain level 55%
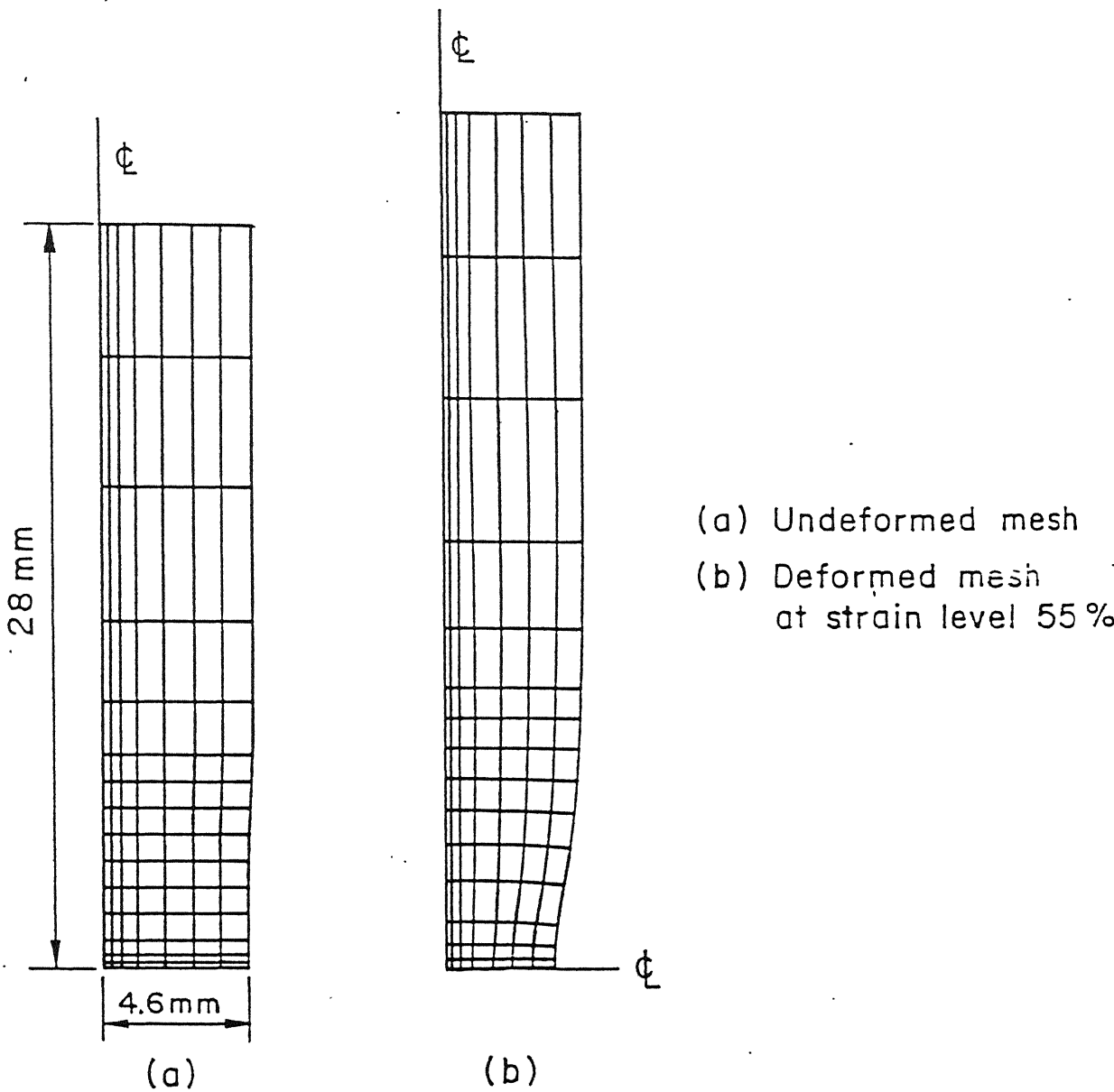
Fig 4.7. Deformed and undeformed mesh patterns for cylindrical specimen.
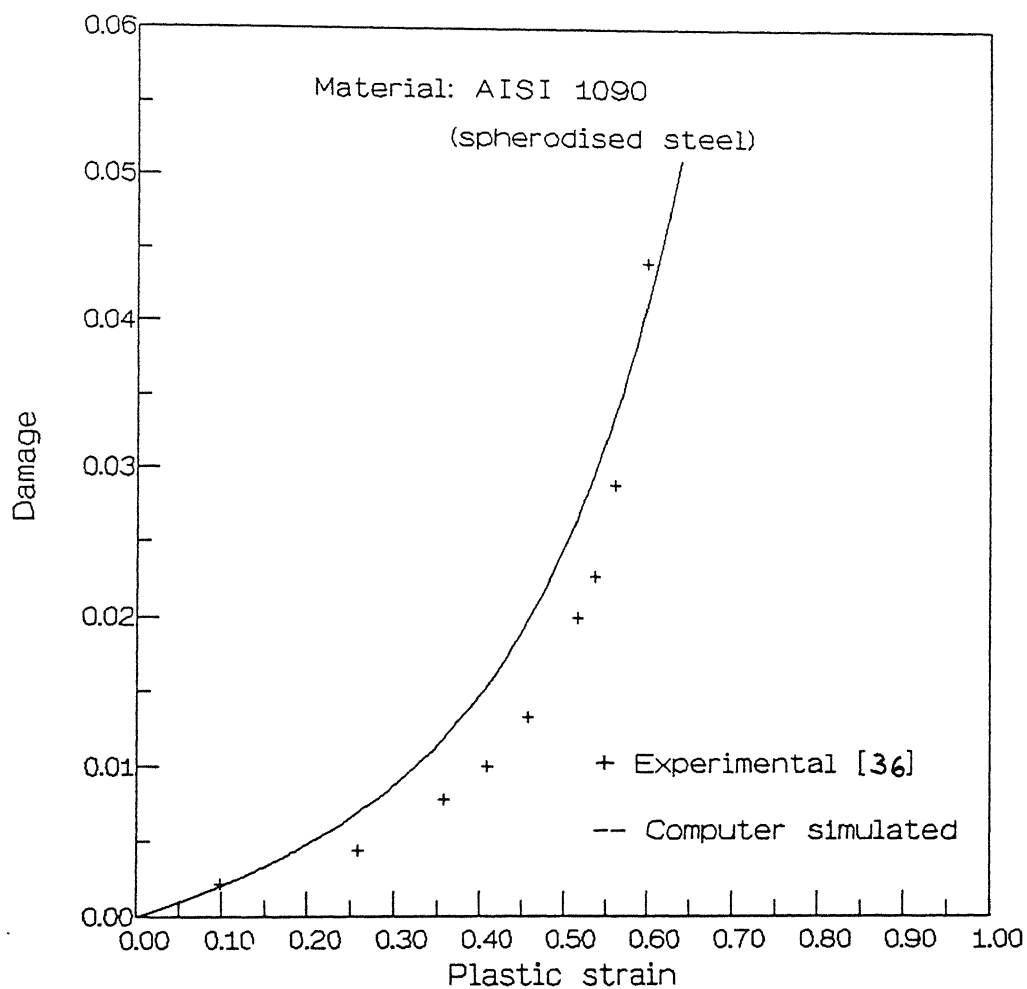
Fig 4.8. Comparison of computer simulated damage growth curve with experimental results for the cylindrical specimen.
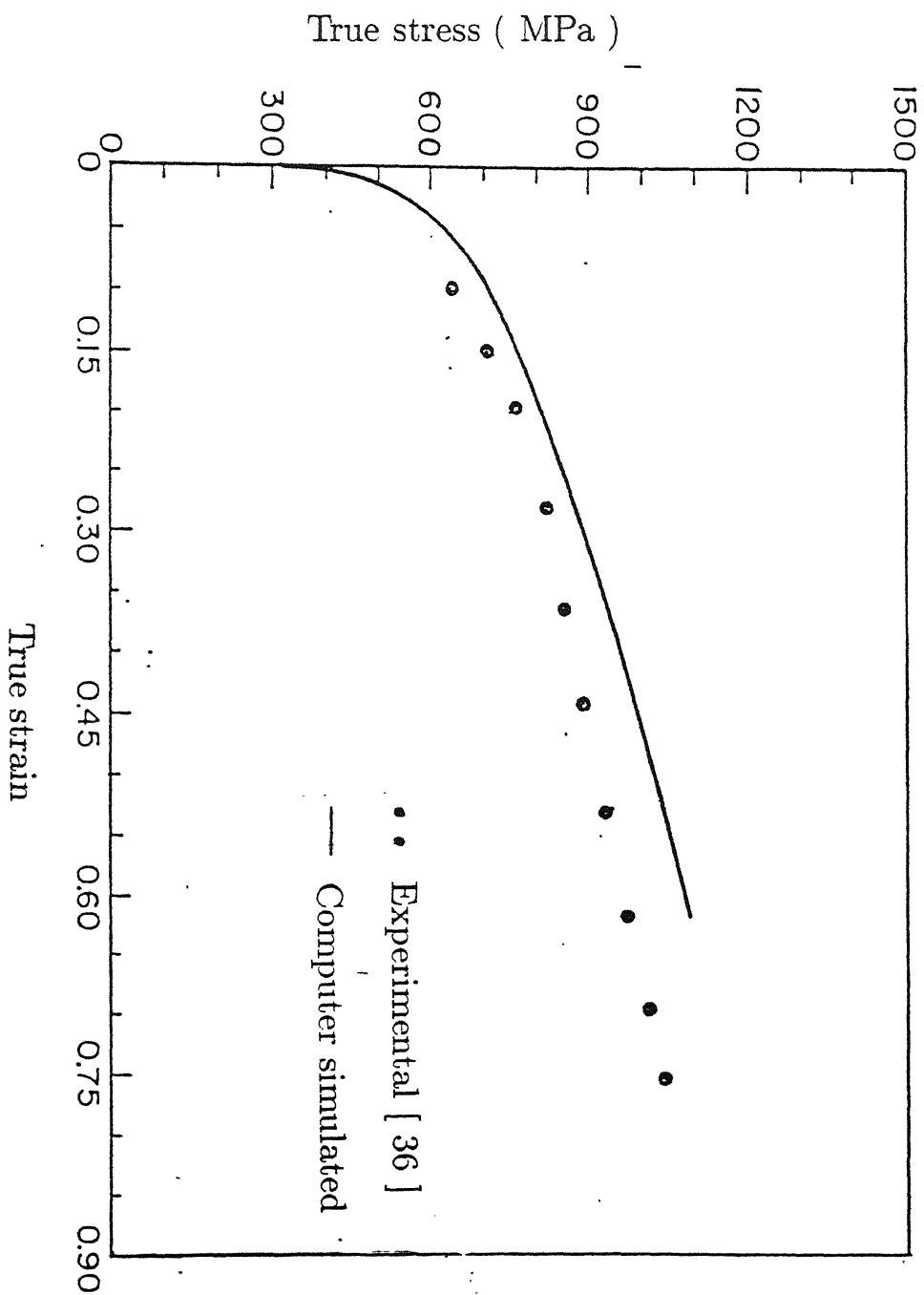
Fig 4.9. Comparison of computer simulated true stress-true strain curve with experimental results for the cylindrical specimen.
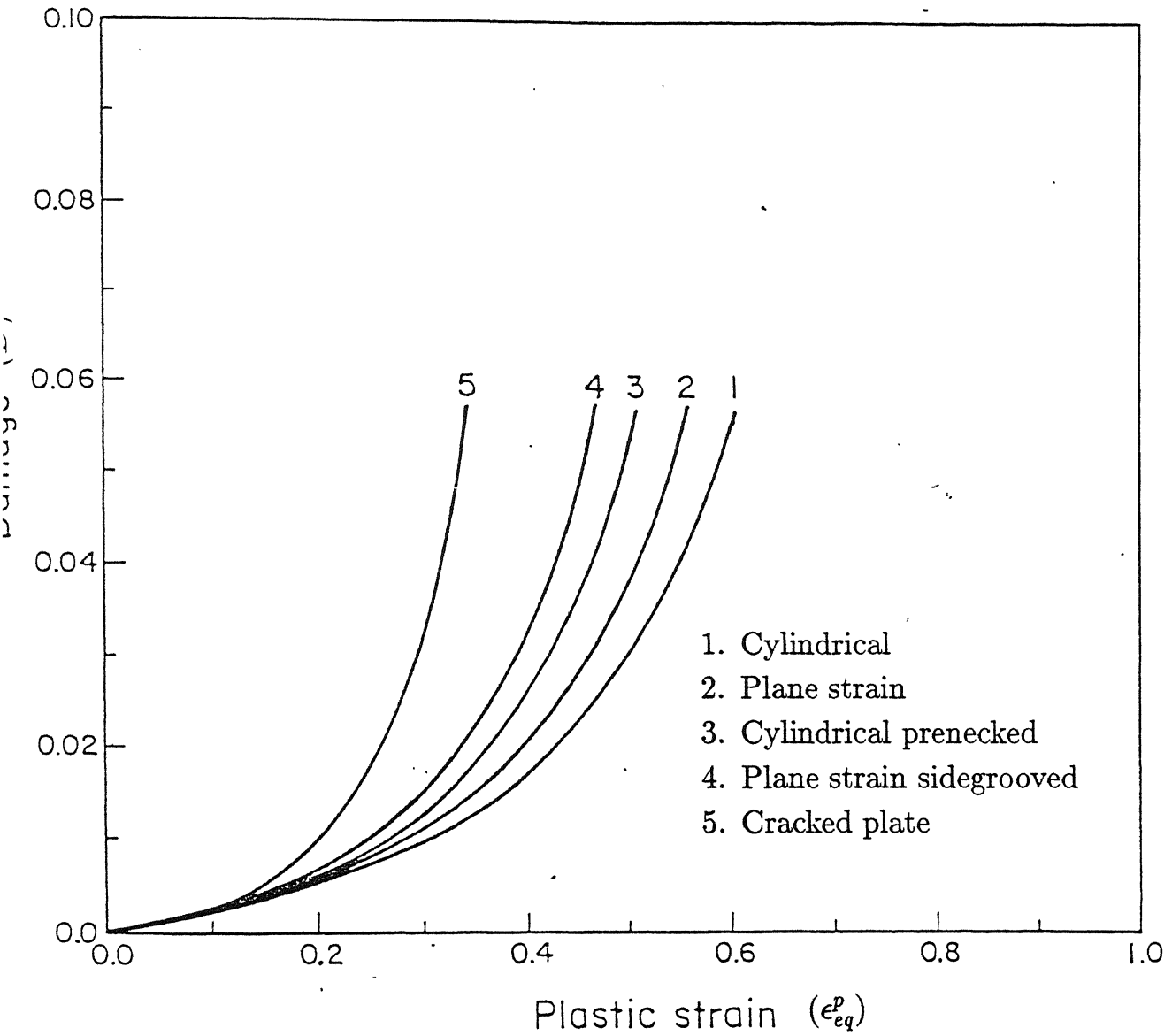
Fig 4.10. Damage growth curves for the five specimens.
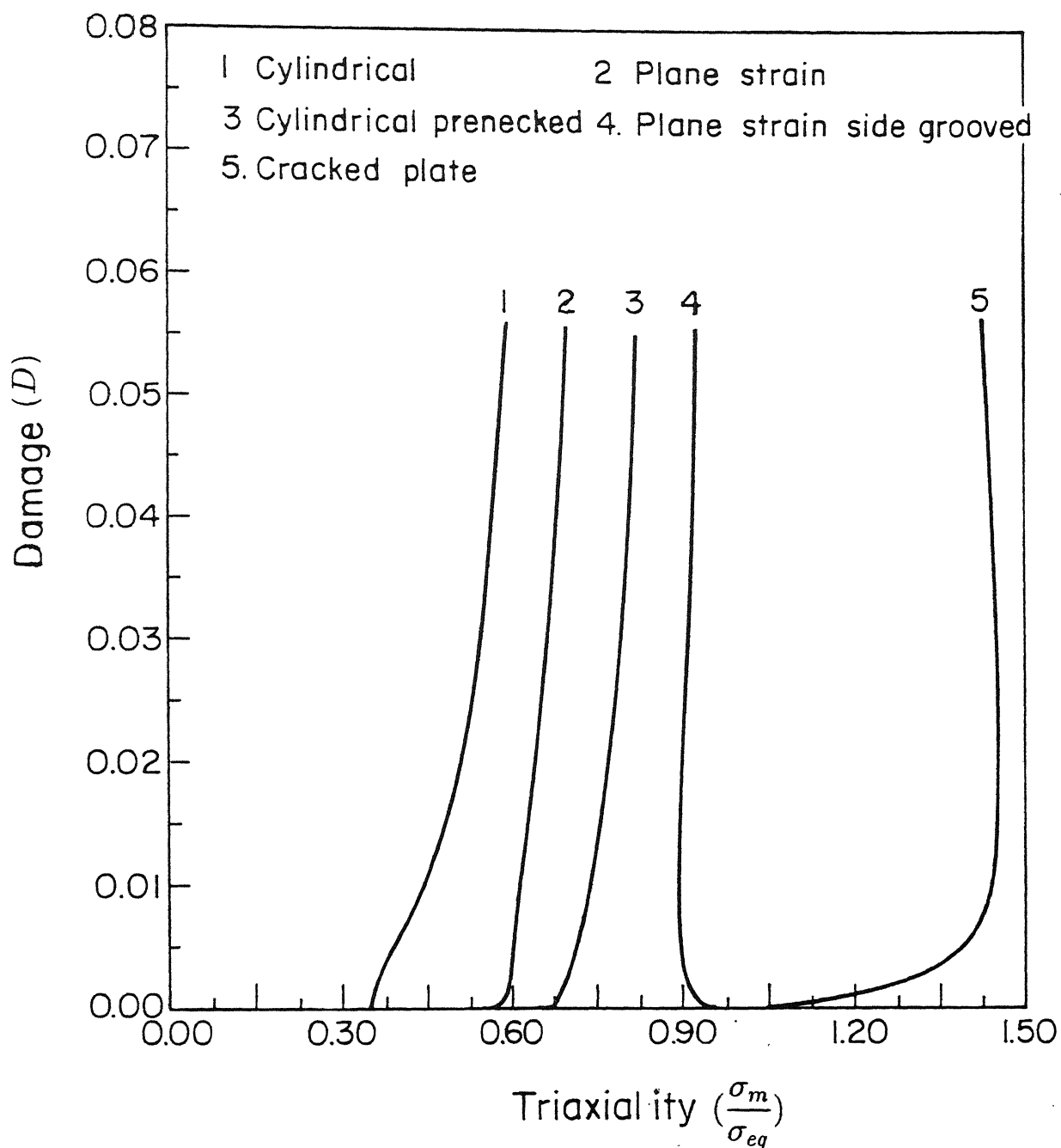
Fig.4.11   Damage versus triaxiality curves for the
            five specimens.

Sl No	Specimen	Critical strain	Critical triaxiality	Critical damage
1	cylindrical	0.61	0.593	5.62×10^{-02}
2	plane strain	0.55	0.701	5.68×10^{-02}
3	cylindrical prenecked	0.50	0.820	5.61×10^{-02}
4	plane strain side grooved	0.46	0.925	5.90×10^{-02}
5	cracked plate	0.34	1.430	5.80×10^{-02}

Table 4.4: Critical values of quantities for the five different cases
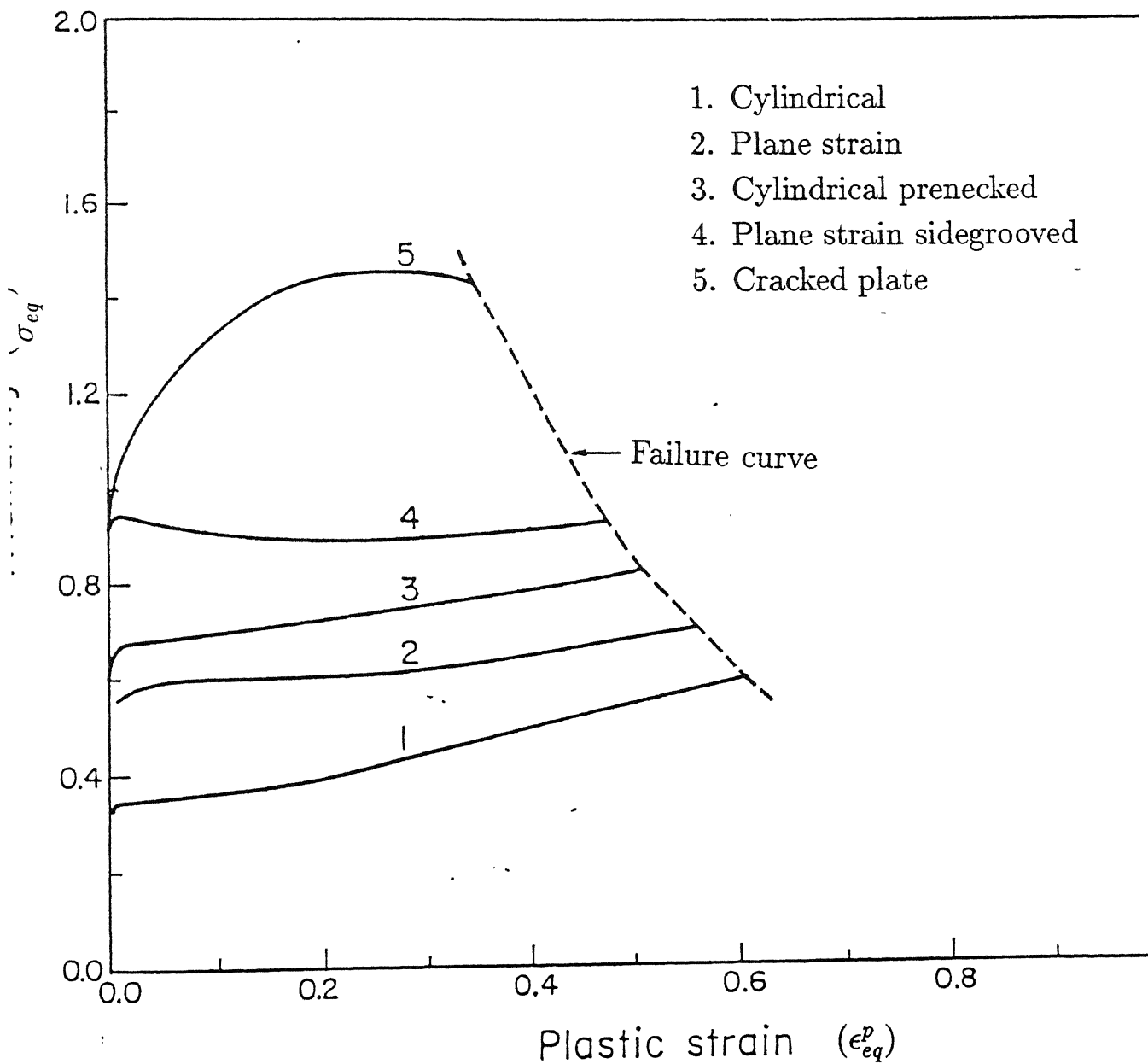
Fig 4.12. Failure curve.

Chapter 5

APPLICATION TO FRACTURE MECHANICS

5.1   Introduction

The previous Chapter was devoted to identify a continuum parameter namely damage variable (D) to indicate micro crack initiation in ductile material. It has been shown that the value of the damage variable reaches a critical value at the micro crack initiation. It has also been pointed out that, for different geometries, even though there is a wide variation in the values of critical strain and triaxial ity, the value of the critical damage remains almost the same.

In this chapter, a local criterion for crack growth initiation (the onset of growth of a existing crack) in Mode-I ductile fracture is proposed using the critical value of the damage variable (D_c). To test the validity of this criterion, experiments have been conducted on standard specimens and have also been simulated numerically. The proposed criterion has been used to find the critical values of load (P_{cr}), fracture toughness (J_{Ic}) and crack tip opening displacement ($(CTOD)_c$). The critical values of the fracture parameters, obtained from computer simulation, compare favourably with their experimental values.

83

5.2   Crack Growth Initiation Criterion

A local fracture criteria can be stated by two parameters namely a critical continuum parameter and a critical length parameter. The critical length parameter denotes the distance ahead of the crack tip where the continuum parameter has to reach its critical value for micro crack initiation. Thus, the critical length is a characteristic dimension of the material which fractures when the crack growth initiates. It is obvious that this characteristic dimension depends on the microstructure of the material and hence it is a material property.

In Chapter 1, some local crack growth initiation criteria have been discussed. In the RKR (Ritchie, Knott and Rice [42]) criterion, stress is used as the continuum parameter while the critical length parameter is taken to be twice the average diameter of Fe grain. On the other hand, in the criterion of Ritchie, Server and Wullaert [43], strain is used as the continuum parameter. The critical length parameter is coming out to be one to six times the average spacing of MnS particles. It is possible that in a few cases, the critical stress or critical strain may be able to predict micro crack initiation in ductile materials. However, as stated in Chapter 4, in general, micro crack initiation depends not just on the critical strain or critical triaxiality but on a critical combination of these two parameters. Since the damage incorporates both these parameters, in the present study, the critical damage (D_c) is used as the critical continuum parameter. For the material AISI-1090 spherodised steel, the value of D_c for different specimens lies between 0.056 to 0.059 (see Table 4.4). In further studies, this value is taken as 0.05. In the present study, the critical length parameter (l_c) is taken as the average austenite grain size of the material. The choice of austenite grain size is not unjustified because the larger sized particles restrict the austenite grain growth. Thus the proposed crack growth initiation criterion can be stated as follows. Whenever

$$D = D_c \quad \text{at } l = l_c \tag{5.1}$$

the crack growth initiates.

5.3 Experiments

The experiments were performed on AISI-1095 spherodised steel whose chemical composition is given in Table 5.1. The specimens tested for experimentation are Three Point Bend (TPB) specimens and Compact Tension (CT) specimens. The dimensions of the specimens were chosen according to the ASTM standard as far as possible. Figs (5.1(a)) and (5.1(b)) show the geometry and dimensions of the specimens.

The bulk material was austenised by heating it to 1000°C for two hours and then furnace cooled. Fig (5.2) shows the austenised grain structure of the material. The average grain size was measured by interception method. The average grain size was found as 33μm within a range of 30μm to 60μm. Next, the material was supplied for the preparation of specimens. After machining, the specimens were annealed by heating them to 750°C for two hours to relieve the residual stresses due to machining. The final heat treatment was done to spherodise the material by heating at 710°C for 20 hours. Fig (5.3) shows the spherodised structure of the material.

A tension test was performed to find the mechanical properties of the material. Table 5.2 shows the results of the test.

The specimens were precracked by fatigue loading in 100 KN MTS machine. The maximum load for a fatigue cycle was kept within 60% of the limit load which was calculated from the following formulae [55].

$$P_L = \frac{4\ B\ b^2\ \sigma_o}{3\ S}, \qquad \text{for TPB specimen} \qquad (5.2)$$

and,

$$P_L = \frac{B\ b^2\ \sigma_o}{2\ (W + a)}, \qquad \text{for CT specimen.} \qquad (5.3)$$

Here, S is the half-length of the TPB specimen, B is the width of the specimen, b is the ligament length, a is the effective crack length and $W = a + b$ (see Fig 5.1). After the appearance of a crack, the maximum load was reduced to 40% of the limit load gradually.

Following are the fatigue data for a TPB and a CT specimen.

For a TPB specimen,

Initial maximum load = 8 KN,

Fatigue ratio = 0.1,

Frequency = 10 Hz,

Final maximum load = 5 KN.

A total of 1,10,000 cycles were required to have a fatigue crack growth of 3.5 mm (which was measured after breaking the specimen at the end of the experiment).

For a CT specimen,

Initial maximum load = 6 KN,

Fatigue ratio = 0.1,

Frequency = 10 Hz,

Final maximum load = 4 KN.

A total of 66,000 cycles were required to have a fatigue crack of size 2.3 mm .

After precracking, the specimens were steadily loaded by controlling the displacement of the ram. In all the cases, a ram speed of 0.1 mm/min was maintained. The load and the load point displacement were recorded in X-Y plotter throughout the loading history. The crack growth initiation was indicated by a distinct pop-in in all the cases. The measured values of the load and the load point displacement and the calculated value of J_I at this point are termed as their critical values and are denoted respectively by P_{cr}, U_{cr} and J_{Ic} . For calculating J_I value at a certain load level, the following formulae were used [56].

For TPB specimen,

$$J_I = \frac{2A}{B\,b} \tag{5.4}$$

where A is the area under the load versus load point deflection curve. For CT specimen,

$$J_I = \frac{\eta A}{B\,b} \tag{5.5}$$

where Ernest factor η is given by [56]

$$\eta = 2.0 + 0.522 \frac{b}{W}.$$

Figs (5.4(a), (b), (c)) and (5.5(a), (b)) show the experimental load deflection curves for the TPB and the CT specimen respectively. The fractured surfaces of broken specimens were scanned by 15 KV JEOL JSM 840 A scanning electron microscope. Figs (5.6(b), (c), (d), (e)) show the fractography taken at different places. The locations of scanning were chosen in accordance with Fig 5.6(a).

5.4 Numerical Simulation Of Fracture Tests

The updated Lagrangian finite element formulation of a damaged elastic-plastic material, developed in Chapter 3, is used to numerically simulate the fracture mechanics tests conducted in this study. The damage growth law, used in computing the damage variable 'D' at any deformation level, is the same as given by equation (2.60). Since the chemical composition and the mechanical properties of the test material are close to that of AISI-1090 spherodised steel (see Tables 4.2, 4.3, 5.1, and 5.2), the values of the coefficients a_1, a_2 and c of the damage growth law are taken to be the same as that of AISI-1090 spherodised steel. These values are given by equation (4.1). Also, the critical value of the damage variable is taken same as that of AISI -1090 spherodised steel i.e $D_c = 0.05$. The average austenite grain size of the test material, as mentioned in the previous section, is $33\mu m$. For crack growth initiation, the criterion proposed in section 5.2 is used. According to this criterion, whenever the value of the damage variable reaches D_c at a distance l_c (austenite grain size) ahead of the crack tip, the crack growth initiates (equation 5.1). Size of the crack tip element is chosen so as to facilitate the application of this criterion. Fig (5.7) shows a representative crack tip element of size $2l_c \times 2l_c$ such that the Gauss point nearest to the crack tip represents one grain. Figs (5.8(a), (b)) show the finite element mesh for both TPB and CT specimens. Eight noded isoparametric elements are used everywhere except at the crack tip where the collapsed crack tip elements are used. A 2×2 Gauss integration scheme is used throughout.

The specimens are deformed by giving a prescribed incremental displacement at a

fixed point which is the load point in actual experiment. Load is calculated from nodal reactions. At the end of each increment, the increment in damage is calculated by using the damage growth law (equation 2.60) which is added to its previous value to get the total damage. During elastic unloading the damage calculation is bypassed. At the end of each increment, the damage at the Gauss point nearest to the crack tip is compared with its critical value. As soon as 'D' reaches 'D_c' the programme is terminated. All values at this stage are termed as the critical values of the respective quantities. The 'J_I' value is calculated after computing the area under the load deflection curve using the relations (5.4 - 5.5). The stretch zone width is calculated from the stretching of the initial crack i.e

$$SZW = (a_i - a_o) \tag{5.6}$$

where, a_i is the current crack length and a_o is the initial crack length. The value of the stretch zone width at the critical condition is regarded as critical stretch zone width or $(SZW)_c$. Out of all collapsed nodes, the Ist node is vertically restrained and others are allowed to move during deformation (Fig(5.9)). CTOD is regarded as the vertical opening of the last collapsed node (node 9). Its value at the critical condition is regarded as the critical crack tip opening displacement or $(CTOD)_c$.

Out of all test specimens, TPB1 and CT1 were completely simulated using the procedure cited above. The plane strain condition was assumed in both the cases.

5.5   Results and Discussion

Experimental Results

Experimental load deflection curves are shown in Figs (5.4(a),(b),(c)) for TPB specimens. It is observed that all the curves show a distinct pop-in which is taken as the crack growth initiation point. This is followed by a ductile crack growth. At the crack growth initiation, there is profuse void growth and coalescence in the highly localised plastic zone at the crack tip and this causes the initial instability. This tendency reduces

and finally arrested due to fall in triaxiality as the free surface is approached.

Figs (5.5(a),(b)) show the load deflection curves for CT specimens. The trends are similar to that of TPB specimens.

Table 5.3 shows the experimental results of TPB specimens. It is found that, for a/w ranging from 0.526 to 0.595, J_{Ic} value varies from $65.77 KN/m$ to $70.99 KN/m$. The average experimental value of J_{Ic} is $68.08 KN/m$. The Table shows a decrease in critical load with the increase of a/w ratio. This is due to decrease in the ligament length b. Table 5.4 shows the experimental results of CT specimens. The average value of J_{Ic} is found as $65.68 KN/m$.

The fractographs (Fig 5.6(b), (c)) reveal the critical stretch zone. The critical stretch zone width for TPB1 specimen is found to be $35\mu m$ and that of CT1 specimen to be $50\mu m$. The other fractographs (Figs 5.6(d), (e)) show voids in the voided zone and ductile shear lips near the free surface.

Comparison between Experimental and Numerical Results

Fig (5.10) shows a comparison of the computer simulated load versus load point deflection curve with that of the experimental curve for the TPB1 specimen. The computer simulated curve depicts similar trend as that of the experimental curve. The difference in critical load prediction is 11.0%. Fig (5.11) is a comparison of load versus load point deflection curve with that of the experimental one for CT1 specimen. The difference in critical load values is 5.0%. Both the computer simulated curves have higher critical loads than those of experimental curves because the simulated curves are for the plane strain condition.

The computer simulated J_{Ic} value of TPB1 specimen is $72.44 KN/m$. On the other hand, the average experimental value of J_{Ic} for TPB specimens is 68.08 KN/m (Table 5.3). The simulated value is 6.3% higher than the experimental value. The computer simulated value of J_{Ic} for CT1 specimen is $73.78 KN/m$ which is 11.0% higher than that

of the average experimental value ($65.68 KN/m$) for CT specimens (Table 5.4). Both the simulated cases yield higher values of J_{Ic} than those from experiments. Since the computer simulations are for plane strain condition, the simulated values are expected to be less than those of experiments. The discrepancy may be due to the reason that the critical value of damage variable (D_c) of the material is determined by using Thomason's limit load analysis (Chapter 2) which uses the upper bound theorem. Thus, the value of D_c equal to 0.05 is an over estimation of the actual value.

The values of critical stretch zone width, calculated for TPB1 and CT1 specimens from equation (5.6), are $31.26 \mu m$ and $32.09 \mu m$ respectively. These computer simulated values are almost equal to the average austenite grain size ($33 \mu m$) of the material. The experimental values of critical stretch zone width ($35 \mu m$ for TPB1 specimen and $50 \mu m$ for CT1 specimen) are within the range of measured grain size ($30 \mu m - 60 \mu m$). The results show that the critical stretch zone width is of the order of grain size l_c.

Comparisons of computer simulated results with experimental data show that the overall agreement is satisfactory. Since the computer simulation uses the proposed crack growth initiation criterion (equation 5.1) for calculating the critical values of the quantities, it shows that the proposed criterion is reasonably good in explaining Mode I fracture for the class of materials discussed here.

Additional Numerical Results

Some additional quantities are computed from the plane strain analysis of a Full CT specimen (Fig (5.12)) . Fig (5.13) shows the growth of plastic zone at different deformation levels. The critical plastic zone size is found to be 0.176 mm. The critical damage zone is shown in Fig (5.14). The ratio of the critical plastic zone to critical damage zone is found as 5.6. This shows that the damage is a highly localised event at the crack tip. Figs (5.15 and 5.16) show the variation of triaxiality and σ_{yy} along the crack line. It is observed that both the values drop at the crack tip. This is expected due to crack tip blunting.

A graph of J_I versus CTOD is shown in Fig (5.17). The relation is linear upto crac growth initiation point. The value of critical crack tip opening displacement ($CTOD_c$ is $56\mu m$ which is 1.8 times the calculated value of critical stretch zone width. Slope c the curve is found as $2.4\sigma_o$. The theoretical value of the slope is $1.6\sigma_o$ (in plane strai. condition) for a ideally plastic material in small scale yielding. In large scale yielding this value can go upto $2.6\sigma_o$ depending on hardening exponent (n) [57]. Thus, the valu of the slope is in confirmity with the exiting result.

C	Mn	S	P	Si	Fe
0.92	0.80	0.035	0.013	-	-

Table 5.1: Chemical composition (% wt) of the test material

Young's Modulus E GPa	Poisson's Ratio ν	Yield Stress σ_o MPa	Ultimate Stress σ_{uts} MPa	Ultimate Strain ϵ_{ut}	Fracture Strain ϵ_f	Hardness Rc	K MPa	n
210	0.3	497	690	15%	59%	34	1211	0.22

Table 5.2: Mechanical properties of the test material
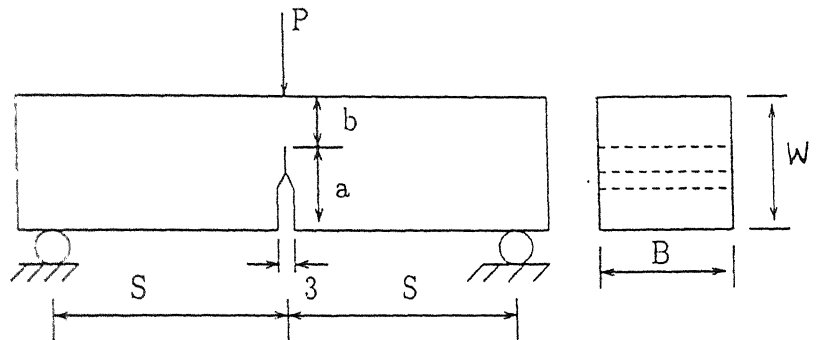
Three point bend (TPB) specimen   All dimensions are in mm

Material	Specimen No	a mm	b mm	W mm	B mm	S mm
AISI 1095 Spherodised Steel	TPB1	11.9	8.1	20	20	40
	TPB2	10.0	9.0	19	19	40
	TPB3	10.1	8.9	19	19	40

Fig. 5.1 (a) : Geometry of TPB Specimens.

2 holes of $\phi = 6.5$
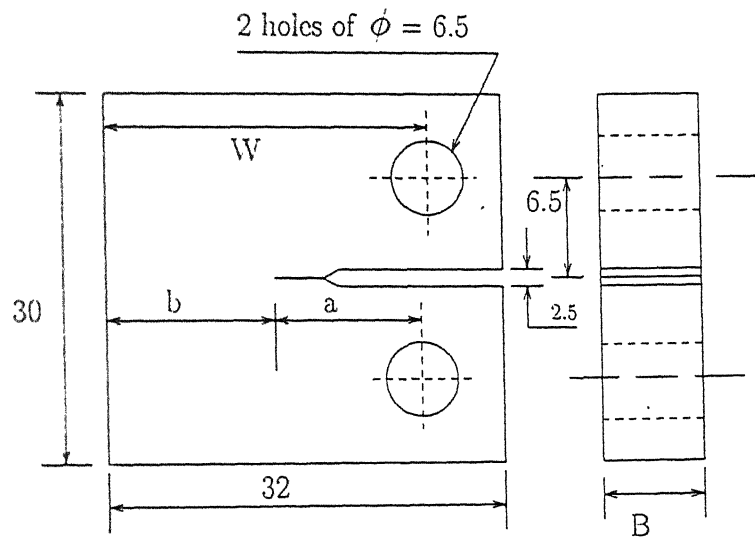
Compact Tension (CT) Specimen   All dimensions are in mm

Material	Specimen No	a mm	b mm	W mm	B mm
AISI 1095 Spherodised Steel	CT1	14.5	10.5	25	8
	CT2	15.0	10.0	25	8

Fig 5.1 (b) : Geometry of CT Specimens.

$1cm = 36\mu m$
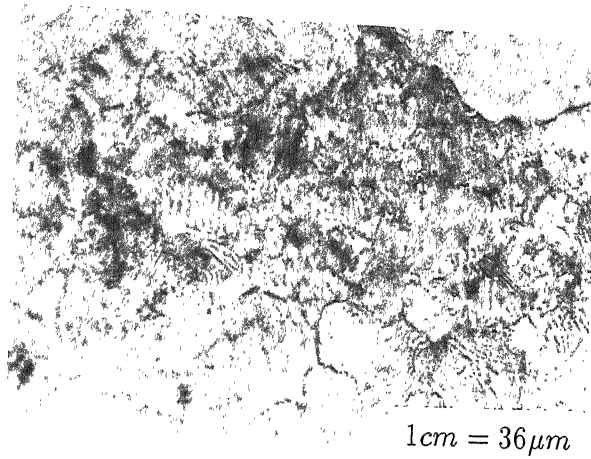
Fig 5.2. Austenite grain structure of material AISI-1095 (C% 0.92).

$1cm = 50\mu m$
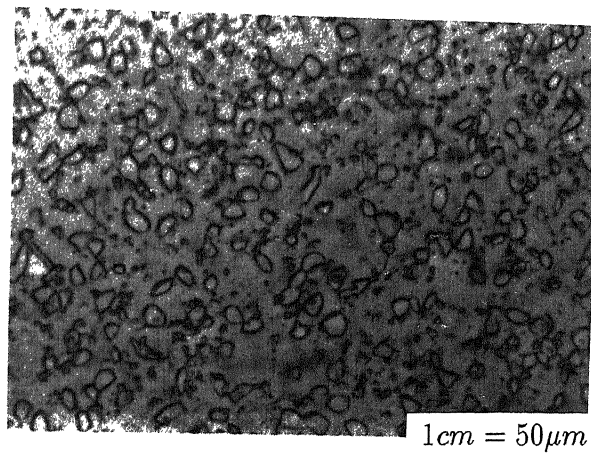
Fig 5.3. Spherodised structure of material AISI-1095 steel (C% 0.92).
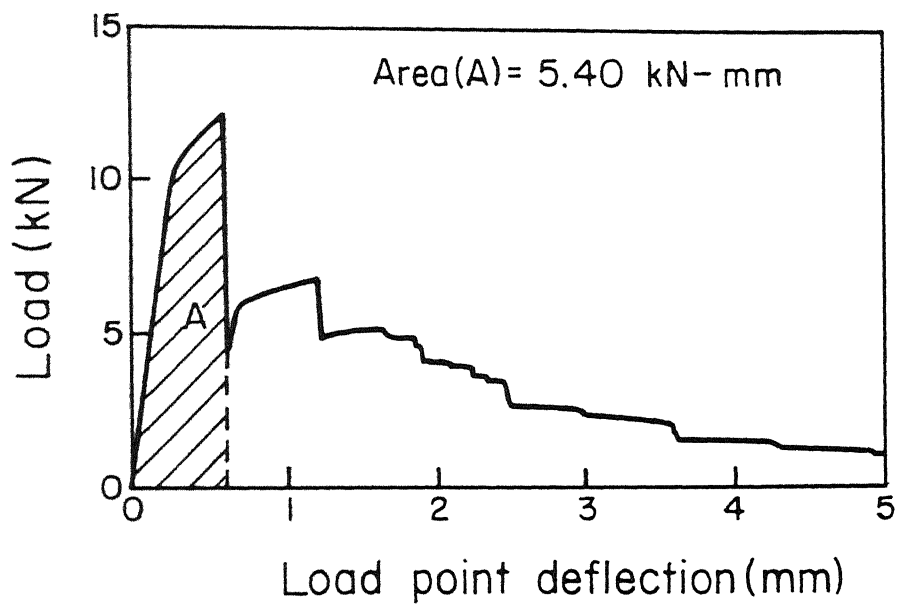
Fig. 5.4 (a) Experimental load deflection curve of specimen TPBI.
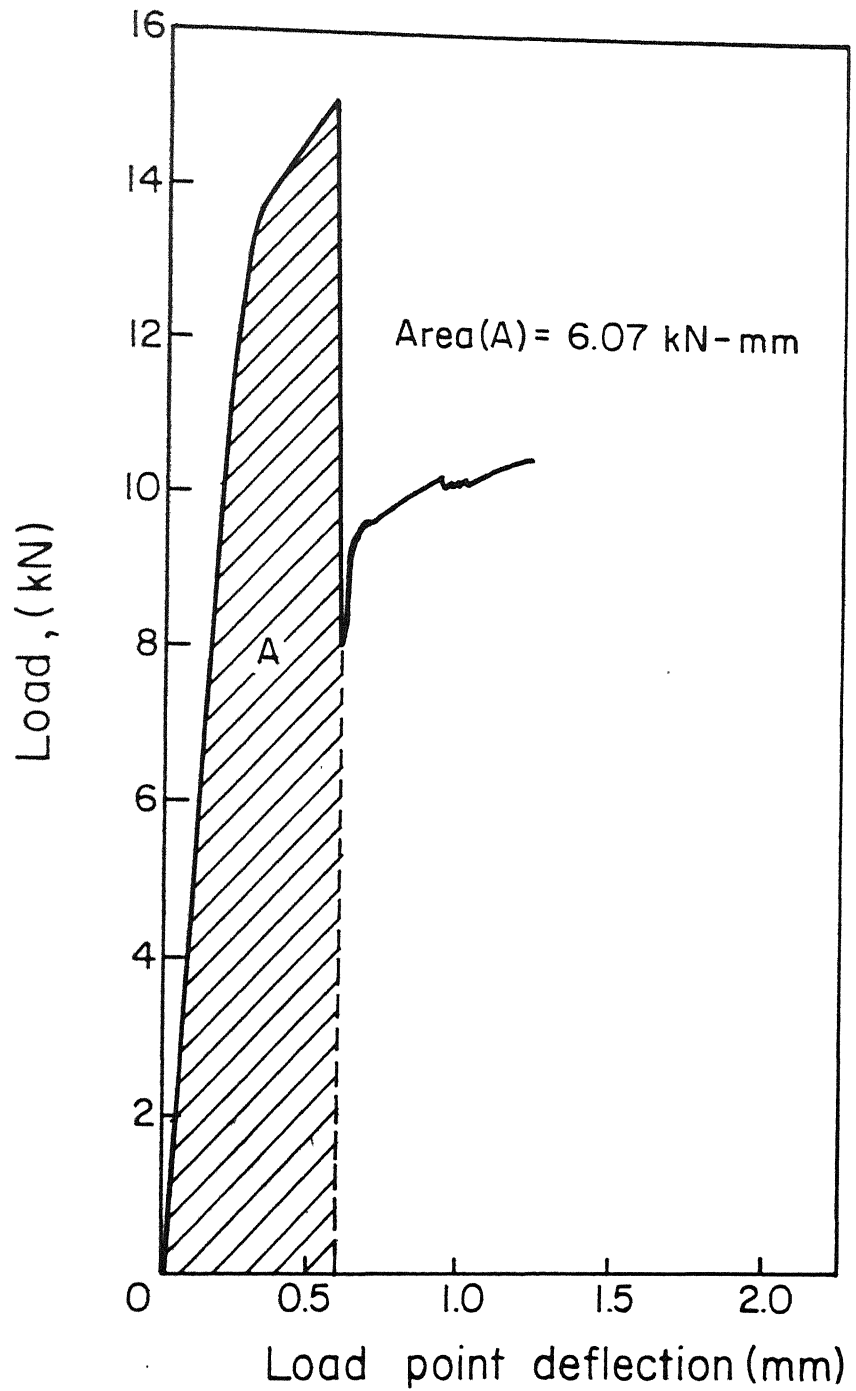
Fig. 5.4 (b) Experimental load deflection curve of spec
TPB - 2.
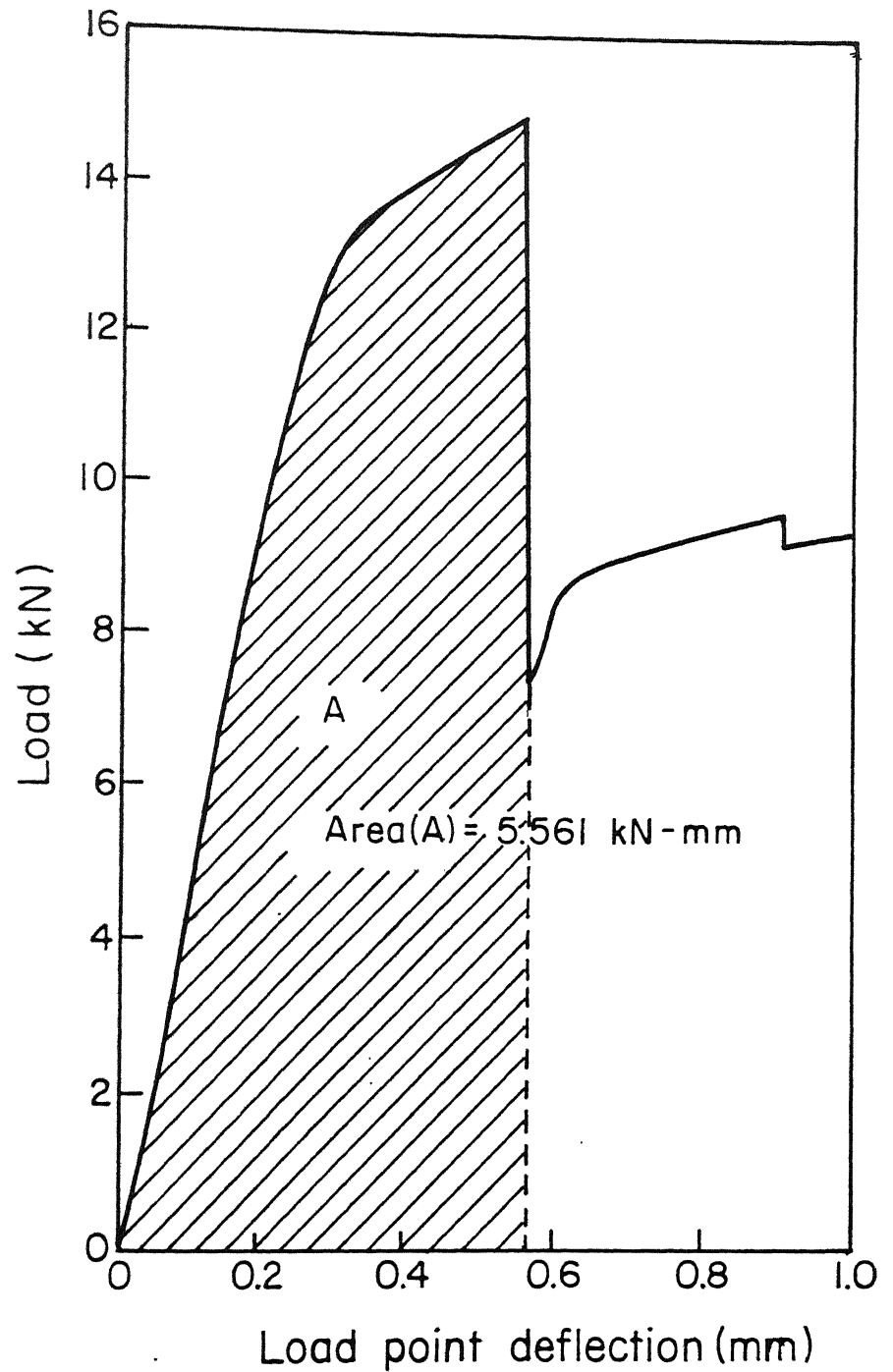
Fig.5.4(c) Experimental load deflection curve of sp
TPB-3 .
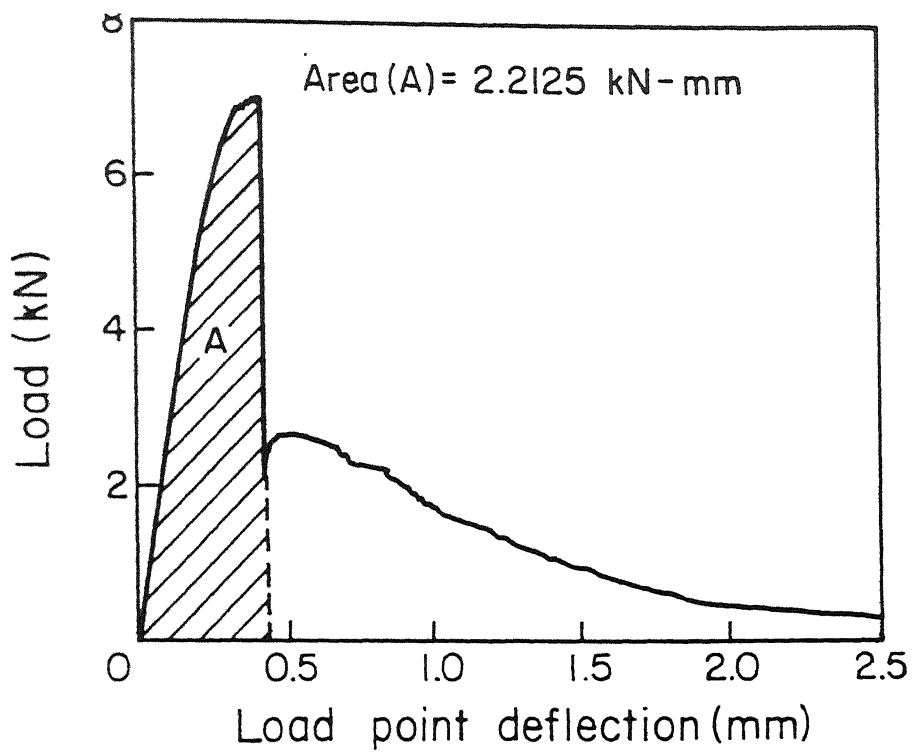
Fig.5.5(a) Experimental load deflection curve of specimen CT-I
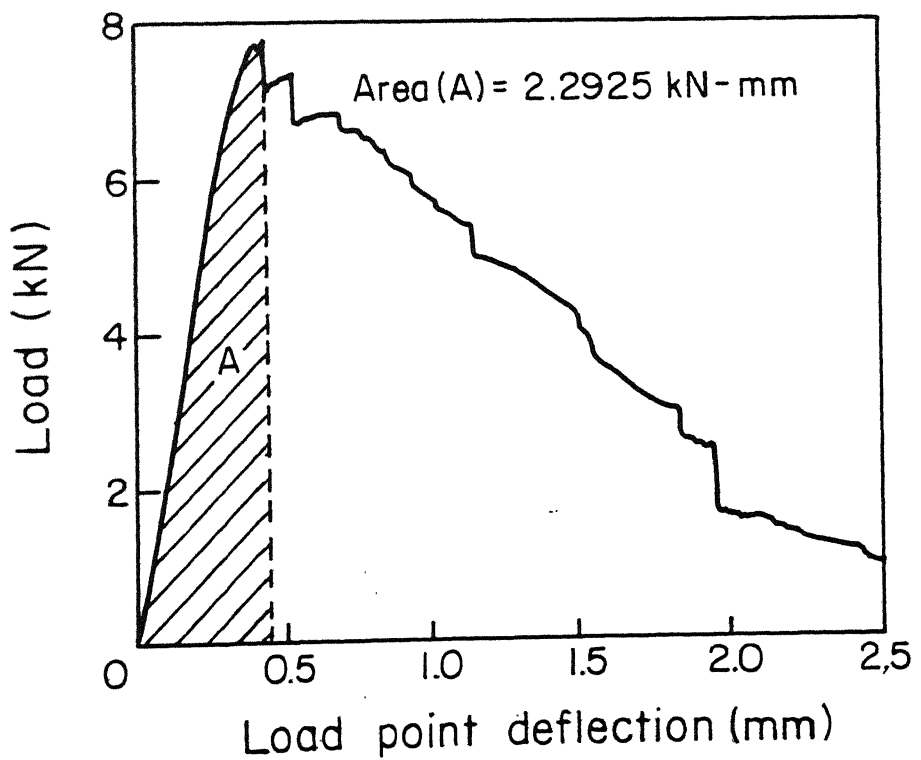
Fig.5.5(b) Experimental load deflection curve of

Specimen	$\frac{a}{w}$	P_{cr} KN	U_{cr} mm	J_{Ic} KN/m	Average J_{Ic} KN/m
TPB1	0.595	12.0	0.65	67.50	
TPB2	0.526	15.1	0.60	70.99	68.08
TPB3	0.531	15.0	0.59	65.77	

Table 5.3: Experimental results of TPB specimens

Specimen	$\frac{a}{w}$	P_{cr} KN	U_{cr} mm	J_{Ic} KN/m	average J_{Ic} KN/m
CT1	0.58	6.98	0.45	64.52	
					65.68
CT2	0.60	7.70	0.425	66.85	

Table 5.4: Experimental results of CT specimens

Fatigue crack

Notch surface

voided zone

ductile shear lips

S Z
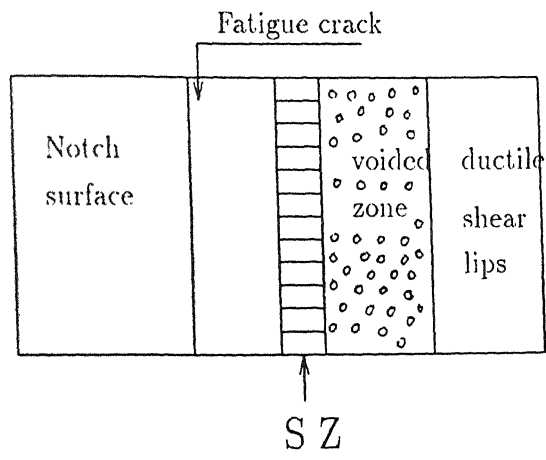
(a) Location of different zones.

tpb1/int
0490   15KV   X350 100µm WD20

(b) Stretch zone of TPB1 specimen.

CT1
0870   15KV   X250 100µm WD39
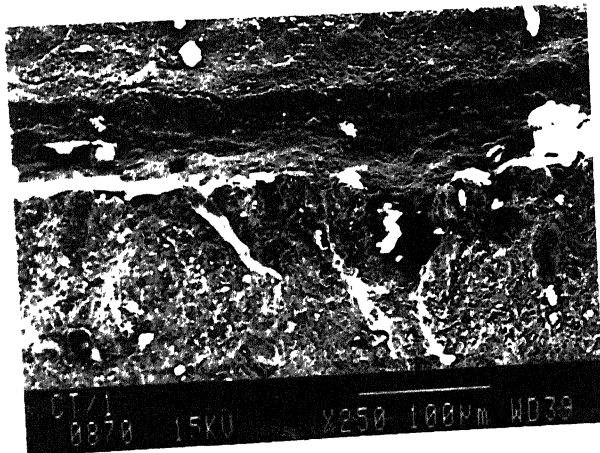
(c) Stretch zone of CT1 specimen.

Fig. 5.6 Fractographs of fractured surface.
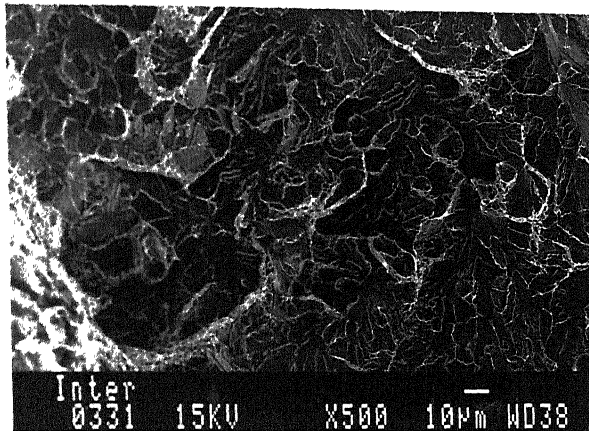
(d) Voided zone.
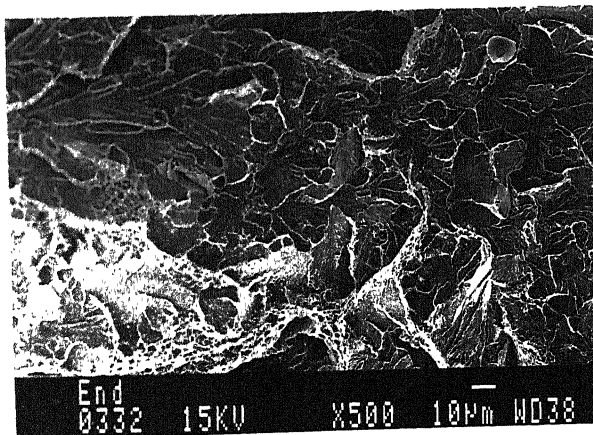
(e) Ductile shear lips.

Fig. 5.6 Fractographs of fractured surface.

Fig.5.7   A representative crack tip element.

Enlarged view of crack tip at A.

$\frac{P}{2}$
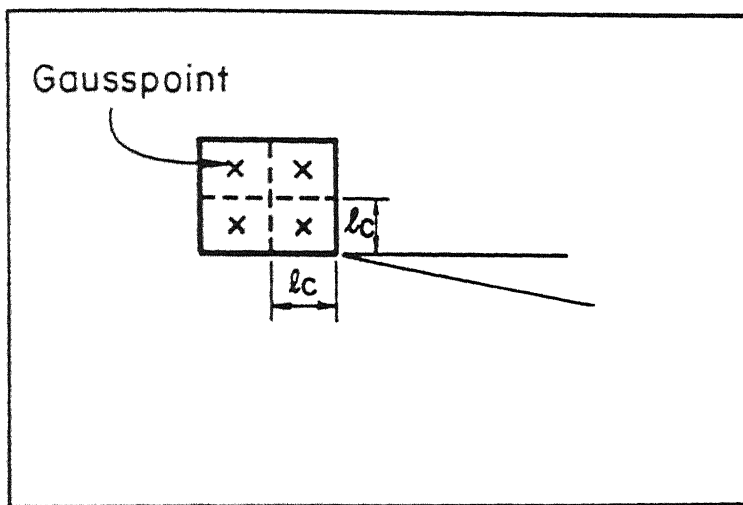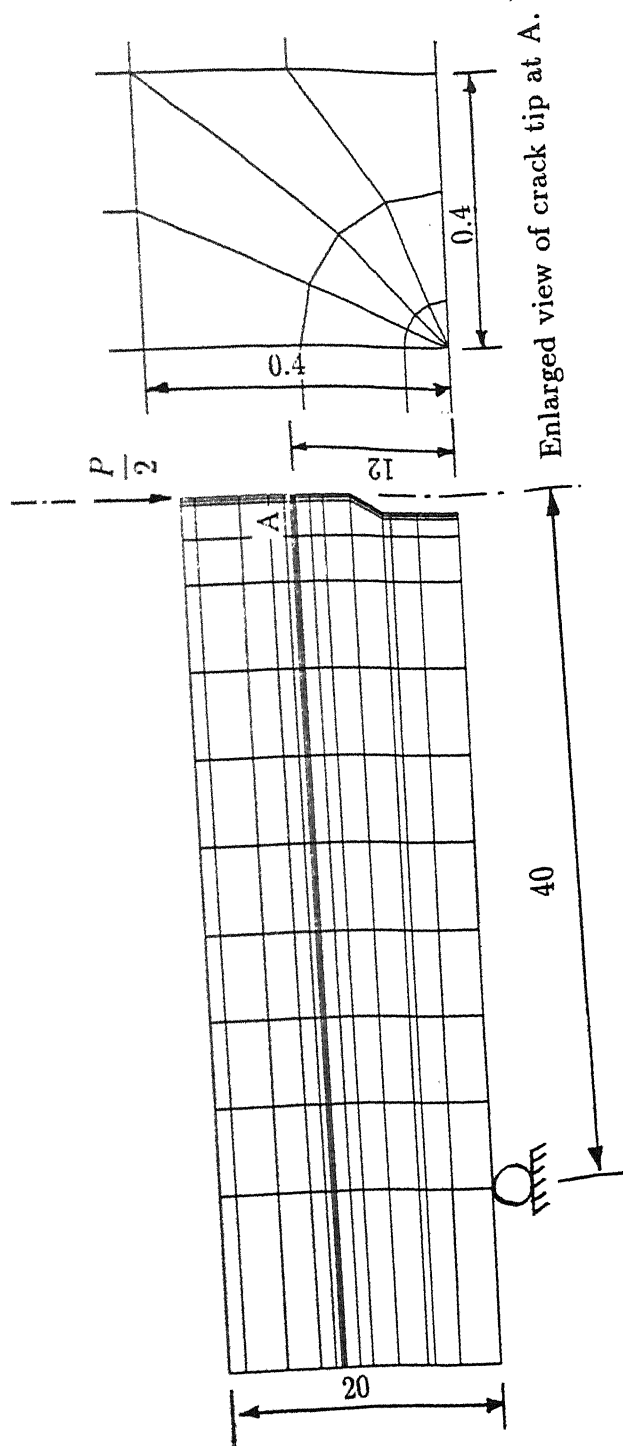
All dimensions are in mm.

Fig 5.8(a). Finite element mesh of specimen TPB1.

Enlarged view of crack tip at A.
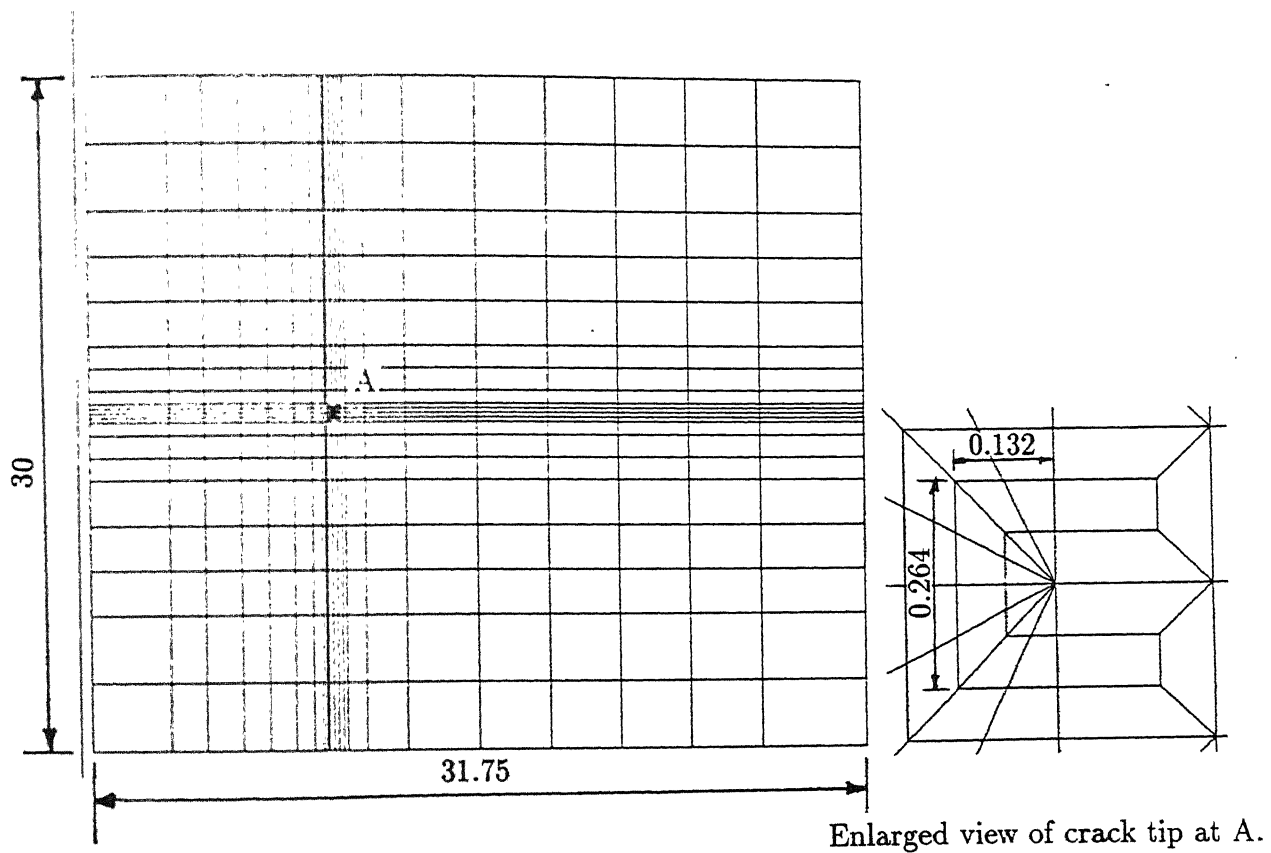
All dimensions are in mm.

Fig 5.8(b). Finite element mesh of specimen CT1.
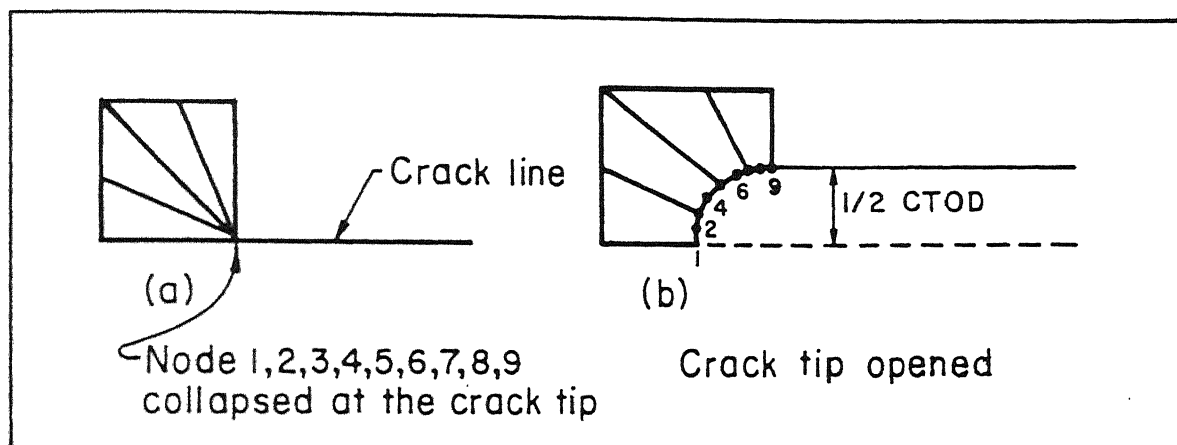
Fig.5.9 Modelling of crack tip.
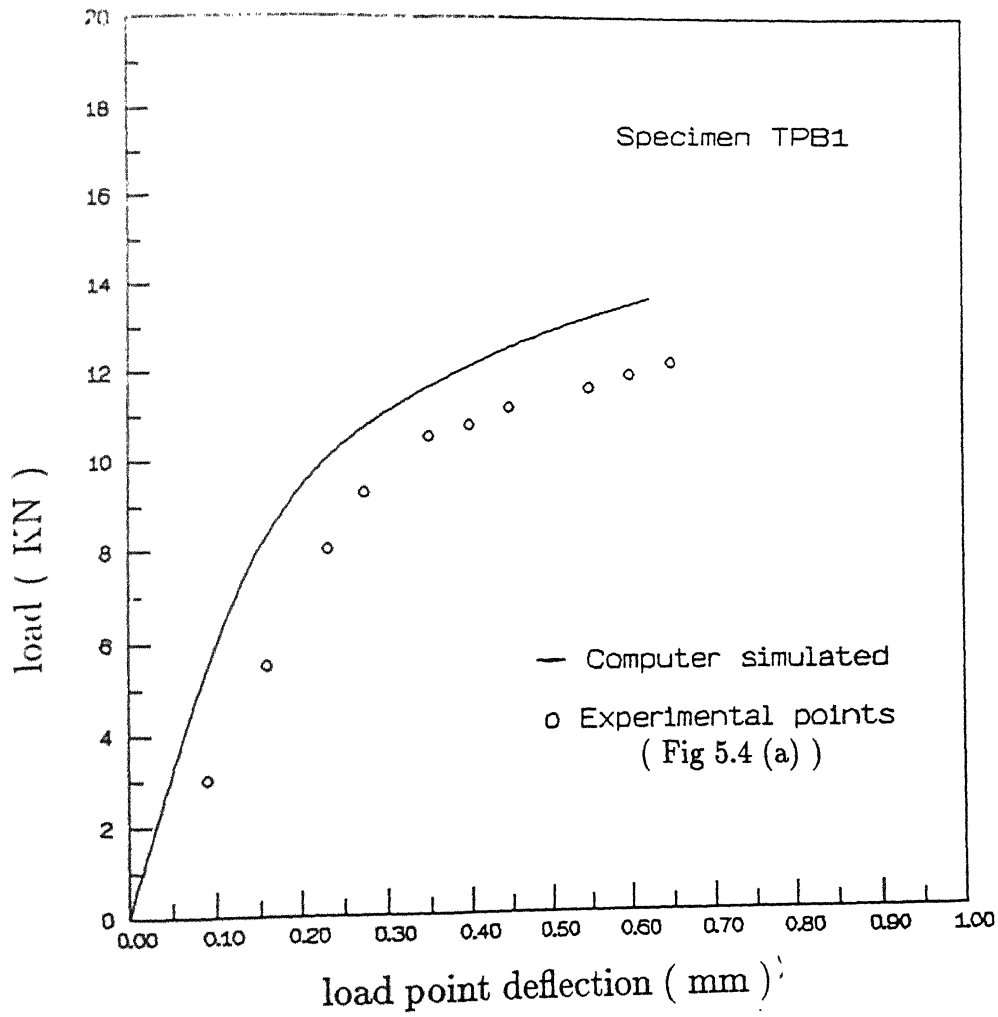
Fig 5.10. Load versus load point deflection curve for TPB1 specimen.
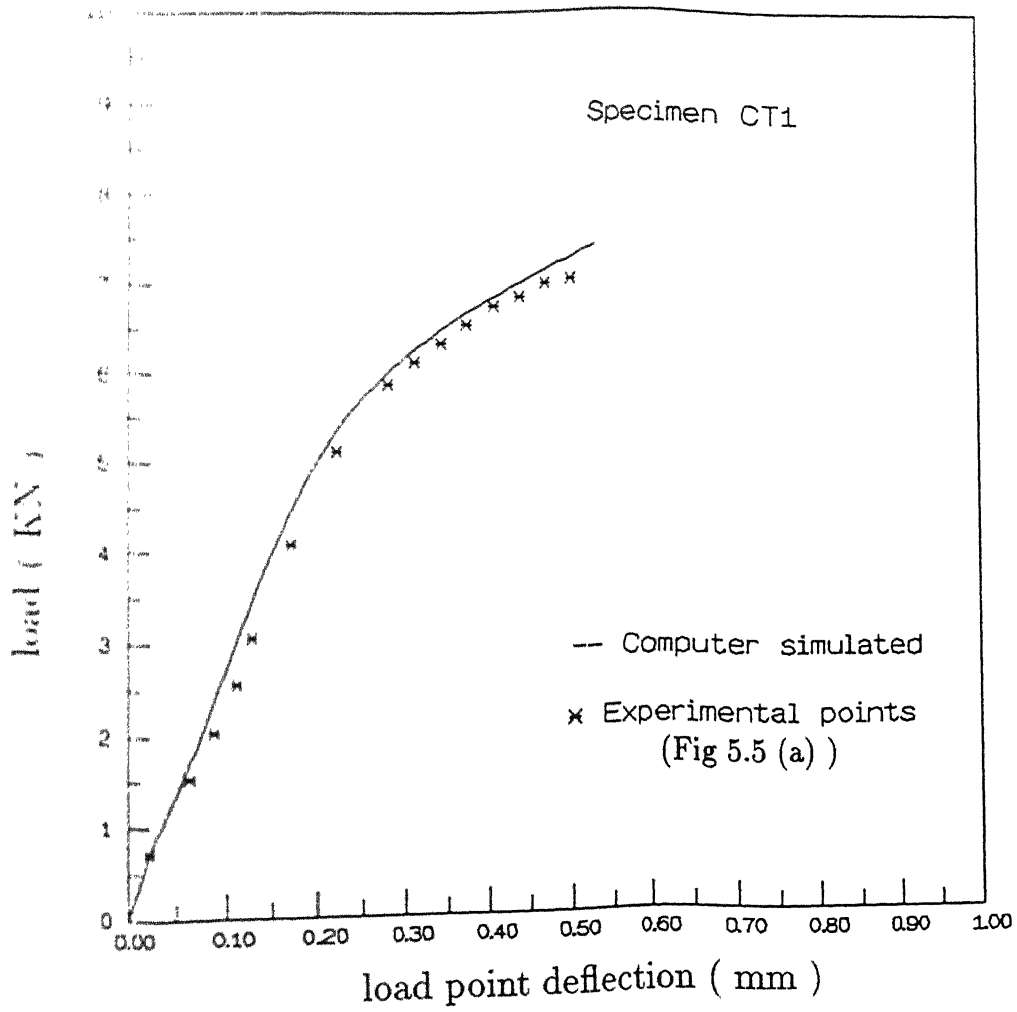
Fig 5.11. Load versus load point deflection curve for CT1 specimen.
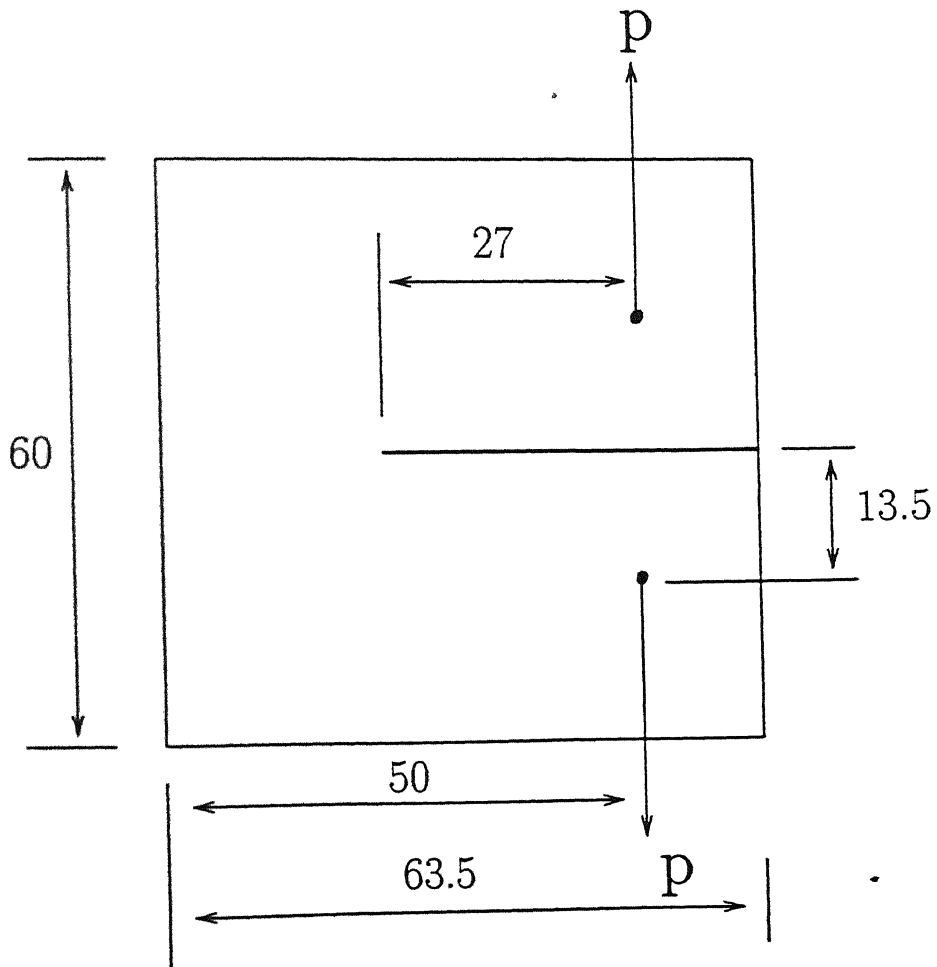
All dimensions are in mm

Fig 5.12. Geometry of Full CT specimen.
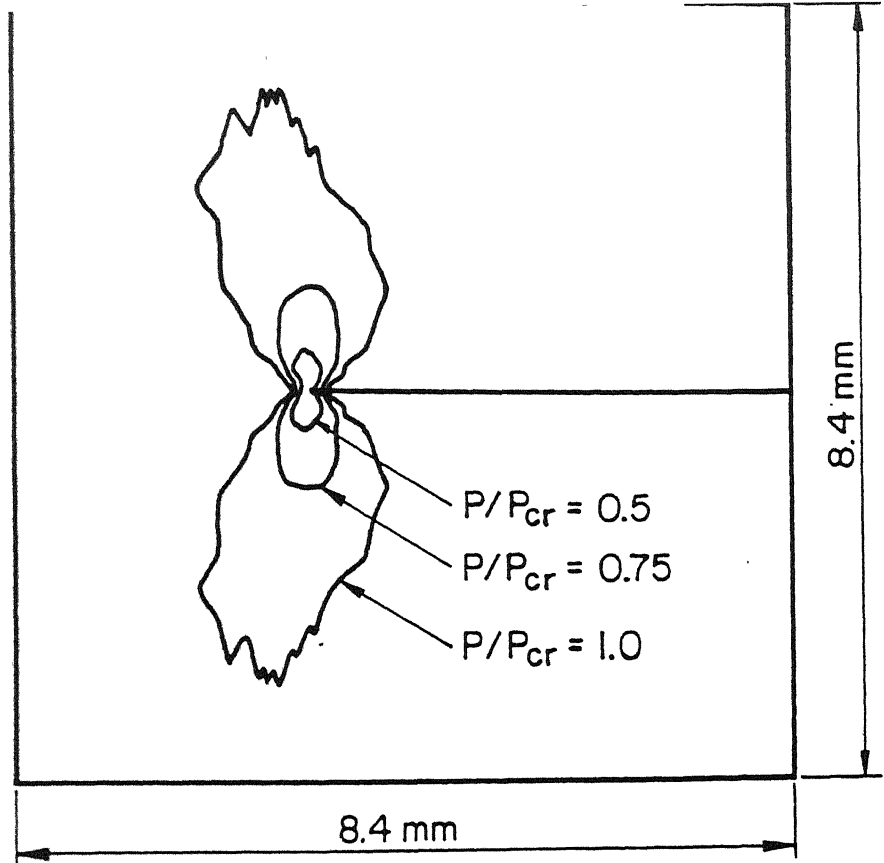
Fig.5.13   Growth of plastic zone.
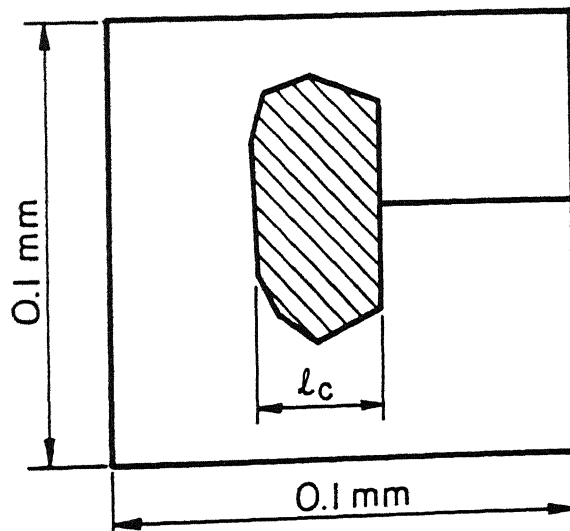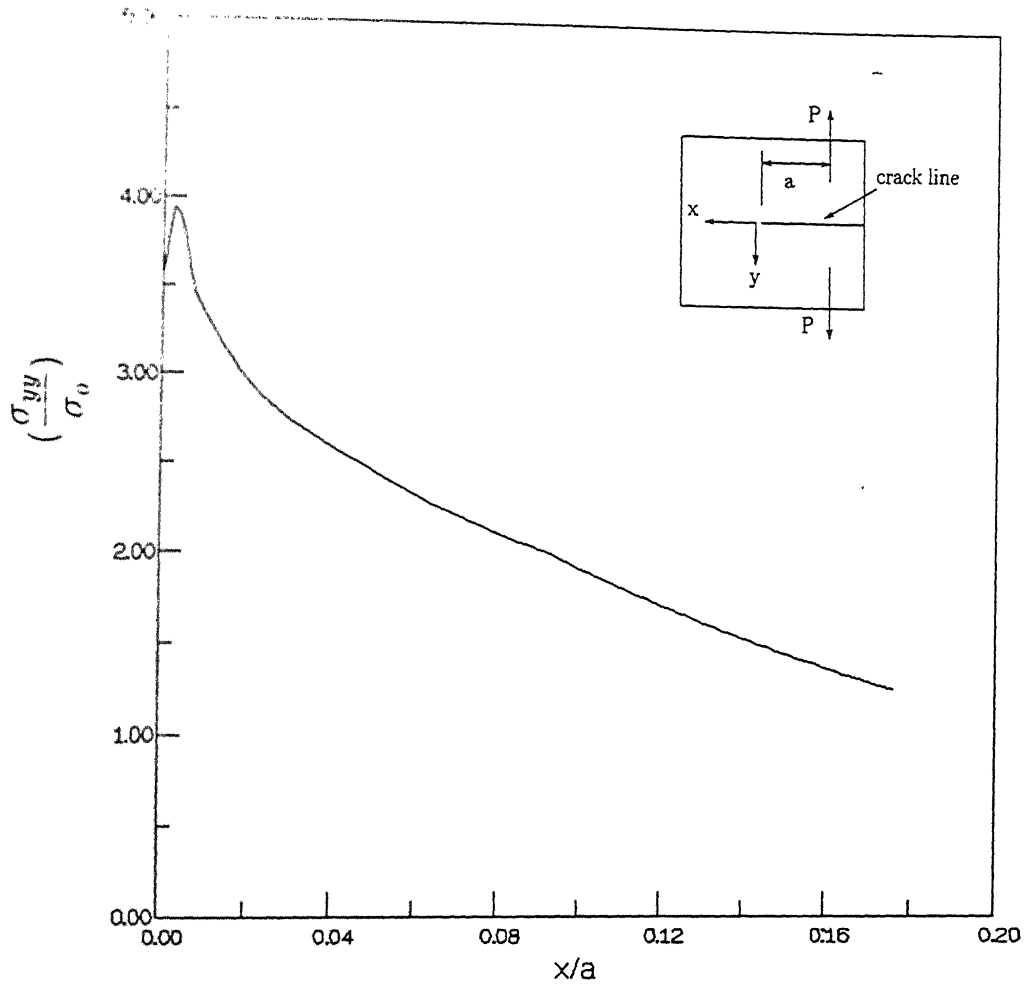

Fig.5.14 Critical damage zone.
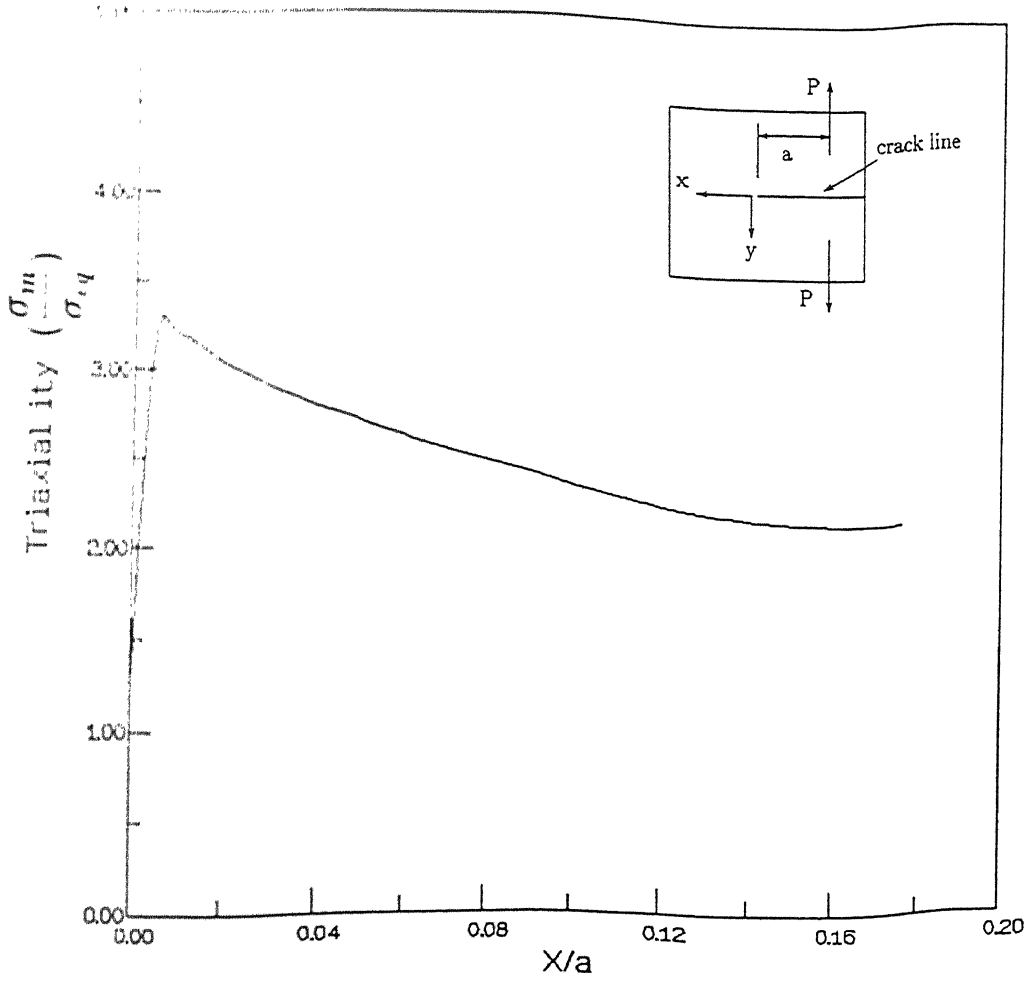
Fig 5.15.   Variation of triaxiality along the crack line.

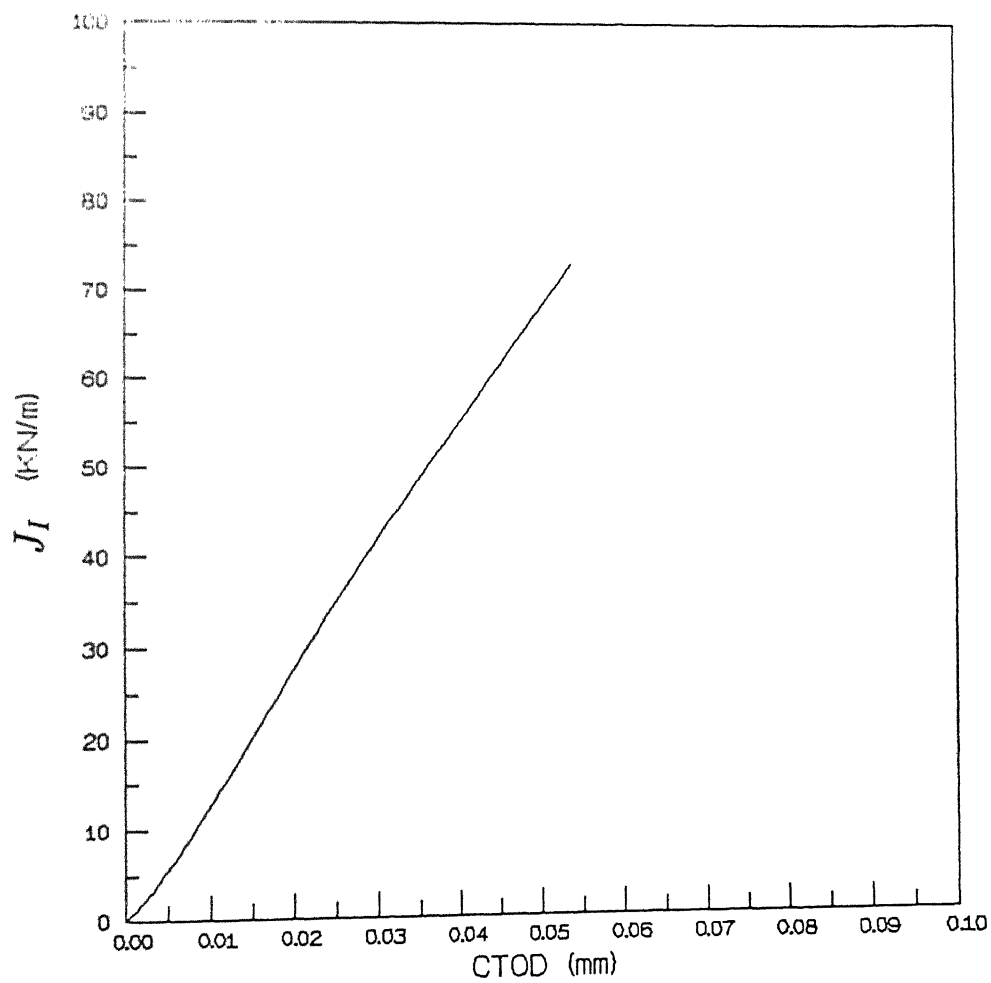Fig 5.16. Variation of σ_{yy} along the crack line.

Fig 5.17. J_I versus $CTOD$.

Chapter 6

THREE DIMENSIONAL ANALYSIS

6.1 Introduction

In chapter 5, numerical estimation of fracture parameters has been done using the plane strain analysis. However, it is observed that the specimen thickness also plays an important role in fracture process [58, 59, 60]. Truly speaking, fracture process is a three dimensional phenomenon as the deformation and stresses vary along the crack front. Even for a thick specimen, the plane strain condition prevails only in the middle part of the specimen whereas the surface regions remain in plane stress condition. Further, the crack front does not remain straight during propagation as it propagates more at the middle and less at the surface. Thus, both the crack initiation and propagation are highly dependent on the specimen thickness. In order to study the effect of specimen thickness on fracture parameters, a three dimensional analysis of the crack front deformation is necessary.

The laboratory test data of fracture parameters pertain to only the plane strain condition. However, the plane strain and plane stress conditions are only approximations to the actual state of deformation/stress when certain conditions are broadly satisfied.

115

Thus, in order to apply the laboratory test data to actual fracture mechanics problems, a knowledge of three dimensional deformation/stress field ahead of a crack front is necessary.

In the earlier Chapters, two dimensional (mainly plane strain) analysis of the ductile fracture process was carried out using the updated Lagrangian elastic-plastic formulation for a damaged material. Here the same method has been extended to three dimensional analysis of the crack front. Due to limitation of computer resources, only a crude mesh is used for the three dimensional analysis. Therefore, the results obtained are of qualitative nature only. The objective of the study is to investigate the variation of the continuum parameters along the thickness as well as the dependence of the critical fracture parameters on the thickness.

6.2   The Finite Element Analysis

1/2T CT specimens (Fig 6.1) with varying thickness (B) are analysed in FE study. The material used is AISI-1095 spherodised steel with chemical composition and mechanical properties given in Tables 5.1 and 5.2 respectively. Numerical schemes used are the same as that for the two dimensional analysis. Each specimen is divided in 3 layers across the half thickness. Each layer contains 84 twenty noded brick elements. The size of the elements along the crack front, in X-Y plane, is chosen to be of the order of the grain size of the material (see Section 5.4). Due to symmetry of the geometry and also of the loading condition, only a quarter of the specimen is analysed. Proper boundary conditions are applied at the planes of symmetry. In the Z plane, the Z displacements are restrained whereas in the Y plane, the Y displacements are restrained except at the crack face. In order to restrict the rigid body movement in X direction, a point A on the midplane which is far away from the crack front (Fig 6.1) is restrained from moving in the X direction. A $2 \times 2 \times 2$ Gauss integration scheme is used. All quantities (stress, strain, triaxiality and damage) are calculated at the Gauss points. These values are

extrapolated to the midplane while applying the crack growth initiation criterion. The total load over the thickness is calculated by summing the nodal reactions across the thickness. The load point displacement is taken as the average displacement over the thickness. Thus, the value of J_I calculated from the load deflection curve with the help of equation (5.5) is an average value over the thickness. While calculating the crack tip opening displacement, the opening of the crack faces at a distance of $0.066mm$ (one element size) behind the crack tip is considered.

6.2.1   The Crack Growth Initiation Criterion

The crack growth initiation criterion proposed in section 5.2 for two dimensional case (equation 5.1) is extended here to the three dimensional analysis. The midplane, perpendicular to the crack front, is chosen for application of the failure criterion. In this plane, D has to reach the critical value D_c at the characteristics length l_c (average austenite grain size) ahead of the crack tip for the crack to grow further. Thus, for crack growth initiation

$$D = D_c \qquad \text{at } l = l_c \quad \text{in the midplane.} \tag{6.1}$$

Therefore, the dimensions of the elements along the crack front, in X-Y plane, are selected as $2l_c \times 2l_c$. The dimension of the elements in Z direction is chosen more at the centre and less at the surface to take care of the sharp variation of the stresses close to the surface. The values of fracture toughness (J_I), triaxiality and strain at the moment when the above condition is satisfied are regarded as their critical values.

6.3   Numerical Results and Discussion

Fig (6.2) shows the comparison of load deflection curve obtained from 3-D analysis with experimental and plane strain curves of Chapter 5 (Fig 5.11). For the ease of comparison, these curves have been reproduced here. The specimen used in this study is a 1/2T CT specimen with thickness of $8mm$. There is a close matching among the results. It means

that a plane strain condition has almost been reached for a thickness of $8mm$. The thickness requirement for plane strain condition, as recommended by ASTM, is

$$B > 25\frac{J_{Ic}}{\sigma_o}, \qquad (6.2)$$

where, J_{Ic} is the plane strain fracture toughness and σ_o is the initial yield stress of the material. This gives a required value of the thickness of the specimen as $5mm$. Thus a thickness of $8mm$ is well above the required value.

Variation of Continuum Parameters along the Thickness

Variation of certain continuum parameters along the thickness at the critical condition of crack growth initiation is discussed here.

Fig (6.3) shows the variation of CTOD along the crack front. It shows larger crack-tip opening at the mid-plane and less at the surface.

Fig (6.4) gives the variation of triaxiality at the crack tip (at a distance r) along the thickness of the specimen. For the specimen of $8mm$ thickness, there is a small increase in triaxiality from the mid-plane towards the surface. The decrease in triaxiallity at the midplane is due to larger opening of the crack-tip at the mid- plane [59]. The triaxiality drops sharply near the free surface. For the specimen of $2mm$ thickness, triaxiality falls gradually from the mid-plane to the free surface showing a smooth transition from plane strain condition to the plane stress condition.

Fig (6.5) shows the variation of out of plane stress (σ_{zz}) at the crack tip (at a distance r) along the thickness. For the specimen of $2mm$ thickness, σ_{zz} is zero for a portion of the thickness near the surface indicating a complete plane stress condition near the surface. The other specimen of $8mm$ thickness has a high value of σ_{zz} at the midplane with a fairly uniform distribution over a large portion of the thickness. The value of σ_{zz} falls sharply near the surface. From Figs (6.4) and (6.5), it appears that the state of stress in the specimen of $8mm$ thickness can be approximated by a plane strain condition whereas the specimen of $2mm$ thickness requires a three dimensional

analysis.

Fig (6.6) is a graphical representation of the variation of equivalent plastic strain at the crack tip (at a distance r) along the thickness. The thiner specimen (thickness of $2mm$) requires more strain for crack growth initiation than that of thicker specimen (thickness of $8mm$). The nature of the curves matches qualitatively with that given in ref [58].

The above discussion shows that both the distribution as well as the values of the continuum parameters depend on the thickness of the specimen. Thus, a ductile fracture process is a thickness dependent phenomenon.

Critical Fracture Parameters

Fig (6.7) shows the variation of critical J_I for specimens with different thickness. It shows that critical J_I for $2mm$ thick specimen is almost 25% higher than that of the specimen of $8mm$ thickness. For a thickness of $6mm$ and above, the critical J_I becomes almost constant and close to its plane strain value J_{Ic}. It should be noted that the plane strain condition is an ideal case. A fully plane strain condition can not be achieved even for a very thick specimen. However, an approximate plane strain analysis can be carried out for those specimen whose thickness satisfies the condition of equation (6.2).

Fig (6.8) gives the variation of critical triaxiality (in the midplane) with the thickness. Thicker specimen shows larger critical triaxiality. For the specimen of thickness $6mm$ and above, the critical triaxiality saturates to its plane strain value.

Variation of critical strain (in the midplane) with the thickness is shown in Fig (6.9). A thiner specimen requires higher critical strain. A $2mm$ thick specimen requires 16% higher strain than that of $8mm$ thick specimen for crack growth initiation. Dependence of critical strain on the specimen thickness shows that a criterion based on critical strain is not enough for predicting ductile fracture. Since the effect of thickness in fracture process can be accommodated through the crack tip triaxiality, it is better to have a

critical continuum parameter depending on both strain and triaxiality to predict ductile crack growth initiation. The critical damage parameter (D_c), as identified in this thesis, fulfills the above requirement.

Enlarged view of crack tip
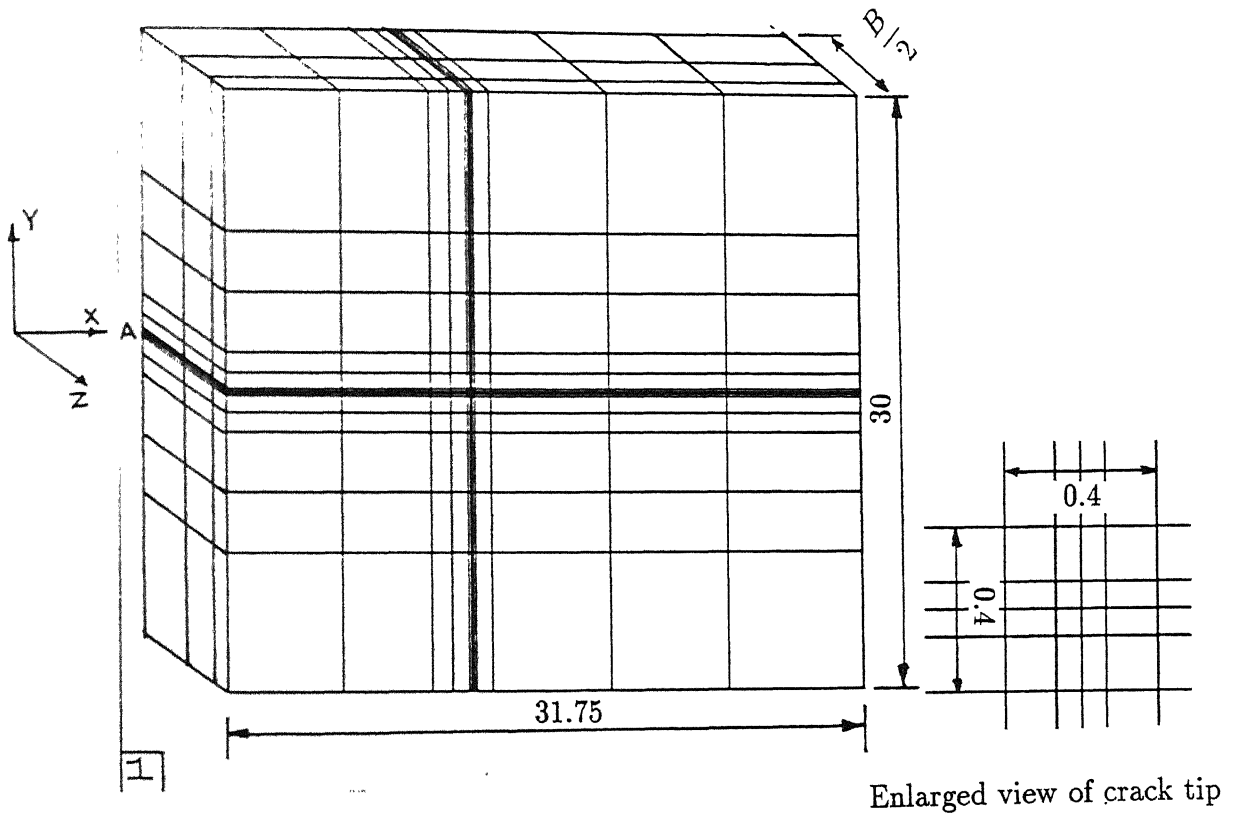
All dimensions are in mm.

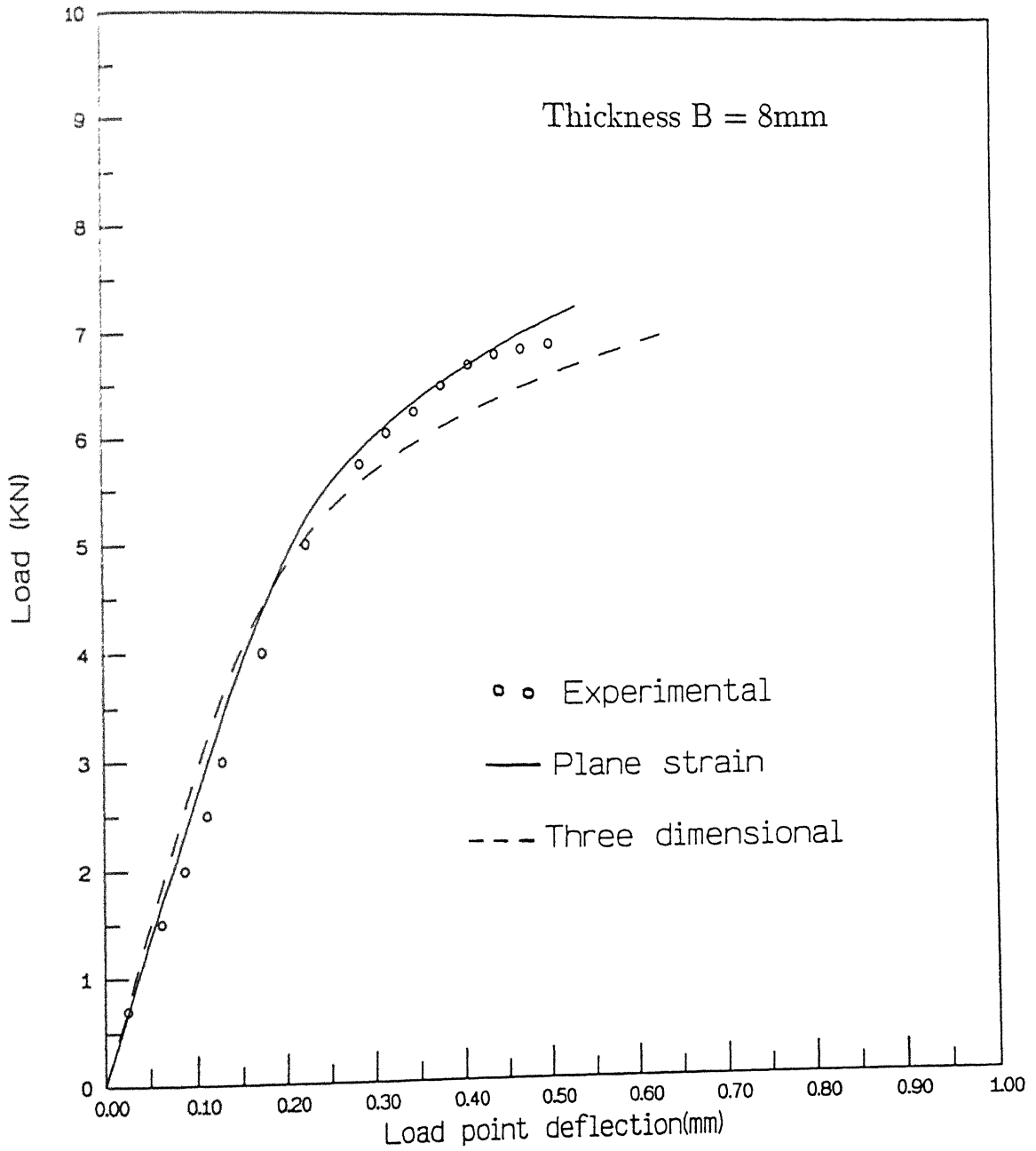Fig 6.1. 3-D finite element mesh for $\frac{1}{2}$T CT specimen.

Fig 6.2. Load deflection curve.

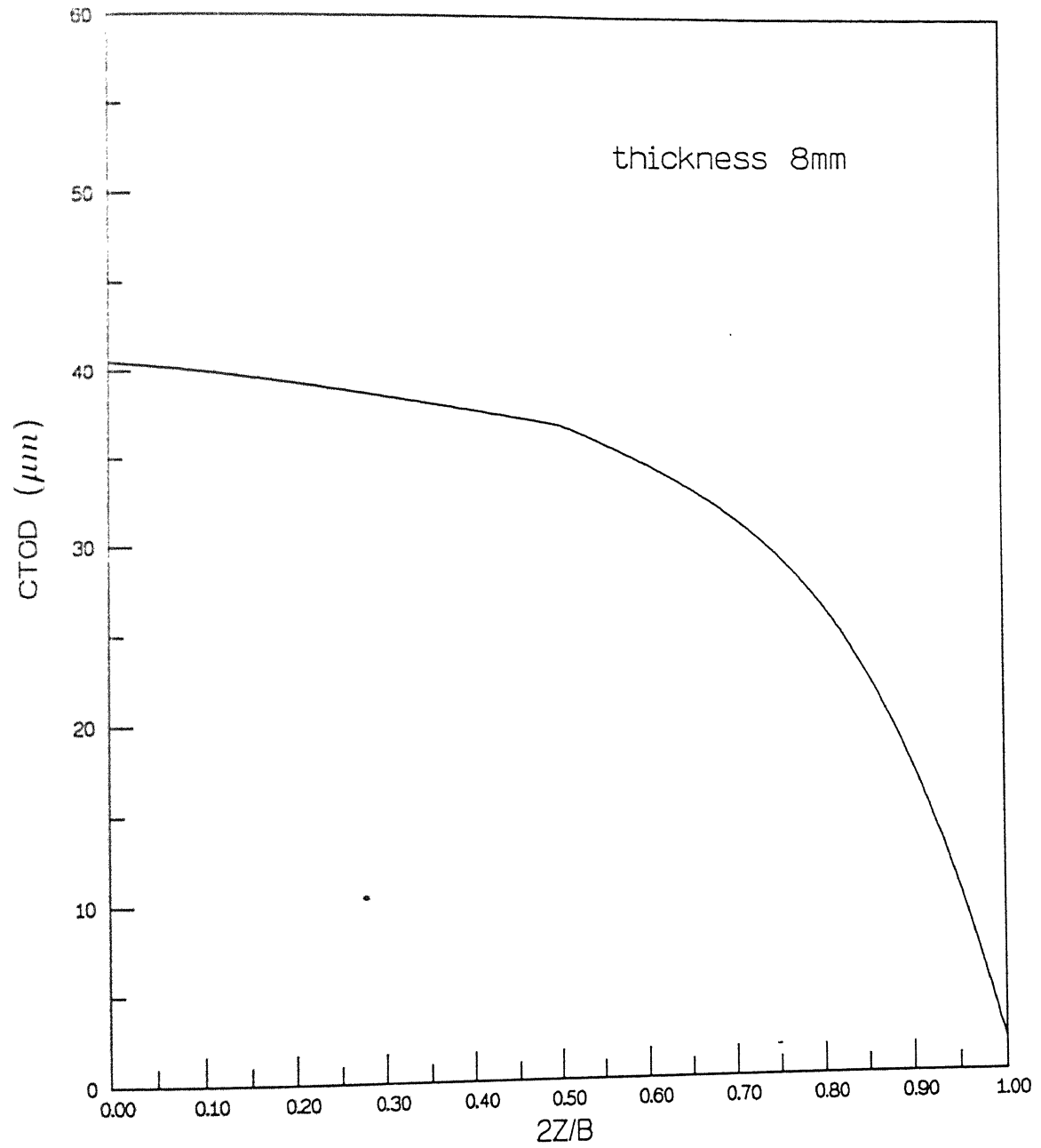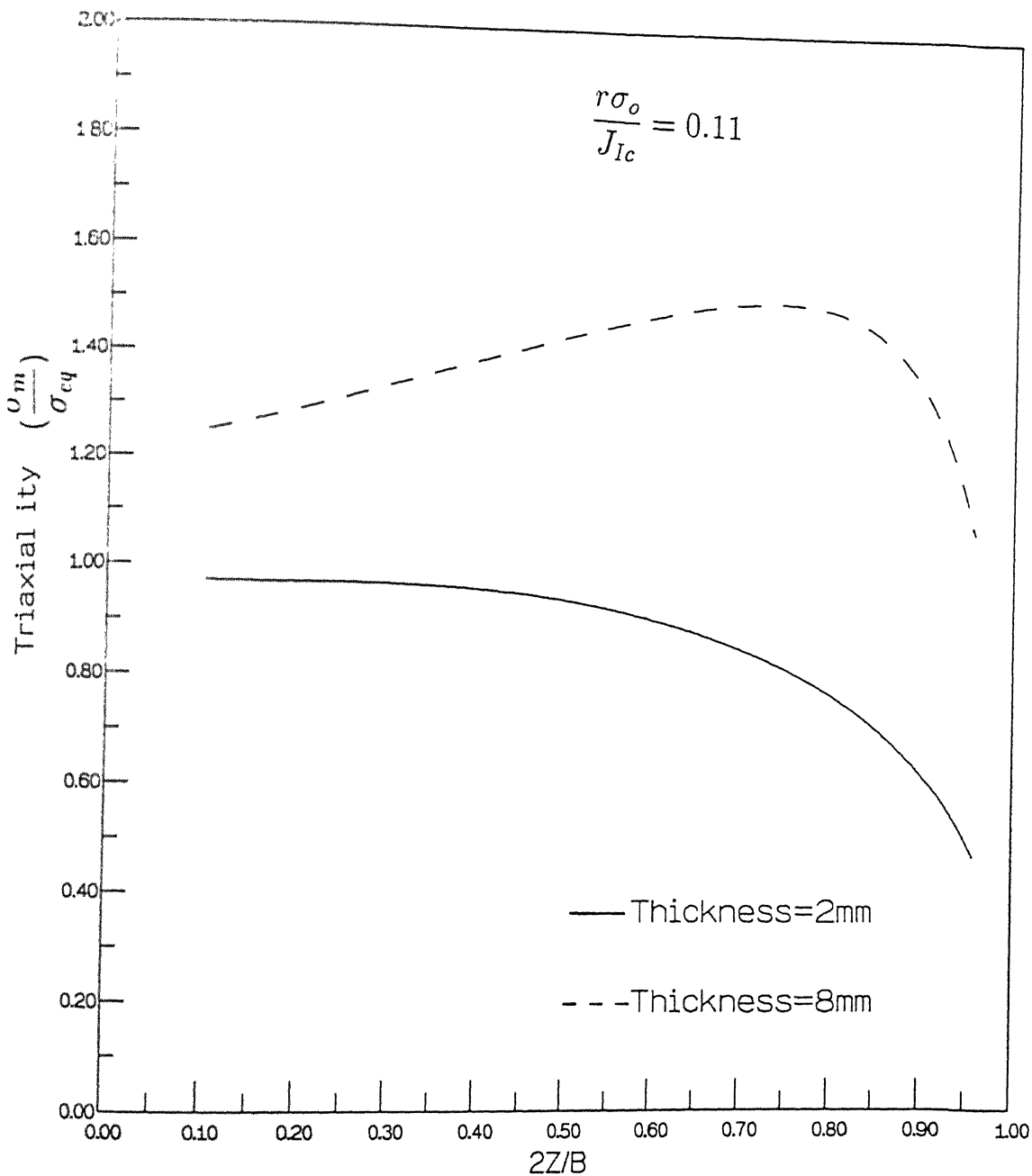Fig 6.3. Variation of CTOD along the thickness.

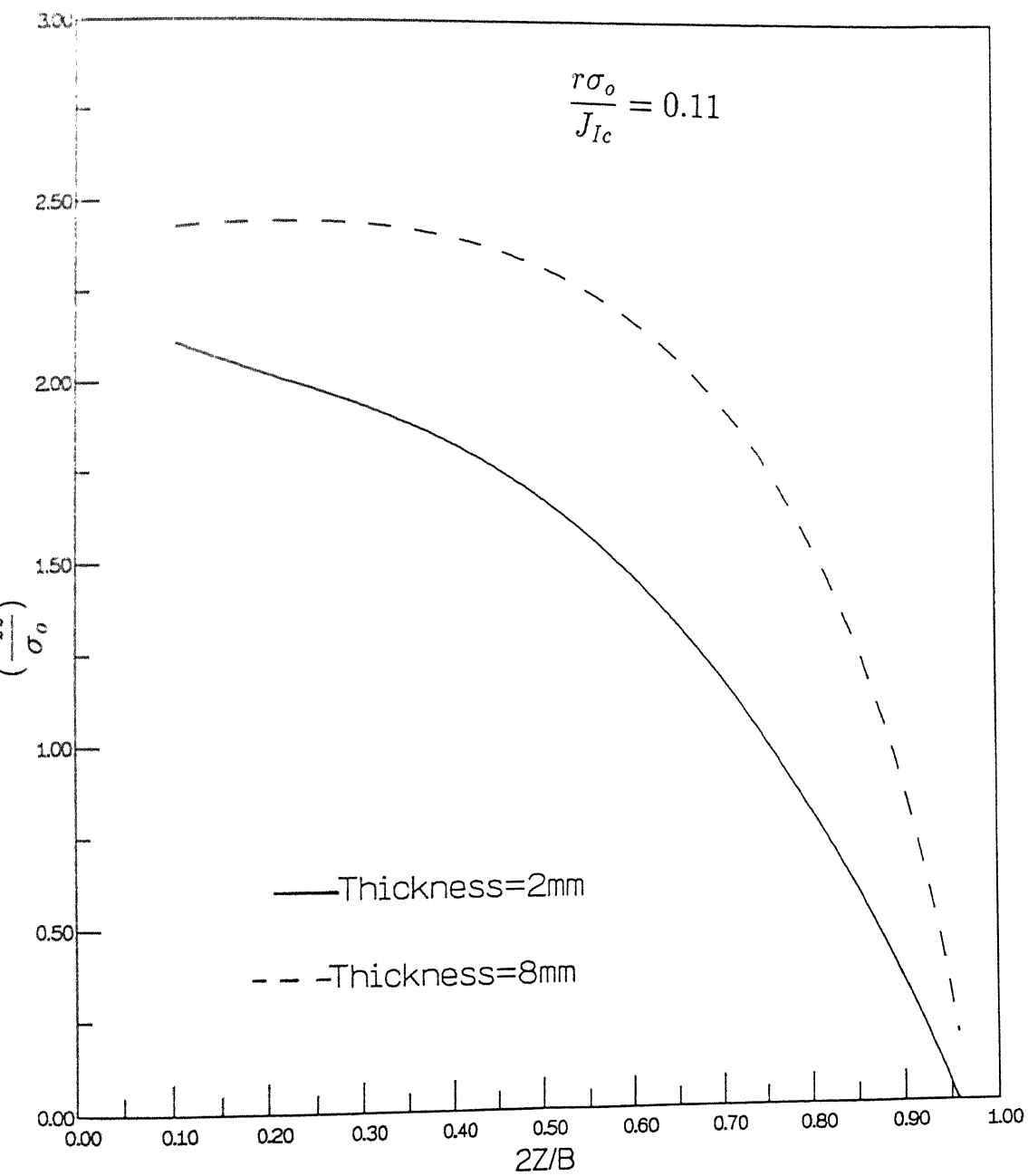Fig 6.4. Variation of triaxiality along the thickness.

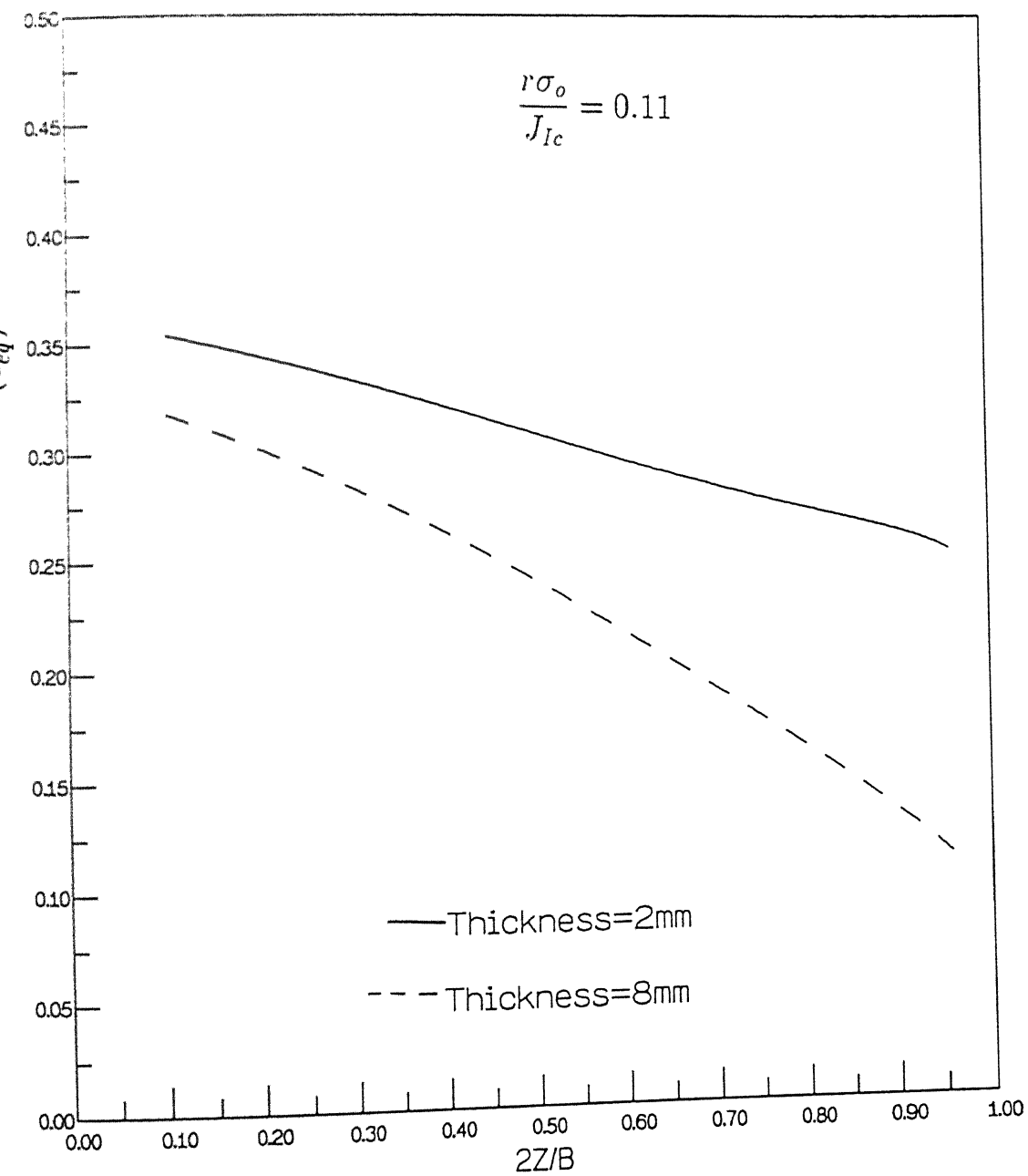Fig 6.5. Variation of out of plane stress along the thickness.

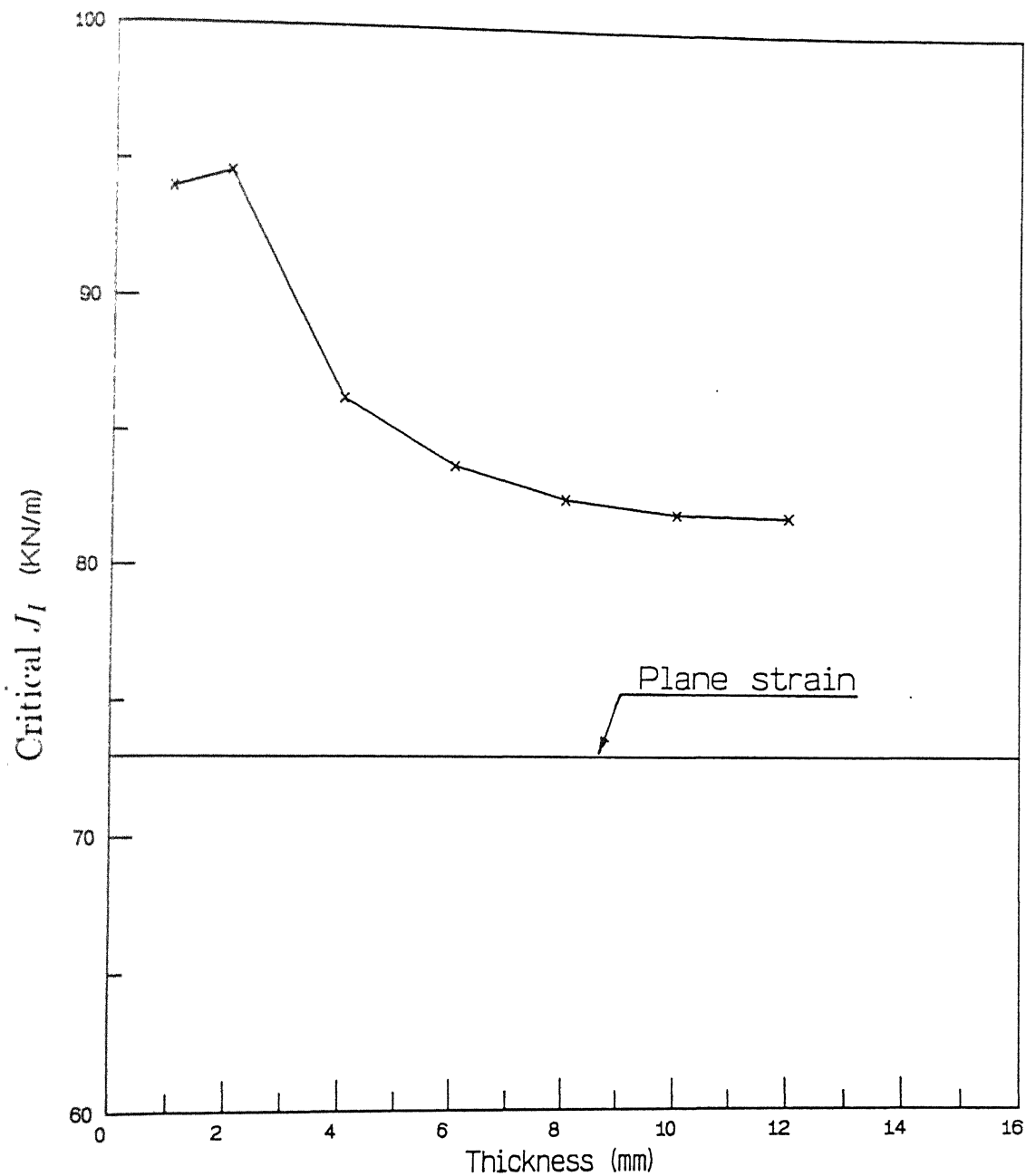Fig 6.6. Variation of plastic strain along the thickness.

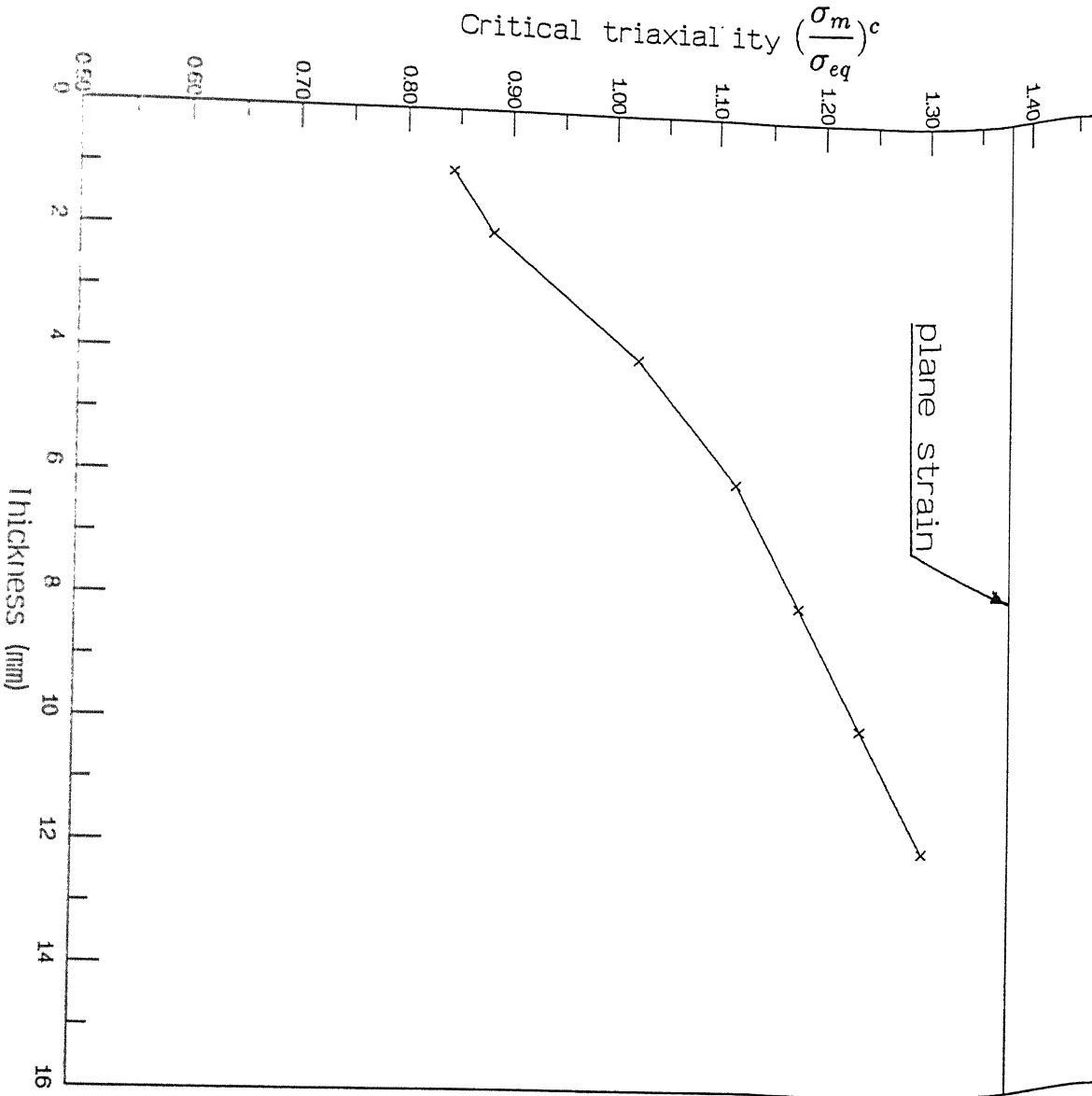Fig 6.7. Fracture toughness for specimens with
different thickness.

Fig 6.8. Critical triaxiality for specimens with different thickness.
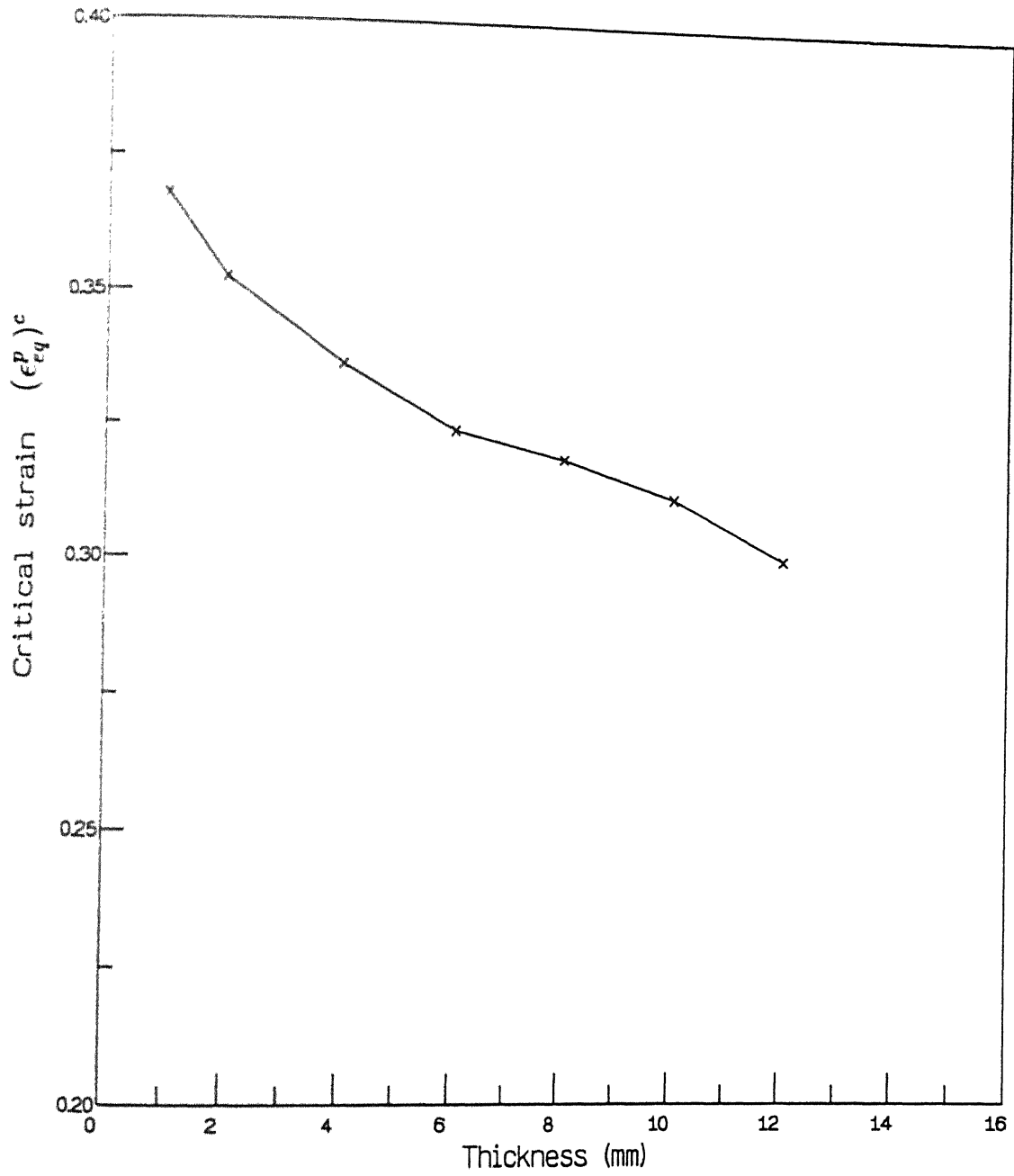
Fig 6.9. Critical strain for specimens with different thickness.

Chapter 7

SUMMARY AND CONCLUSIONS

At microscopic level, a ductile fracture process depends on void nucleation, growth and coalescence. At continuum level, it depends on the critical values of several continuum parameters. The role of triaxiallity in void growth phenomenon had been identified long back. But it has not yet been established as a proper fracture parameter either singly or in combination with other parameters. In this study an attempt has been made to explain the void growth phenomenon in Mode I ductile fracture where triaxiallity plays a major role. AISI-1090, 1095 steels are chosen as the test materials which contain a large number of secondary particles. A damage growth law has been proposed with the help of Lemaitre's continuum damage mechanics theory together with the experimental results of LeRoy et al. The damage variable D, quantifying the void growth, is physically interpreted as the area void fraction at a point in a plane. Thomason's limit load model for void coalescence is used for predicting micro crack initiation.

The results of Chapter 4 show that the ductile failure depends on both the plastic strain and the triaxiallity (Fig 4.12). Since, the damage variable D is a combination of both the plastic strain and triaxiallity, its critical value (D_c) is taken as the continuum parameter for predicting micro crack initiation. It is clear from Table 4.4 that the critical damage D_c is almost independent of the specimen geometry. Hence, D_c is taken as a material property. For AISI-1090 spherodised steel, it is coming out to be equal to 0.05.

Chapter 5 is an application of the critical damage as the continuum parameter and austenite grain size as the length parameter in a local criterion (equation 5.1) for predicting the crack growth initiation in ductile materials. The numerically predicted and the experimentally obtained values of fracture toughness (J_{Ic}) are in close agreement (see Section 5.5).

The fractographs (Figs 5.6(b), (c)) of the fractured surface reveal that the critical stretch zone width ($(SZW)_c$) lies within the range of the measured grain size ($30\mu m - 60\mu m$). The computed value of (SZW)$_c$ is $32\mu m$ which is almost equal to the average austenite grain size ($33\mu m$) of the material. The critical value of crack tip opening displacement ($(CTOD)_c$) is obtained as $56\mu m$ from the computational results (Fig 5.17). Thus, $(CTOD)_c$ is 1.8 times $(SZW)_c$ which seems reasonable. For a semicircular crack tip, this value is likely to be 2 [61].

The J verses $CTOD$ curve (Fig 5.17) gives the slope of the curve as $2.4\sigma_o$. This result falls in the range of experimental results [57] for plane strain condition.

The ratio of the plastic zone to damage zone (Figs 5.13. 5.14) is obtained as 5.6. It shows damage as a highly localised event. Sometimes a fracture process zone is defined within the plastic zone and is of the size of the critical crack tip opening displacement [4]. A critical damage zone of one austenite grain size falls within the fracture process zone.

As an overall conclusion of the results of Chapter 5, it can be stated that the proposed criterion (equation 5.1) is reasonably good in predicting crack growth initiation in ductile materials.

The results of Chapter 6 (Figs 6.3 - 6.6) give the variations of continuum parameters at the crack tip along the thickness of the specimen. It also shows the dependence of critical value of J_I and critical plastic strain $(\epsilon_{eq}^p)_c$ on the thickness of the specimen (Figs 6.7 - 6.9). The qualitative trends of the results are consistent with the earlier published results [58].

In the light of the above discussion the following conclusions can be drawn:

1. The void growth law, proposed in this study for the class of materials like AISI-1090, AISI-1095 spherodised steel, is a reasonably good approximation.

2. Thomason's limit load model is a good representation of micro crack initiation due to void growth and coalescence in ductile materials.

3. Ductile fracture process is influenced by both the plastic strain and the triaxial ity.

4. The critical damage parameter (D_c) is a good measure of ductile failure initiation due to void growth.

5. Choice of austenite grain size as the characteristic length parameter in crack growth initiation criterion leads to a good estimation of fracture parameters.

6. The elastic-plastic FE analysis together with CDM can estimate fracture parameters reasonably well.

Scope of Further Work

The CDM theory together with FE analysis has been applied here to explain Mode I ductile fracture. The proposed damage growth law and the fracture criterion can be extended to other problems of fracture mechanics and metal forming processes. some important aspects are given below:

1. Application of the proposed damage growth law and void coalescence condition in metal forming processes to predict the central burst event.

2. Application of the proposed crack growth initiation criterion to mixed mode analysis of the ductile fracture.

APPENDIX

Simulation of Necking

Necking is a phenomenon which occurs due to localization of plastic deformation in a small region. For example, in tension test of a cylindrical bar, a large reduction of diameter takes place in a small region due to local plastic flow where as the other part of the bar remains elastic. Definitely, it is an instability problem which can be treated in different ways. The common method to simulate instability is either to introduce a small perturbation in geometry or load (imperfect approach [53]) or to superpose on the displacement field of the critical load a part of the eigenmode (perfect approach). Here the imperfect approach of perturbing the geometry is used. It is done by introducing a small imperfection of the order of 0.1% in the diameter.

The phenomenon is explained below for a one dimensional problem with the help of two elements (Fig A1). The imperfection has been introduced at the bottom of element 2, i.e. at node 3. For simplicity we assume that $\Delta u^3 = 0$ and Δu^1 is the prescribed displacement at the end of the bar. One dimensional strain increments in elements (1) and (2) are

$$\Delta \epsilon^1 = \frac{\Delta u^1 - \Delta u^2}{l_1} \tag{A1}$$

and

$$\Delta \epsilon^2 = \frac{\Delta u^2 - \Delta u^3}{l_2} = \frac{\Delta u^2}{l_2} \qquad \text{since } \Delta u^3 \text{ is zero.} \tag{A2}$$

Here l_1 and l_2 are the lengths of the elements as shown in Fig A1(a). Since the element (2) has a lesser cross section than that of element (1), the stress level in element (2) is higher than that of element (1) to maintain equilibrium. These stress levels are indicated by points 1 and 2 on one dimensional stress-strain curve in Fig A1(b). Since the slope of the stress strain curve at point 2 is less than that at point 1, element (2) requires a greater strain increment than that of element (1) to have the same stress increment. More over, element (2) requires a larger stress increment to equilibrate the load since its cross section is less. Thus, for equilibrium it is required that

$$\Delta \epsilon^2 > \Delta \epsilon^1. \tag{A3}$$

Since Δu^1 is a fixed prescribed displacement increment, a situation will arise when

$$\Delta u^2 > \Delta u^1. \tag{A4}$$

Then equation (A1) shows that element(1) experiences negative strain increment or unloading where as the positive strain increment in element (2) increases.
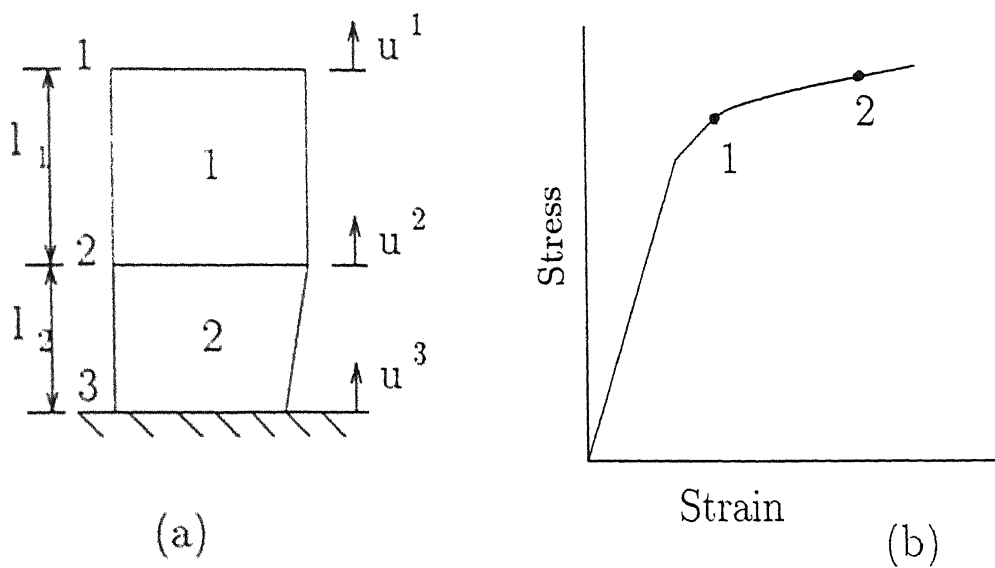
Fig A1: Simulation of necking

REFERENCES

[1] J. W. Hutchinson. (1968), 'Singular behaviour at the end of a tensile crack in a hardening material', *J. Mech. Phy. Solids*, 16, pp 13-31.

[2] J. R. Rice and G. F. Rosengren. (1968), 'Plane strain deformation near a crack tip in a power law hardening material, *J. Mech. Phy. Solids*, 16, pp 1-12.

[3] J. R. Rice, (1968), 'A path independent integral and the approximate analysis of strain concentration by notches and cracks', *J. App. Mech*, 35, pp 379-386.

[4] M. F. Kanninen and C. H. Popelar, (1985) *Advanced fracture mechanics*. Oxford University Press, NewYork.

[5] F. A. McClintock, (1967), 'On the mechanics of fracture from inclusion'. *Ductility*, ASM, Metal park, Ohio, pp 255-275.

[6] P. Perzyna, (1985), 'On constitutive modelling of dissipative solids for plastic flow, instability and fracture', *Plasticity Today*, A. Sawczuk and G. Bianchi edited, pp 657-679.

[7] J. Lemaitre, (1985), 'A continuous damage mechanics model for ductile fracture', *J. Eng. Mat. Tech*, 107, pp 83-89.

[8] G. Rousselier, (1987), 'Ductile fracture model and their potential in local approach of fracture', *Nucl. Eng. Desn*, 105, pp 97-111.

[9] P. F. Thomason, (1990), 'Three dimensional models for the plastic limit load at incipient failure of intervoid matrix in ductile porous solids', *Acta Metall*, 33, pp 1079-1085.

[10] M. L. Williams, (1957) 'On stress distribution at the base of a crack', *J. App. Mech*, 24, pp 109-114.

[11] G. R. Irwin, (1957), 'Analysis of stress and strain near the end of a crack traversing a plate', *J. App. Mech*, 24, pp 361-364.

[12] G. R. Irwin, (1968), 'Linear fracture mechanics, fracture transition, fracture control', *Eng. Fract. Mech*, 1, pp 241-257.

[13] J. W. Hutchinson and P. C. Paris, (1979), ' Stability analysis of *J* controlled crack growth', *Elastic- Plastic Fracture*, ASTM STP-668, Philadelphia. Pa, pp 37-64.

[14] J. F. Knott, (1973), *Fundamentals of Fracture Mechanics*. Butterworths, U.K.

[15] C. F. Shih, (1981), 'Relationship between the *J* integral and the crack tip opening displacement for stationary and extending cracks', *J. Mech. Phy. Solids*, 29, pp 305-326.

[16] R. M. McMeeking and D. M. Parks, (1979), 'On criteria of *J* dominance of crack tip fields in large scale yielding, *Elastic Plastic Fracture*, ASTM STP 668 , Philadelphia. Pa, pp 175-194.

[17] C. F. Shih and M. D. German, (1981), 'Requirements for a one parameter characterization of crack tip fields by HRR singularity', *Int. J. Fract*, 17, pp 27-43.

[18] J. R. Rice and M. A. Johnson, (1970), 'The role of large crack tip geometry changes in plane strain fracture', *Inelastic Behavior of Solids*, Kanninen, Adler, Rosenfield and Jaffe edited, pp 641-672.

[19] A. C. Mackenzie, J. W. Hancock and D. K. Brown, (1977), 'On the influence of state of stress on ductile failure initiation in high strength steels', *Eng. Fract. Mech*, 9, pp 167-188.

[20] D. K. Brown, J. W. Hancock, R. Thomson and D. M. Parks, (1980), The effect of dilating plasticity on some elastic plastic stress and strain concentration problems relevant to fracture', *Numer. Methd. in Fract. Mech*, D. R. Owen and A. R. Luxmoore edited, pp 309-325.

[21] C. A. Berg, (1970), 'Plastic dilation and void interaction', *Inelastic Behavior of Solids*, Kanninen, Adler, Rosenfield and Jaffe edited, pp 171-210.

[22] A. L. Gurson, (1977), 'Continuum theory of ductile rapture by void nucleation and growth: Part I - Yield criteria and flow rules for porous ductile media', *J. Eng. Mat. Tech*, 99, pp 2-15.

[23] V. Tvergaard, (1981), 'Influence of voids on shear band instabilitys under plane strain condition', *Int. J. fract*, 17, pp 389-406.

[24] J. W. Rudnicki and J. R. Rice, (1975), 'Conditions for the localization of deformation in pressure sensitive dilatant materials', *J. Mech. Phy. Solids*, 23, pp 371-394.

[25] H. Yamamoto, (1978), 'Conditions for shear localization in the ductile fracture of void containing materials', *Int. J. Fract*, 14, pp 347-365.

[26] P. F. Thomason, (1990), *Ductile fracture*, Pergamon Press, (U.K).

[27] N. Alberti, A. Barcellona, L. cannizzaro and F. Micari, (1994), 'Prediction of ductile fracture in metal forming processes: an approach based on the damage mechanics', *Annals. CIRP*, 43, pp 207-210.

[28] S. H. Goods and L. M. Brown, (1979), 'The nucleation of cavities by plastic deformation', *Acta Metall*, 27 pp 1-15.

[29] J. R. Rice and D. M. Tracy, (1969), 'On the Ductile enlargement of voids in triaxial stress field, *J. Mech. Phy. Solids*, 17, pp 201-217.

[30] A. S. Argon and J. Im, (1975), 'Separation of second phase particles in spherodised 1045 steel, Cu 0.6 Pct Cr alloy and Maraging steel in plastic straining', *Metall. Trans*, 6A, pp 839-851.

[31] J. Gurland, (1972), 'Observation on the fracture of cementite particles in spherodised 1.05 % C steel deformed at room temperature', *Acta Metall*, 20, pp 735-741.

[32] F. A. McClintock, (1968), 'A criterion for ductile fracture by the growth of holes', *J. App. Mech*, June, pp 363-371.

[33] S. E. Clift, P. Hartley, C. E. N. Sturgess and G. W. Rowe, (1990), 'Fracture prediction in plastic deformation processes', *J. Mech. Sci*, 32, pp 1-17.

[34] S. I. Oh, C. C. Chen and S. Kobayashi, (1979), 'Ductile fracture in axisymmetric extrusion and drawing', *J. Engn. Indus*, 101, pp 36-44.

[35] W. H. Tai and B. X. Yang, (1986), 'A new microvoid damage model for ductile fracture', *Eng. Frac. Mech*, 25 pp 377-384.

[36] G. LeRoy, J. D. Embury, G. Edward and M. F. Ashby, (1981), 'A model of ductile fracture based on nucleation and growth of voids', *Acta Metall*, 29, pp 1509-1522.

[37] W. T. Jun, (1992), 'Unified CDM model and local criteria for ductile fracture-I', *Engn Fract Mech*, 42, pp 177-183.

[38] B. A. Bilby, I. C. Howard and Z. H. Li, (1992), 'Prediction of the first spinning cylinder test using ductile damage theory', *Fat. fract. Engn. Mat. Struct*, 16, pp 1-20.

[39] M. Zheng, Z. J. Luo and X. Zheng, (1992), 'A new damage model for ductile material', *Engn. Fract. Mech*, 41, pp 103-110.

[40] M. G. Cockcroft and D. J. Latham, (1968), 'Ductility and workability of metals', *J. Inst. Metals*, 96, pp 33-39.

[41] M. Oyane, (1972), 'Criteria of ductile strain', *Bull. J. S. M. E*, 15, pp 1507-1513.

[42] R. O. Ritchie, J. F. Knott and J. R. Rice, (1973), 'On the relationship between critical tensile stress and fracture toughness in mild steel', *J. Mech. Phy. Solids*, 21 pp 395-410.

[43] R. O. Ritchie, W. L. Server, R. A. Wullaert, (1979), 'Critical fracture stress and fracture strain models for the prediction of lower and upper self toughness in nuclear pressure vessel steels'. *Metall Trans*, 10A, pp 1557-1570.

[44] P. Germain, Q. S. Nguyen and P. Suquet, (1983), 'Continuum thermodynamics', *J. App. Mech*, 50, pp 1010-1020.

[45] H. Ziegler, (1983), *An introduction to thermomechanics*, North Holland publishing company, Amsterdam.

[46] R. M. McMeeking, (1991), 'Crack blunting and void growth models for ductile fracture', *Topics in Fracture Fatigue*, A. S. Argon edited, pp 179-196.

[47] K. J. Bathe, E. Ramm and E. L. Wilson, (1975), 'Finite element formulations for large deformation dynamic analysis', *Int. J. Num. Meth. Engn*, 9, pp 353-386.

[48] M. A. Crisfield, (1987), 'Consistent schemes for plasticity computation with Newton-Raphson method', *Computational Plasticity Part-I*, D. R. Owen, E. Hinton, E. Oñate edited, pp 133-159.

[49] E. Ramm, (1980), 'Strategies for tracing nonlinear response near limit points', *Europe-U.S workshop on nonlinear finite element analysis in structural mechanics*, July 28-31, Bochum.

[50] J. L. Batoz and G. Dhatt, (1979), 'Incremental displacement algorithms for nonlinear problems', *Int. J. Num. Meth. Engn*, 14, pp 1262-1268.

[51] T. R. Tsu, (1986), *The finite element method in thermomechanics*, Allen and Unwin, London.

[52] P. W. Bridgman (1952), *Studies in large plastic flow and fracture*, McGraw Hill, New York.

[53] W. H. Chen, (1971), 'Necking of a bar', *J. Mech. Phy. solids*, 7, pp 685-717.

[54] J. W. Hancock and D. K. Brown, (1983), 'On the role of strain and stress in ductile fracture', *J. Mech. Phy. Solids*, 31, pp 1-24.

[55] I. C. Howard, (1992), *Elastic plastic fracture mechanics*, Workshop at Jadavpur Univ. Calcutta, Jan 4-8.

[56] ASTM STP 743, *Fracture Mechanics*, Richard Roberts edited.

[57] S. A. Paranjape and S. Banerjee, (1979) 'Interrelation of crack tip opening displacement and *J* integral', *Engn. Fract. Mech.* 11, pp 43-50.

[58] W. Brocks, G. Kunecke, H. D. Noack and H. Veith, (1989), 'On the transferability of fracture mechanics parameters from specimens to structures using FEM', *Nucl. Engn. Desn*, 112, pp 1-14.

[59] J. Faleskog, (1994), 'An experimental and numerical investigation of ductile crack growth characteristics in surface cracked specimens under combined loading', *Int. J. Fract*, 68, pp 99-126.

[60] C. L. Chow and X. F. Chen, (1995), 'Three dimensional fracture analysis of CT specimens with ductile damage model based on endochronic plasticity', *Int. J. Fract*, 69, pp 229-249.

[61] D. Broek, (1989), '*The Practical Use of Fracture Mechanics*', Kluwer Academic Publishers, Netherlands.